

# Flamelet-generated manifolds : development and application to premixed laminar flames

**Citation for published version (APA):**

Oijen, van, J. A. (2002). *Flamelet-generated manifolds : development and application to premixed laminar flames*. [Phd Thesis 1 (Research TU/e / Graduation TU/e), Mechanical Engineering]. Technische Universiteit Eindhoven. <https://doi.org/10.6100/IR557848>

**DOI:**

[10.6100/IR557848](https://doi.org/10.6100/IR557848)

**Document status and date:**

Published: 01/01/2002

**Document Version:**

Publisher's PDF, also known as Version of Record (includes final page, issue and volume numbers)

**Please check the document version of this publication:**

- A submitted manuscript is the version of the article upon submission and before peer-review. There can be important differences between the submitted version and the official published version of record. People interested in the research are advised to contact the author for the final version of the publication, or visit the DOI to the publisher's website.
- The final author version and the galley proof are versions of the publication after peer review.
- The final published version features the final layout of the paper including the volume, issue and page numbers.

[Link to publication](#)

**General rights**

Copyright and moral rights for the publications made accessible in the public portal are retained by the authors and/or other copyright owners and it is a condition of accessing publications that users recognise and abide by the legal requirements associated with these rights.

- Users may download and print one copy of any publication from the public portal for the purpose of private study or research.
- You may not further distribute the material or use it for any profit-making activity or commercial gain
- You may freely distribute the URL identifying the publication in the public portal.

If the publication is distributed under the terms of Article 25fa of the Dutch Copyright Act, indicated by the "Taverne" license above, please follow below link for the End User Agreement:

[www.tue.nl/taverne](http://www.tue.nl/taverne)

**Take down policy**

If you believe that this document breaches copyright please contact us at:

[openaccess@tue.nl](mailto:openaccess@tue.nl)

providing details and we will investigate your claim.

# Flamelet-Generated Manifolds: Development and Application to Premixed Laminar Flames

PROEFSCHRIFT

ter verkrijging van de graad van doctor aan de Technische Universiteit Eindhoven, op gezag van de Rector Magnificus, prof.dr. R.A. van Santen, voor een commissie aangewezen door het College voor Promoties in het openbaar te verdedigen op woensdag 18 september 2002 om 16.00 uur

door

Jeroen Adrianus van Oijen

geboren te Vlijmen

Dit proefschrift is goedgekeurd door de promotoren:

prof.dr. L.P.H. de Goey  
en  
prof.dr.ir. A.A. van Steenhoven

Copyright © 2002 by J.A. van Oijen

All rights reserved. No part of this publication may be reproduced, stored in a retrieval system, or transmitted, in any form, or by any means, electronic, mechanical, photocopying, recording, or otherwise, without the prior permission of the author.

Printed by the Eindhoven University Press.

CIP-DATA LIBRARY TECHNISCHE UNIVERSITEIT EINDHOVEN

Oijen, Jeroen A. van

Flamelet-generated manifolds : development and application to premixed laminar flames / by Jeroen A. van Oijen. – Eindhoven : Technische Universiteit Eindhoven, 2002.

Proefschrift. – ISBN 90-386-3053-0

NUR 978

Subject headings: premixed laminar flames / reduced chemical models / flamelets / flamelet-generated manifolds / flame stretch / triple flames

*To my parents*



# Contents

<b>1</b>	<b>Introduction</b>	<b>1</b>
1.1	Background . . . . .	1
1.2	Chemically reacting flows . . . . .	3
1.3	Combustion chemistry . . . . .	7
1.4	Reduced chemical models . . . . .	10
1.5	Purpose of this study . . . . .	14
1.6	Outline . . . . .	15
<b>2</b>	<b>Flamelet-Generated Manifolds</b>	<b>17</b>
2.1	Flamelet equations . . . . .	17
2.2	Manifold construction . . . . .	21
2.2.1	One-dimensional manifold . . . . .	21
2.2.2	Multi-dimensional manifolds . . . . .	23
2.2.3	Conserved variables . . . . .	24
2.3	Application of FGM . . . . .	25
2.3.1	Storage and retrieval . . . . .	25
2.3.2	Reduced set of equations . . . . .	29
2.4	Test results . . . . .	31
2.4.1	One-dimensional validation . . . . .	31
2.4.2	Two-dimensional validation . . . . .	32
2.4.3	Computational efficiency . . . . .	35
2.5	Conclusions . . . . .	38
<b>3</b>	<b>Flame Stretch</b>	<b>41</b>
3.1	Introduction . . . . .	41
3.2	Mass burning rate of premixed flames . . . . .	41
3.2.1	Mass burning rate of stretchless flames . . . . .	42
3.2.2	Mass burning rate of stretched flames . . . . .	43
3.3	Premixed counterflow flames . . . . .	44
3.4	Numerical simulations . . . . .	47
3.4.1	Results for $Le_i = 1$ . . . . .	48
3.4.2	Results for $Le_i = 1.1$ . . . . .	53
3.4.3	Results for $Le_i = const$ . . . . .	55
3.5	Conclusions . . . . .	57

---

<b>4</b>	<b>Partially Premixed Flames</b>	<b>59</b>
4.1	Introduction . . . . .	59
4.2	Numerical simulations . . . . .	62
4.3	Results . . . . .	65
4.3.1	Comparison detailed chemistry/FGM . . . . .	66
4.3.2	Flame propagation and mixing length . . . . .	70
4.3.3	Flamelet analysis . . . . .	71
4.4	Conclusions . . . . .	78
<b>5</b>	<b>Application to a Semi-Practical Combustion System</b>	<b>81</b>
5.1	Introduction . . . . .	81
5.2	Experimental set-up . . . . .	81
5.3	Numerical simulation . . . . .	83
5.3.1	Porous burner . . . . .	83
5.3.2	Radiation . . . . .	84
5.3.3	Computational domain and boundary conditions . . . . .	85
5.4	Results . . . . .	86
5.5	Conclusions . . . . .	90
<b>6</b>	<b>Summarizing Conclusions</b>	<b>91</b>
	<b>Nomenclature</b>	<b>95</b>
<b>A</b>	<b>Reaction Mechanism</b>	<b>99</b>
<b>B</b>	<b>An Alternative Way to Create Multi-Dimensional Manifolds</b>	<b>101</b>
	<b>References</b>	<b>105</b>
	<b>Abstract</b>	<b>113</b>
	<b>Samenvatting</b>	<b>115</b>
	<b>Curriculum Vitae</b>	<b>117</b>
	<b>Dankwoord</b>	<b>119</b>

# Introduction

## 1.1 Background

This thesis concerns a new efficient method to model the chemistry in combustion simulations. Combustion is the main source of energy for, e.g., transportation, heating and electrical energy production. More than 80% of our worldwide energy support is provided by combustion of organic fuels. This makes it really worthwhile studying combustion processes. The key words in combustion research are clean and efficient. Efficient, because our resources of fossil fuels are limited, so we have to use them wisely. Despite the growth of renewable energy sources, like solar and wind energy, fossil fuels will continue to be an important energy source for the next 100 years [97].

Clean combustion has become an important aspect in the last decades. Besides heat, combustion of hydrocarbon fuels always generates unwanted products or pollutants. Some examples of pollutant species are carbon monoxide (CO), which is highly toxic, and sulphur and nitrogen oxides (SO<sub>x</sub> and NO<sub>x</sub>), which cause acid rain. The emission of carbon dioxide (CO<sub>2</sub>), which is inherent to combustion of fossil fuels, is believed to be responsible for the greenhouse effect and can only be reduced by improving the efficiency of combustion appliances. Due to an increased awareness of the ecological impact of these emissions, ever more restrictive emission regulations have been passed by the government, forcing the industry to acquire detailed, fundamental knowledge of the combustion process.

In the 17<sup>th</sup> century it was believed that fire was a matter called phlogiston, which escaped from a burning object. Some 100 years later Lavoisier (1743–1794) disproved the phlogiston theory and he showed that combustion is nothing else than a chemical reaction between fuel and oxygen. Modern combustion research started in the beginning of the 20<sup>th</sup> century with scientists like Arrhenius and Zeldovich. Until 1960 combustion research was mainly of empirical nature and analytical work considered extremely simplified models only. With the advent of fast computers and the growing knowledge of chemical kinetics during the last decades, a detailed mathematical description of chemically reacting flows became available. Like in many other fields of fluid dynamics, computational fluid dynamics (CFD) has become an important part of combustion research.

Although the speed and storage capacity of modern computers increases continuously, it is still impossible to employ models that use detailed chemistry for the simulation of combustion in practical furnaces. Especially the models for turbulent flames are tremendously complicated due to the large range of time and length scales involved. The modelling of laminar flames is easier because the flow is relatively simple. Nowadays, numerical simulations of one-dimensional laminar flames with detailed chemistry and transport models are often used in combustion research. Nevertheless, the computation time for multi-dimensional laminar flame models prohibits the simulation of flames in complex

geometries or an investigation of the influence of different parameters.

The use of complex reaction mechanisms is, apart from some simple cases, impossible, because for each species a partial differential equation has to be solved, and a typical reaction mechanism for hydrocarbon combustion considers more than 100 species [92]. Furthermore, the chemical kinetics cause the system of differential equations to be very stiff, which makes the use of expensive implicit solvers inevitable. Therefore, much research is spent on the development of reduction methods, which create reduced chemical models based on the complex reaction mechanism. These simplified chemistry models reduce the computational effort considerably without losing too much accuracy.

The first and probably the most well-known systematic reduction method is introduced by Peters *et al.* [65, 66]. This method (referred to as conventional reduction technique) is based on the observation that due to very fast chemical processes in combustion problems many chemical species and reactions are in quasi-steady state or partial equilibrium. When a species is assumed to be in steady state, the corresponding differential equation can be replaced by an algebraic relation, which reduces the computational cost. The main disadvantage of the method is that a vast knowledge of the chemical kinetics is required, because the researcher has to decide which species can be assumed to be in steady state. This problem is solved in the reduction methods introduced by Lam and Goussis [46] and Maas and Pope [54]. In these reduction techniques a more mathematical approach is used, which makes it possible to perform the reduction procedure automatically without insight of the user in the chemical kinetics. In both methods the fast chemical processes are identified by a mathematical analysis of the chemical system. Linear combinations of species corresponding to the fast chemical processes are assumed to be in steady state. In the method of Maas and Pope the fast and slow chemical processes are separated by using an eigenvalue analysis of the Jacobian of the chemical source term, while Lam and Goussis propose a computational singular perturbation method.

The methods based on steady-state assumptions are, however, less efficient in 'low'-temperature regions. At high temperatures many chemical processes are fast and can be assumed to be in partial equilibrium. At lower temperatures the number of slow chemical processes increases and less species can be assumed to be in quasi-steady state. At these lower temperatures, convection and diffusion become important and the local mixture composition is determined by a balance between convection, diffusion and reaction.

In this thesis a new reduction method is presented, that is not only based on 'chemical' assumptions like existing reduction methods, but that also takes the main parts of convection and diffusion into account. This reduction method is developed for premixed laminar flames. In premixed flows, fuel and oxidizer are mixed on a molecular level. Since the chemical reactions taking place are typically very fast, premixed flames are characterized by a thin propagating flame front with a thickness in the order of a tenth of a millimeter in the case of atmospheric hydrocarbon flames. The propagation of the flame front normal to itself, the so-called burning velocity, is the key feature of premixed combustion. In this thesis the method is applied to premixed methane/air flames, because methane ( $\text{CH}_4$ ) is the main component of natural gas. However, the method can be applied to any fuel and any reaction mechanism without detailed knowledge of the chemical kinetics.

In the remainder of this chapter the equations governing chemically reacting flows are presented. The mathematical description of the chemistry is presented in section 1.3. The most important reduction methods are discussed in section 1.4. At the end of this chapter an outline of the remaining part of this thesis is given.

## 1.2 Chemically reacting flows

In this section we formulate the equations describing chemically reacting flows. The evolution of chemically reacting flows is governed by a set of transport equations describing the conservation of mass, momentum, energy and chemical components. We formulate these conservation laws as well as the constitutive relations. Models are presented for the diffusion velocity of species, for the stress tensor, and for the heat-flux vector. A model for the chemistry is presented in the next section. More detailed information on the derivation of the conservation equations for a reacting gas mixture can be found in [95].

Conservation of mass is expressed by the continuity equation

$$\frac{\partial \rho}{\partial t} + \nabla \cdot (\rho \mathbf{u}) = 0, \quad (1.1)$$

where  $\rho$  is the mass density and  $\mathbf{u} = (u, v, w)^T$  the velocity of the gas mixture. Conservation of momentum is covered by the Navier-Stokes equations

$$\frac{\partial(\rho \mathbf{u})}{\partial t} + \nabla \cdot (\rho \mathbf{u} \mathbf{u}) = -\nabla p - \nabla \cdot \boldsymbol{\tau} + \rho \mathbf{g}, \quad (1.2)$$

with  $p$  the hydrostatic pressure,  $\boldsymbol{\tau}$  the stress tensor, and  $\mathbf{g}$  the acceleration due to gravity. No body forces other than gravity are considered in (1.2). For matters of convenience, the equation describing conservation of energy is written in terms of the specific enthalpy  $h$

$$\frac{\partial(\rho h)}{\partial t} + \nabla \cdot (\rho \mathbf{u} h) = -\nabla \cdot \mathbf{q} - \boldsymbol{\tau} : (\nabla \mathbf{u}) + \frac{Dp}{Dt}, \quad (1.3)$$

where  $\mathbf{q}$  denotes the heat flux. The second and third term on the right-hand side of (1.3) represent enthalpy production due to viscous effects and pressure variations. In (1.3), it is assumed that there are no volumetric heat sources.

Finally, conservation of the chemical components is given by transport equations for the species mass fractions, which are defined as  $Y_i = \rho_i / \rho$  with  $\rho_i$  the mass density of species  $i$ . The density of the mixture is the sum of the densities of the various species:  $\rho = \sum_{i=1}^{N_s} \rho_i$ , with  $N_s$  the number of species. The conservation equations for the species mass fractions  $Y_i$  ( $i = 1, \dots, N_s$ ) read

$$\frac{\partial(\rho Y_i)}{\partial t} + \nabla \cdot (\rho \mathbf{u}_i Y_i) = \dot{\omega}_i, \quad (1.4)$$

where  $\dot{\omega}_i$  is the chemical source term and  $\mathbf{u}_i$  the specific velocity of species  $i$ . The chemical source term  $\dot{\omega}_i$  is defined as the mass of species  $i$  that is produced (or consumed) by chemical reactions per unit volume and per unit time. Since chemical reactions are mass conserving, the following relation holds:

$$\sum_i^{N_s} \dot{\omega}_i = 0. \quad (1.5)$$

By introducing the diffusion velocity  $\mathbf{U}_i$  of species  $i$  as

$$\mathbf{U}_i = \mathbf{u}_i - \mathbf{u}, \quad (1.6)$$

the mass balance (1.4) is rewritten in the more commonly used convection-diffusion form

$$\frac{\partial(\rho Y_i)}{\partial t} + \nabla \cdot (\rho \mathbf{u} Y_i) = -\nabla \cdot (\rho \mathbf{U}_i Y_i) + \dot{\omega}_i. \quad (1.7)$$

The set of differential equations (1.1)–(1.3) and (1.7) is completed with two state equations. The caloric equation of state

$$h = \sum_{i=1}^{N_s} Y_i h_i, \quad \text{with} \quad h_i = h_i^{\text{ref}} + \int_{T^{\text{ref}}}^T c_{pi}(T') dT', \quad (1.8)$$

defines the enthalpy  $h$  as a function of temperature  $T$  and species mass fractions assuming that the species are thermally perfect gases. In (1.8)  $h_i$ ,  $h_i^{\text{ref}}$  and  $c_{pi}$  are the specific enthalpy, specific enthalpy of formation at reference temperature  $T^{\text{ref}}$  and specific heat capacity at constant pressure of species  $i$ , respectively. The specific heat capacity at constant pressure of the gas mixture is given by

$$c_p = \sum_{i=1}^{N_s} Y_i c_{pi}, \quad (1.9)$$

with the species heat capacities  $c_{pi}$  well tabulated in polynomial form [42]. In most combustion problems the gas mixture and its components are considered to behave as perfect gases. Therefore, the thermal equation of state is given by the ideal-gas law

$$\rho = \frac{p \bar{M}}{RT}, \quad (1.10)$$

with  $R$  the universal gas constant and  $\bar{M}$  the average molar mass defined as

$$\bar{M} = \left( \sum_{i=1}^{N_s} Y_i / M_i \right)^{-1}, \quad (1.11)$$

where  $M_i$  is the molar mass of species  $i$ . Summarizing, we have found a system of  $N_s + 5$  conservation equations (1.1)–(1.3) and (1.7) and two state equations (1.8) and (1.10), which describe the evolution of  $N_s + 7$  variables:  $\rho$ ,  $\mathbf{u}$ ,  $p$ ,  $h$ ,  $T$  and  $N_s$  species mass fractions  $Y_i$ .

Since the typical flow velocities in laminar flames are much smaller than the speed of sound (the Mach number  $Ma$  is  $O(10^{-3})$ ), the governing equations can be simplified by using the low-Mach number approximation [9]. This low-Mach number approximation is referred to as the Combustion Approximation. By using low-Mach number asymptotics, it can be shown [73] that the leading and first-order pressure in a Mach-number series expansion are functions of time only. Since only open systems are considered in this thesis, the leading-order pressure is not only constant in space, but in time as well. As a result the gas law (1.10) now reads

$$\rho = \frac{p_{\text{amb}} \bar{M}}{RT}, \quad (1.12)$$

with  $p_{\text{amb}}$  the ambient pressure. Furthermore, the pressure term in the energy equation (1.3) vanishes. Moreover, since the term in (1.3) involving the stress tensor is  $O(Ma^2)$  [73], the energy dissipation by viscous forces is usually neglected in laminar combustion as well.

In order to solve the system of conservation equations, models for  $\boldsymbol{\tau}$ ,  $\mathbf{q}$ ,  $\mathbf{U}_i$  and  $\dot{\omega}_i$  are required. A model for the chemical source term  $\dot{\omega}_i$  is given in section 1.3. The stress tensor  $\boldsymbol{\tau}$  of the gas mixture is taken identical to the stress tensor for a single-component Newtonian fluid. Using Stokes' assumption the stress tensor can be expressed as

$$\boldsymbol{\tau} = -\mu (\nabla \mathbf{u} + (\nabla \mathbf{u})^T - \frac{2}{3}(\nabla \cdot \mathbf{u})\mathbf{I}), \quad (1.13)$$

where  $\mu$  is the dynamic viscosity of the mixture and  $\mathbf{I}$  the unit tensor. Although this expression is formally not correct due to the multi-component nature of the mixture, it can be shown that it is accurate for laminar combustion [95].

For the heat flux  $\mathbf{q}$  we use the common expression [95]

$$\mathbf{q} = -\lambda \nabla T + \sum_{i=1}^{N_s} \rho \mathbf{U}_i Y_i h_i, \quad (1.14)$$

with  $\lambda$  the thermal conductivity of the mixture. This expression for  $\mathbf{q}$  takes into account heat transport through conduction and mass diffusion. Heat transport caused by concentration gradients (Dufour effect) and pressure gradients is usually neglected in flame simulations [93].

In general the mixture averaged viscosity  $\mu$  and conductivity  $\lambda$  depend on the temperature and composition of the mixture in a complex way. Therefore, the evaluation of these transport properties is very CPU-intensive (CPU: Central Processing Unit). In order to reduce the computational cost of the simulations presented in this thesis, the transport properties are modelled by using simplified formulations for  $\lambda$  and  $\mu$  for fuel/air mixtures [85]:

$$\lambda/c_p = 2.58 \times 10^{-5} (T/298 \text{ K})^{0.69} \quad \text{kg m}^{-1} \text{ s}^{-1}, \quad (1.15)$$

$$\mu/c_p = 1.67 \times 10^{-8} (T/298 \text{ K})^{0.51} \quad \text{kg}^2 \text{ J}^{-1} \text{ m}^{-1} \text{ s}^{-1}. \quad (1.16)$$

These expressions are found by fitting the results of methane/air flame simulations with more complex transport models. As a result, these models are only accurate for comparable conditions, i.e. fuel/air mixtures, which consist mainly of nitrogen ( $\text{N}_2$ ).

Diffusion of species is caused by concentration gradients, temperature gradients (Soret effect) and pressure gradients [37]. In atmospheric hydrocarbon flames, however, the latter two can be neglected [93]. With this assumption the diffusion velocities  $\mathbf{U}_i$  can be described by the Stefan-Maxwell equation [18]:

$$\nabla X_i = \sum_{j=1}^{N_s} \frac{X_i X_j}{D_{ij}} (\mathbf{U}_j - \mathbf{U}_i), \quad (1.17)$$

where  $X_i = Y_i \bar{M}/M_i$  is the mole fraction of species  $i$ . This expression involves the binary diffusion coefficients  $D_{ij}$ , which are independent of the mixture composition. Since the diffusion velocity of a species depends on the concentration gradients of all other species, the evaluation of (1.17) is very CPU-intensive. Therefore, a simplified model is used for the diffusion velocities. In this thesis, the diffusion velocities are modelled by a Fick-like expression [56], i.e.

$$\mathbf{U}_i Y_i = -D_{im} \nabla Y_i, \quad (1.18)$$

where  $D_{im}$  is the mixture-averaged diffusion coefficient, describing the diffusion of species  $i$  in the mixture. Relation (1.18) is accurate for trace species and applies quite well in premixed fuel/air flames, because  $N_2$  is abundant in this case.

The ratio of thermal conduction to species diffusion is given by the Lewis numbers, defined as

$$Le_i = \frac{\lambda}{\rho D_{im} c_p}. \quad (1.19)$$

By using these Lewis numbers the species diffusion fluxes can be expressed as

$$\rho \mathbf{U}_i Y_i = -\frac{\lambda}{Le_i c_p} \nabla Y_i, \quad (1.20)$$

and the heat-flux vector as

$$\mathbf{q} = -\frac{\lambda}{c_p} \nabla h - \frac{\lambda}{c_p} \sum_{i=1}^{N_s} \left( \frac{1}{Le_i} - 1 \right) h_i \nabla Y_i, \quad (1.21)$$

where we used  $\nabla h = c_p \nabla T + \sum_i^{N_s} h_i \nabla Y_i$ . Using these expressions the set of partial differential equations is cast in its final form:

$$\frac{\partial \rho}{\partial t} + \nabla \cdot (\rho \mathbf{u}) = 0, \quad (1.22)$$

$$\frac{\partial (\rho \mathbf{u})}{\partial t} + \nabla \cdot (\rho \mathbf{u} \mathbf{u}) = -\nabla p - \nabla \cdot \boldsymbol{\tau} + \rho \mathbf{g}, \quad (1.23)$$

$$\frac{\partial (\rho h)}{\partial t} + \nabla \cdot (\rho \mathbf{u} h) - \nabla \cdot \left( \frac{\lambda}{c_p} \nabla h \right) = \nabla \cdot \left( \frac{\lambda}{c_p} \sum_{i=1}^{N_s} \left( \frac{1}{Le_i} - 1 \right) h_i \nabla Y_i \right), \quad (1.24)$$

$$\frac{\partial (\rho Y_i)}{\partial t} + \nabla \cdot (\rho \mathbf{u} Y_i) - \nabla \cdot \left( \frac{\lambda}{Le_i c_p} \nabla Y_i \right) = \dot{\omega}_i, \quad i = 1, \dots, N_s. \quad (1.25)$$

Since the  $N_s$  species equations (1.25) together with the continuity equation (1.22) are over-complete, only  $N_s - 1$  species equations (1.25) are solved. The solution for the abundant species ( $i = N_s$ ) and its effective Lewis number follow from the constraints

$$\sum_{i=1}^{N_s} Y_i = 1 \quad \text{and} \quad \sum_{i=1}^{N_s} \mathbf{U}_i Y_i = 0. \quad (1.26)$$

In order to reduce the computational cost the Lewis numbers of the trace species are assumed to be constant.

For the analysis furtheron in this thesis, it is instructive to consider the element mass fractions  $Z_j$  defined as

$$Z_j = \sum_{i=1}^{N_s} w_{ji} Y_i, \quad j = 1, \dots, N_e, \quad (1.27)$$

where  $w_{ji}$  denotes the mass fraction of element  $j$  in species  $i$ . Conservation equations for the  $N_e$  element mass fractions can be derived by taking the proper linear combination of (1.25):

$$\frac{\partial(\rho Z_j)}{\partial t} + \nabla \cdot (\rho \mathbf{u} Z_j) - \nabla \cdot \left( \frac{\lambda}{c_p} \nabla Z_j \right) = \nabla \cdot \left( \frac{\lambda}{c_p} \sum_{i=1}^{N_s} \left( \frac{1}{Le_i} - 1 \right) w_{ji} \nabla Y_i \right). \quad (1.28)$$

These equations are, of course, *not* independent of the set (1.25). Note the resemblance between (1.24) and (1.28). Both equations do not contain a chemical source term, which implies that  $Z_j$  and  $h$  in a flame are only influenced by convection and diffusion. Moreover, in case of Lewis numbers equal to 1 ( $Le_i = 1$ ) the terms involving  $\nabla Y_i$  drop out and all element mass fractions and the enthalpy behave exactly the same.

In this section we have formulated the equations describing a laminar flame using a number of assumptions and approximations. Nevertheless, the equations presented here have proven to be accurate for laminar hydrocarbon/air flames and are used in many numerical studies (e.g. [40, 69, 81]). It is worth mentioning that the reduction method presented in this thesis does not rely on these assumptions and can be used, for instance, in combination with more complex models for the transport properties as well.

### 1.3 Combustion chemistry

In the previous section the governing equations are introduced, but the chemical source terms  $\dot{\omega}_i$  appearing in the species balance equations are not specified yet. The oxidation of hydrocarbon fuels is governed by many elementary reaction steps. Before presenting the general expression for the chemical source term, the contribution of only one elementary reaction is considered. As an example we consider the reaction



in which oxygen ( $\text{O}_2$ ) and atomic hydrogen ( $\text{H}$ ) react and form the radicals hydroxyl ( $\text{OH}$ ) and oxygen ( $\text{O}$ ). The reaction rate  $r_f$  is assumed to be proportional to the concentrations of the reactants:

$$r_f = k_f [\text{O}_2] [\text{H}], \quad (1.30)$$

where the square brackets denote the concentration  $\rho Y_i / M_i$  of species  $i$  and  $k_f$  the reaction rate coefficient. The subscript  $f$  indicates that the forward reaction is considered. The reaction rate coefficient is usually written in a modified Arrhenius form [93]

$$k_f = A T^\beta \exp(-E_a / RT), \quad (1.31)$$

with  $A$  and  $\beta$  reaction constants and  $E_a$  the activation energy ( $\text{J mol}^{-1}$ ). For a homogeneous system, the concentration of the species involved will change in time due to reaction (1.29) as follows:

$$\frac{d[\text{OH}]}{dt} = \frac{d[\text{O}]}{dt} = -\frac{d[\text{O}_2]}{dt} = -\frac{d[\text{H}]}{dt} = r_f. \quad (1.32)$$

In general, the species may also react in opposite direction:



The reaction rate of this reversed reaction is denoted by  $r_r$  and the net reaction rate of the forward and reversed reactions (1.29) and (1.33) is given by

$$r = r_f - r_r = k_f[\text{O}_2][\text{H}] - k_r[\text{OH}][\text{O}]. \quad (1.34)$$

The reaction coefficient of the reversed reaction  $k_r$  can be obtained by using the equilibrium constant  $k_{\text{eq}}$

$$k_{\text{eq}}(p, T) = \frac{k_f}{k_r}, \quad (1.35)$$

which is well defined by thermodynamic properties of the species involved in the reaction [87]. The use of (1.35) to compute  $k_r$  from  $k_f$  and  $k_{\text{eq}}$  results in a much more accurate prediction of the chemical equilibrium composition, than when a similar expression as (1.31) is used for  $k_r$ .

In general, a chemical reaction  $j$  can be written as



where  $\mathcal{M}_i$  represents species  $i$  and  $\nu_{ij} = \nu''_{ij} - \nu'_{ij}$  the stoichiometric coefficients, which indicate how many molecules of species  $i$  take part in reaction  $j$ . In a practical gas-phase combustion system the reaction order,  $\sum_{i=1}^{N_s} \nu'_{ij}$ , of the reactions involved will not exceed three. Reaction (1.29) is an example of a second-order reaction, which is the most common and least complicated type of reaction. Two other important reaction types are the dissociation reaction and its counterpart the recombination reaction, which are first and third order, respectively. At not too high densities (pressures below 100 bar) the probability of a collision between four or more molecules is so small, that the influence of these higher-order reactions may be neglected.

The general expression for the reaction rate of reaction (1.36) reads

$$r_j = k_{fj} \prod_{i=1}^{N_s} [\mathcal{M}_i]^{\nu'_{ij}} - k_{rj} \prod_{i=1}^{N_s} [\mathcal{M}_i]^{\nu''_{ij}}. \quad (1.37)$$

The total source term as it appears in the conservation equations for the species (1.25), contains the contribution of all chemical reactions, viz.

$$\dot{\omega}_i = M_i \sum_{j=1}^{N_r} \nu_{ij} r_j, \quad (1.38)$$

where  $N_r$  is the total number of reactions.

The reactions and their rate constants  $A$ ,  $\beta$  and  $E_a$  are listed in so-called reaction mechanisms or reaction schemes. Comprehensive and well-tested reaction schemes for natural gas combustion are provided by several research groups, e.g. [45, 83, 93]. These reaction schemes describe several hundred elementary reactions between more than 50 species. In this work we have used the mechanism from Smooke [85] as base mechanism for the reduced computations. Since this mechanism represents only a minimal subset of the complete mechanism, it is sometimes referred to as a skeletal mechanism. This skeletal mechanism does not include the path to higher hydrocarbons, but considers only  $\text{C}_1$  chemistry

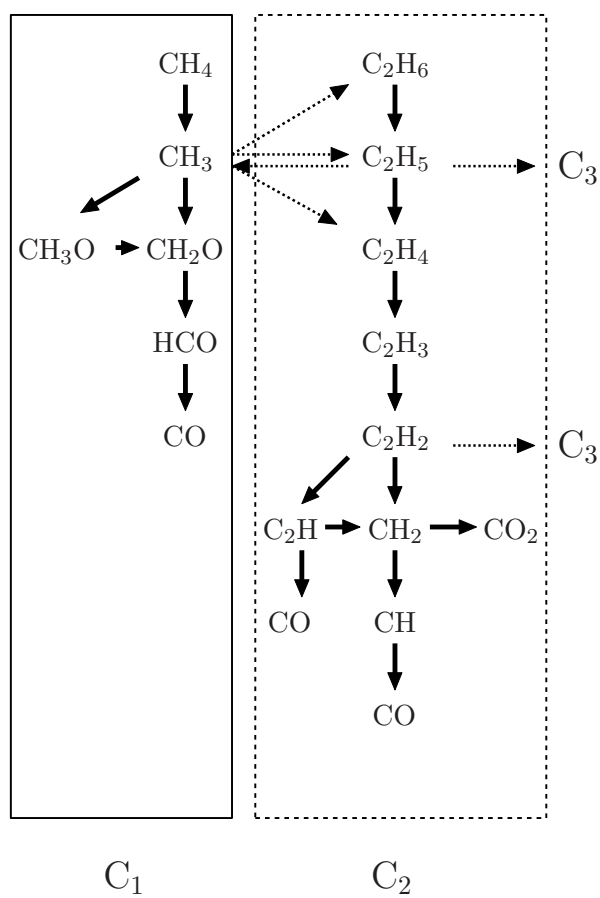


**Figure 1.1.** Main reaction path in methane combustion for not too fuel-rich conditions [92]. The dashed box describes what is usually referred to as the C<sub>2</sub> chain. The C<sub>1</sub> chain is shown in the box on the left.

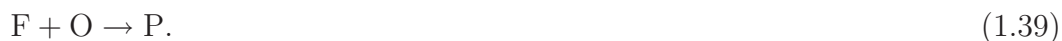
(see figure 1.1). However, it is claimed to predict the most important flame features well for fuel-lean methane/air flames. This skeletal mechanism consists of only 16 species and 25 reversible reactions and is therefore less CPU-intensive and thus more attractive to use in detailed flame computations than the mechanisms mentioned above. The species, their Lewis numbers and the reactions with their reaction constants are listed in appendix A. The use of this skeletal mechanism is not essential for the reduction method presented in this thesis. The method is a general reduction technique, which can be applied to any reaction mechanism.

## 1.4 Reduced chemical models

In order to simulate combustion processes the conservation equations for mass, momentum and energy presented in the previous sections have to be solved. Furthermore, for each species in the reaction mechanism a balance equation has to be considered. Solving the set of partial differential equations (1.22)–(1.25) is the key problem in combustion modelling. As the number of species involved is generally quite large, not only a large number of equations has to be solved, but the chemical source terms in these equations contain contributions of even more reactions. The highly non-linear chemical source term causes a strong coupling between the different equations. Furthermore, the different reactions in the chemical source term describe processes with a wide range of time scales [54]. This causes the set of equations to be stiff, which implies that very small time steps or special numerical techniques have to be used to solve the system. Despite of all these difficulties, numerical simulations of flames with detailed reaction mechanisms have been reported in the literature by several authors (see e.g. [14, 60, 88]). However, these simulations are restricted to simple geometries and their computational times often exceed days, prohibiting an extensive study on the effect of different parameters.

In the last ten years, a lot of effort has been put in the development of methods to reduce the computation time of flame simulations. One way to achieve this is using sophisticated numerical methods to solve the governing set of equations. State-of-the-art in this field of combustion research is the use of multi-grid solvers [22, 38], parallel computing [88] and local grid refinement [2, 3].

Another way to reduce the computational cost of flame simulations is to simplify the chemical reaction model. A classical approach describing the chemistry in flames was developed by Zeldovich and Kamenetzki [98]. They presume that all chemical reactions can be summarized in a single, global one-step reaction, combining fuel  $F$  and oxidizer  $O$  to products  $P$ ,



More recently, various authors have proposed reaction mechanisms consisting of a few global reaction steps. A major problem using these 'ad-hoc' global mechanisms is that the reaction parameters required for the computation of the chemical source term cannot be derived from elementary kinetic data. Instead, the reaction parameters are obtained by fitting the results to experiments [50, 53] or computations with detailed chemistry [94]. This limits the applicability of these models to the mostly small range of conditions they are developed for. Extrapolation to other conditions may result in unrealistic behaviour. Although global mechanisms have been applied in many combustion simulations (e.g. [3, 51]), their lack of accuracy causes them to be useful for global studies only.

More accurate chemical reduction techniques are based on the observation that a typical combustion system contains many chemical processes with a much smaller time scale than the flow time scales. These fast chemical processes can be decoupled, reducing the stiffness of the system and thus increasing the computational efficiency. The most prominent reduction methods are the reduction technique introduced by Peters and Williams [66, 63], the computational singular perturbation (CSP) method from Lam and Goussis [46] and the intrinsic low-dimensional manifold (ILDM) approach of Maas and Pope [54]. Each of these methods identifies the fast chemical processes in a different manner.

### Conventional reduction technique

In the conventional reduction technique partial-equilibrium and steady-state assumptions are invoked for particular reactions and species that are associated with fast processes. A steady-state approximation simply states that for a certain species the chemical reactions balance, i.e. for species  $i$

$$\dot{\omega}_i = M_i \sum_{j=1}^{N_r} \nu_{ij} r_j = 0. \quad (1.40)$$

Equation (1.40) results in an algebraic equation (involving contributions of many reactions) for each species considered to be in steady state. Obviously, the nomenclature stems from the description of a homogeneous reacting system, where this equation implies that the time derivative of the concentration of species  $i$  is zero. In a flame, it implies that the time scales of the reactions producing or consuming a steady-state species are much shorter than the time scales related to convection and diffusion.

When the first  $N_{st}$  species are assumed to be in steady state, their conservation equations are replaced by (1.40) and the set of equations (1.25) becomes

$$0 = \dot{\omega}_i \quad i = 1, \dots, N_{st}, \quad (1.41)$$

$$\frac{\partial(\rho Y_i)}{\partial t} + \nabla \cdot (\rho \mathbf{u} Y_i) - \nabla \cdot \left( \frac{\lambda}{Le_i c_p} \nabla Y_i \right) = \dot{\omega}_i \quad i = N_{st} + 1, \dots, N_s. \quad (1.42)$$

Due to the application of the algebraic steady-state relations not only the number of differential equations is reduced, but also their stiffness, since the differential equations for the species with the fastest time scales are removed from the set of differential equations. However, if no further assumptions are made, the steady-state relations (1.41) form a set of non-linear coupled algebraic equations, which is not easy to solve. To reduce the complexity of this set and, even more, to obtain explicit expressions for the steady-state species, the steady-state expressions (1.40) can be truncated by considering the largest terms in (1.40) only [63, 86].

In the conventional reduction technique, the selection of the steady-state species is done by hand, which requires a deep insight of the user in the chemical kinetics. A detailed investigation of the reaction paths and the time scales in the chemical reaction mechanism should give information about which species are closest to steady state. For higher hydrocarbon fuels with reaction mechanisms consisting of hundreds of reactions this is a complicated task. Furthermore, the conventional reduction technique is a global method, which means that the same species are assumed in steady state at different conditions in different systems. However, it depends on the local conditions which species are in quasi-steady state. Species, which can be assumed in steady state at e.g. high temperatures, may

be not in steady state at lower temperatures. In general, a reduced reaction mechanism will not yield accurate results outside the range of conditions for which it is developed.

In view of these problems, the time-scale analysis in the CSP and ILDM method is performed automatically, based on the local Jacobian of the chemical source term. The CSP method uses computational singular perturbation to identify the fast time scales. Since this is done dynamically, the number and identity of the steady-state species may vary during the combustion process. Although this technique is very accurate, its applicability to complex simulations is questionable due to its high computational cost. Recently, Massias *et al.* [58] used the CSP method to construct global reduced mechanisms. By averaging the local CSP data over the computational domain of a simple test problem, global characteristics of the dynamics are computed. Since global mechanisms are fixed throughout the domain, they are more efficient to use. However, it must be noted that the accuracy of the local CSP method is lost in this way.

### Intrinsic low-dimensional manifolds

In this section we discuss the ILDM method introduced by Maas and Pope [54]. It is explained more extensively than the other reduction techniques, because the reduction method presented in this thesis is based on the ILDM method. Since the description given here is certainly not complete, the reader is referred to e.g. [5, 25, 54] for a more elaborate discussion of ILDM.

The ILDM method identifies the fast processes by using an eigenvalue analysis of the local Jacobian of the chemical source term. In order to study the chemical nature of the reaction system, the convection and diffusion terms in (1.25) are omitted. This yields the following differential equations for a homogeneous time-dependent system:

$$\frac{dY_i}{dt} = W_i, \quad i = 1, \dots, N_s, \quad (1.43)$$

where  $W_i = \dot{\omega}_i/\rho$ . The composition of a mixture, which is given by the mass fractions of all species, can be written in vector notation as  $\mathbf{Y} = (Y_1, \dots, Y_{N_s})^T$ . In vector notation (1.43) reads

$$\frac{d\mathbf{Y}}{dt} = \mathbf{W}, \quad (1.44)$$

with  $\mathbf{W} = (W_1, \dots, W_{N_s})^T$  the chemical source term. The vector notation is associated with the description of the mixture in a  $N_s$ -dimensional space, which is called the composition space. When a set of basis vectors is defined corresponding to the species, the mass fractions are the coordinates in the composition space. Formally, the pressure and enthalpy are needed to describe the complete composition of the mixture, yielding a  $(N_s + 2)$ -dimensional composition space. However, since  $p$  and  $h$  are constant here, they are omitted in the vector notation.

To identify the fast and slow chemical processes, the chemical source term  $\mathbf{W}$  is linearized around the reference composition  $\mathbf{Y}^0$ :

$$\frac{d\mathbf{Y}}{dt} \approx \mathbf{W}(\mathbf{Y}^0) + \mathbf{J}(\mathbf{Y}^0)(\mathbf{Y} - \mathbf{Y}^0), \quad (1.45)$$

where  $\mathbf{J}(\mathbf{Y}^0)$  is the  $N_s \times N_s$  Jacobian matrix with elements  $J_{ij} = \partial W_j / \partial Y_i |_{\mathbf{Y}^0}$ . The local characteristics of the system can be examined by transforming (1.45) into the basis of

eigenvectors of the Jacobian matrix. The Jacobian matrix is therefore diagonalized as follows

$$\mathbf{J} = \mathbf{S}\mathbf{\Lambda}\mathbf{S}^{-1}, \quad (1.46)$$

where  $\mathbf{\Lambda}$  is a diagonal matrix with the eigenvalues  $\lambda_i$ . The columns of matrix  $\mathbf{S}$  are the right eigenvectors  $\mathbf{s}_i$  of the Jacobian matrix. By using the transformation  $\mathbf{Y} = \mathbf{S}\hat{\mathbf{Y}}$ , equation (1.45) can be written in the basis of eigenvectors:

$$\frac{d\hat{\mathbf{Y}}}{dt} = \hat{\mathbf{W}}^0 + \mathbf{\Lambda}(\hat{\mathbf{Y}} - \hat{\mathbf{Y}}^0), \quad (1.47)$$

with  $\hat{\mathbf{W}}^0 = \mathbf{S}^{-1}\mathbf{W}(\mathbf{Y}^0)$ . As a result of this transformation, the differential equations in (1.47) are decoupled and the evolution of each mode  $\hat{Y}_i$  is described by

$$\frac{d\hat{Y}_i}{dt} = \hat{W}_i^0 + \lambda_i(\hat{Y}_i - \hat{Y}_i^0). \quad (1.48)$$

This equation gives us the basis for a time-scale analysis of the different modes. When the absolute value of the eigenvalue  $\lambda_i$  is small, the typical time scale of the corresponding mode is given by  $(\hat{W}_i^0)^{-1}$ . On the other hand, if the absolute value of the real part of the eigenvalue is large, the time scale is given by  $\lambda_i^{-1}$ . If the magnitude of  $\lambda_i$  is large, movements in the direction of the associated eigenvector will proceed fast. Depending on the sign of the real part of the eigenvalues we can distinguish between different kinds of behaviour. Modes with a positive real part of the eigenvalue will grow exponentially in time. For negative real parts of the eigenvalues the corresponding processes will relax towards a steady state. It can be shown [25] that modes with  $\lambda_i = 0$  correspond to conserved quantities such as an element mass fraction.

Considering the behaviour of the different reaction modes, it can be concluded that the introduction of steady-state equations is most suitable for modes corresponding to eigenvalues with large negative real parts. If the modes are ordered in such a way that the eigenvalues with the lowest index correspond to the fastest damping processes, the steady-state equations may be written as

$$(\mathbf{s}_i^L, \mathbf{W}) = 0, \quad i = 1, \dots, N_{\text{st}}, \quad (1.49)$$

where  $\mathbf{s}_i^L$  are the left eigenvectors of the Jacobian matrix. Since the analysis is based on the local Jacobian matrix, the combination of species in steady state changes in composition space. The collection of all points in composition space which satisfy (1.49), form a  $(N_s - N_{\text{st}})$ -dimensional subspace: the intrinsic low-dimensional manifold. In figure 1.2 it is schematically shown how a reaction trajectory is rapidly attracted to the manifold due to the fast chemical processes. The subsequent movement in the manifold is much slower. In the reduced model the fast chemical processes are assumed in steady state and only movements within the manifold are allowed.

Because the numerical solution of (1.49) is computationally expensive, the manifold is computed in a pre-processing step before the actual flame modelling, instead of solving the steady-state equations at run-time as in the conventional reduction method. For application in flame simulations, the manifold is parametrized by so-called controlling variables and it is tabulated in a look-up table. This is done once for a given mixture and, subsequently, this database can be used in a series of combustion calculations.

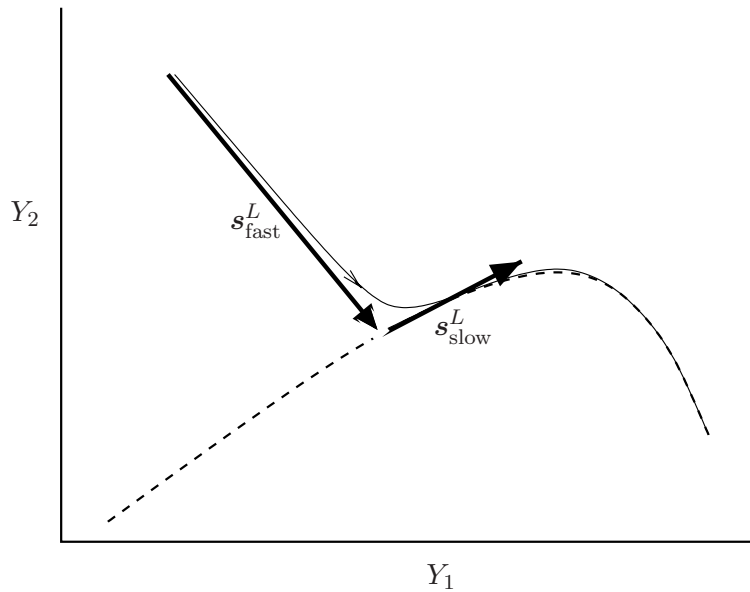


**Figure 1.2.** Fast and slow chemical processes in composition space. The thick arrows represent the left eigenvectors  $s_{fast}^L$  and  $s_{slow}^L$  corresponding to the fast and slow chemical processes, respectively. The reaction path (thin solid curve) is attracted towards the manifold (dashed line).

Since the composition of a mixture in the manifold is completely described by a relatively small number ( $N_s - N_{st}$ ) of controlling variables, conservation equations have to be solved for these slowly changing variables only, which reduces the computational cost. Additionally, the chemical source terms can be computed in advance and stored in the database, which makes a CPU-intensive evaluation of (1.38) at run-time unnecessary resulting in a much faster flame simulation. The dimension of the look-up table is determined by the number of controlling variables that is needed to describe the slow chemical processes. Or in other words: by the number of processes that can be assumed in steady state. For simple fuels like CO/H<sub>2</sub> mixtures, two controlling variables appear to be sufficient [26, 55]. However, for an accurate reproduction of the burning velocity of premixed methane/air flames at least three degrees of freedom are needed [25]. Together with variations in enthalpy, pressure and element composition that can occur in combustion systems, this results in a high-dimensional look-up table.

Concluding, ILDM is a reduction method that identifies the fast chemical processes by a local eigenvalue analysis of the chemical source term. ILDM has proven to be a very successful method, which has been applied in many flame simulations (e.g. [26, 54, 77]). However, due to the large number of controlling variables that is needed to get an accurate prediction of the burning velocity, ILDM seems to be complicated for higher hydrocarbon fuels in case of premixed flames.

## 1.5 Purpose of this study

The reduction methods discussed in the previous sections are based on the assumption that a large number of species (or linear combinations of them) is in steady state. This implies that the different contributions in the chemical source term are assumed to be

much larger than the other terms in (1.25). Therefore, the left-hand side of (1.25) can be neglected for these species, leaving a balance between the chemical reactions. A drawback of using steady-state relations is that they only hold in high-temperature regions of a flame, where the reaction rates are high and where chemistry is dominant. In 'colder' regions of a flame, however, convection and diffusion cannot be neglected and an increased number of controlling variables is needed to describe the slow chemical processes. Furthermore, there is an important region between the preheat zone and the reaction layer where reaction and diffusion are in balance.

In this thesis a new method to create low-dimensional manifolds is introduced. This method is not only based on 'chemical' assumptions, but it also takes the most important transport processes into account. It shares the idea with so-called flamelet approaches [62, 33] that a multi-dimensional flame can be considered as a set of one-dimensional (1D) flames: *flamelets*. This implies that the path followed in composition space in case of multi-dimensional flames will be close to the path found in 1D flames. Therefore, the chemical compositions in flamelets are used to construct a manifold in this new method. The resulting manifold is referred to as a *Flamelet-Generated Manifold* (FGM<sup>1</sup>).

It is expected that FGM coincides with the ILDM in high-temperature regions, but will be a better approximation of the mixture composition in 'colder' zones of laminar premixed flames than the ILDM, since the main parts of convection and diffusion are taken into account. Besides the objective of validating this conjecture, the consequences are investigated for the number of controlling variables that is needed to represent the combustion process.

Flame stretch, curvature and unsteady effects are not present in the flamelets that are used to construct the FGM. These processes play, however, an important role in multi-dimensional flames. Which (physical) processes must be included in the FGM and which terms may be neglected is studied. Furthermore, it is examined how flame stretch affects the accuracy of the FGM method, to what extent, and how to deal with it.

Another interesting aspect of reduced chemical models is their applicability. FGM is developed for premixed laminar flames, while ILDM can be applied to more types of combustion processes: premixed, non-premixed, laminar and turbulent. We investigate whether FGM is limited to premixed laminar flames and if not, how large the deviations from premixed laminar flame behaviour may be.

The main goal of reduction methods is to reduce the computational cost of flame simulations without losing too much accuracy, and eventually, to make it possible to treat more realistic problems. In this thesis it is also studied whether FGM can be used as an efficient tool for flame simulations in more complex combustion systems.

## 1.6 Outline

In the foregoing sections the governing equations for reacting flow have been presented. Some modelling problems when using complex chemistry and their possible solutions have been discussed in section 1.4. In the remaining part of this thesis, the FGM method is presented and applied to (partially) premixed laminar flames.

The FGM method is introduced in chapter 2. First a set of flamelet equations is derived, starting from the full set of transport equations (1.22)–(1.25). Then it is demonstrated how

---

<sup>1</sup>The abbreviations ILDM and FGM are used for both the manifold itself and the reduction method as a whole.

the solutions of the set of flamelet equations can be used to construct a manifold. The application of FGM in combustion simulations is discussed as well. Some test results for 1D and 2D burner-stabilized methane/air flames are presented in section 2.4.

Flame stretch and curvature effects play an important role in realistic flames. Since a FGM is constructed by using 1D stretchless flamelets, these multi-dimensional effects are not included in the manifold. The influence of flame stretch on the accuracy of FGM is investigated in chapter 3. In order to isolate the effects of flame stretch, the FGM method is applied to premixed counterflow flames, which are not influenced by other multi-dimensional perturbations. Special attention is given to the burning velocity of these stretched flames.

In chapter 4 the application of FGM to partially-premixed flames is discussed. In order to deal with variations in the mixture fraction, which occur in partially-premixed flames, the manifold is extended with an additional controlling variable. This extended manifold is used to compute so-called triple flames. The propagation speed and the local burning velocity of these triple flames are studied. Especially, the effects of flame stretch and curvature on the local mass burning rate are investigated.

In chapter 5 it is studied whether FGM can be used to perform accurate and efficient simulations of premixed laminar flames in complex burner systems. A semi-practical furnace is modelled and the results are compared with temperature measurements in an experimental setup. Finally, summarizing conclusions are given in chapter 6.

# Flamelet-Generated Manifolds

## 2.1 Flamelet equations

The FGM method shares its basic assumption with flamelet methods, that a multi-dimensional flame can be considered as a set of 1D flamelets. Therefore, the compositions in 1D flames will be representative for the compositions in more general flames as well. In this section a set of 1D flamelet equations is derived following the basic ideas of De Goeij and Ten Thijs Boonkkamp [32, 33]. In the following sections it is explained how this set of flamelet equations can be used to construct a FGM.

A premixed flame is defined as the region in space, where a scalar variable  $\mathcal{Y}$  assumes values between  $\mathcal{Y}_u = 0$  in the unburnt gases and  $\mathcal{Y}_b = 1$  in the burnt gases. The subscripts  $u$  and  $b$  denote variables associated with the unburnt and burnt mixture, respectively. The variable  $\mathcal{Y}$  can be any linear combination of species mass fractions, which obeys  $\nabla\mathcal{Y} \neq 0$ . A 'flame surface' is defined as an iso-surface of  $\mathcal{Y}$ , i.e. a surface at which  $\mathcal{Y}(\mathbf{x}, t) = \text{const.}$  The motion of such a surface is described by the kinematic equation

$$\frac{d\mathcal{Y}}{dt} := \frac{\partial\mathcal{Y}}{\partial t} + \mathbf{u}_f \cdot \nabla\mathcal{Y} = 0, \quad (2.1)$$

stating that a point on a flame surface stays on this surface for all  $t$ . The local velocity of a flame surface  $\mathbf{u}_f$  is determined by a balance between the local fluid velocity  $\mathbf{u}$  and the local burning velocity  $s_L$ :

$$\mathbf{u}_f = \mathbf{u} + s_L \mathbf{n}. \quad (2.2)$$

The burning velocity is defined as the velocity at which the flame surface propagates normal to itself and relative to the flow in the unburnt mixture. The local normal vector  $\mathbf{n}$  can be determined from the scalar field  $\mathcal{Y}$ ,

$$\mathbf{n} = -\frac{\nabla\mathcal{Y}}{|\nabla\mathcal{Y}|}, \quad (2.3)$$

directed to the unburnt gas mixture. As figure 2.1 shows, the tangential component of the flame surface velocity is equal to the tangential component of the fluid velocity and the difference  $\rho(\mathbf{u} - \mathbf{u}_f)$  normal to the flame surface is equal to the amount of mass effectively consumed by the flame. Substitution of (2.2) in (2.1) leads to the kinematic equation

$$\frac{\partial\mathcal{Y}}{\partial t} + \mathbf{u} \cdot \nabla\mathcal{Y} = s_L |\nabla\mathcal{Y}|. \quad (2.4)$$

This equation is very similar to the well-known kinematic  $G$ -equation first introduced by Williams [96], which describes the motion of a single flame sheet ( $\mathcal{Y} = \mathcal{Y}^0$ ). However,

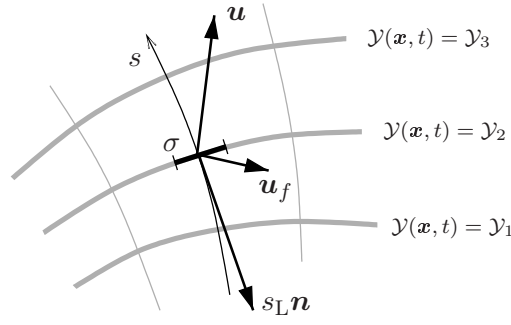


Figure 2.1. Flamelet system adapted to iso-surfaces of  $\mathcal{Y}$ .

important differences are that (2.4) describes the motion of all flame surfaces with  $\mathcal{Y}_u < \mathcal{Y} < \mathcal{Y}_b$ , and that  $s_L$  is a field quantity in (2.4), while in the  $G$ -equation it is defined at the flame sheet only.

In [32], De Goeij and Ten Thijs Boonkcamp proposed the stretch rate  $K$  as the relative rate of change of the mass  $M(t)$ , defined as

$$M(t) = \int_{V(t)} \rho \, dV, \quad (2.5)$$

contained in an infinitesimal volume  $V(t)$  in the flame, moving with velocity  $\mathbf{u}_f$ :

$$K = \frac{1}{M} \frac{dM}{dt}. \quad (2.6)$$

Applying Reynolds' transport theorem to  $M(t)$  in (2.5) gives the following expression for the scalar field quantity  $K$ :

$$\rho K = \frac{\partial \rho}{\partial t} + \nabla \cdot (\rho \mathbf{u}_f). \quad (2.7)$$

Together with (2.2) this expression can be used to rewrite the continuity equation (1.22):

$$\nabla \cdot (\rho s_L \mathbf{n}) = \rho K, \quad (2.8)$$

where all distortions from local 1D flame behaviour are combined in the right-hand side term  $\rho K$ . Apart from the usual terms related to flame curvature and flow straining, this definition of  $K$  incorporates additional contributions, for instance due to flame thickness variations. A physical interpretation of the different contributions to flame stretch is presented in [32].

The conservation equation for the scalar variable  $\mathcal{Y}$  reads

$$\frac{\partial(\rho \mathcal{Y})}{\partial t} + \nabla \cdot (\rho \mathbf{u} \mathcal{Y}) - \nabla \cdot \left( \frac{\lambda}{Le_{\mathcal{Y}} c_p} \nabla \mathcal{Y} \right) - \dot{\omega}_{\mathcal{Y}} = 0, \quad (2.9)$$

with  $Le_{\mathcal{Y}}$  and  $\dot{\omega}_{\mathcal{Y}}$  generally depending on the other field variables in the flame. Using the kinematic equation (2.4) and equations (2.7) and (2.2), the following equation for  $\mathcal{Y}$  is found rigorously

$$-\nabla \cdot (\rho s_L \mathbf{n} \mathcal{Y}) - \nabla \cdot \left( \frac{\lambda}{Le_{\mathcal{Y}} c_p} \nabla \mathcal{Y} \right) - \dot{\omega}_{\mathcal{Y}} = -\rho K \mathcal{Y}, \quad (2.10)$$

with all transport terms along the flame surfaces gathered in the right-hand-side term  $-\rho K\mathcal{Y}$ . Introducing the mass burning rate  $m = \rho s_L$ , the arc-length perpendicular to the flame surfaces  $s$  and the variable  $\sigma$ , which is a measure for the flame surface through which transport takes place (cf. figure 2.1), equation (2.10) can be written in quasi-1D form normal to the flame surfaces:

$$\frac{\partial}{\partial s}(\sigma m \mathcal{Y}) - \frac{\partial}{\partial s} \left( \sigma \frac{\lambda}{Le_Y c_p} \frac{\partial \mathcal{Y}}{\partial s} \right) - \sigma \dot{\omega}_Y = -\sigma \rho K \mathcal{Y}. \quad (2.11)$$

The derivative of  $\sigma$  is related to the curvature  $\kappa$  of the flame surface via

$$\kappa = \nabla \cdot \mathbf{n} = -\frac{1}{\sigma} \frac{\partial \sigma}{\partial s}. \quad (2.12)$$

Using this expression for  $\kappa$ , (2.11) becomes

$$\frac{\partial}{\partial s}(m \mathcal{Y}) - \frac{\partial}{\partial s} \left( \frac{\lambda}{Le_Y c_p} \frac{\partial \mathcal{Y}}{\partial s} \right) - \dot{\omega}_Y = -\rho K \mathcal{Y} + \kappa F_Y, \quad (2.13)$$

where all perturbations from 1D flat flame behaviour are gathered at the right-hand side. In (2.13) we introduced  $F_Y$  as a short-hand notation for the convective and diffusive flux of  $\mathcal{Y}$ . Using similar notations for the fluxes of the species mass fractions and the enthalpy, i.e.

$$F_i = m Y_i - \frac{\lambda}{Le_i c_p} \frac{\partial Y_i}{\partial s}, \quad (2.14)$$

and

$$F_h = m h - \frac{\lambda}{c_p} \frac{\partial h}{\partial s} - \frac{\lambda}{c_p} \sum_{i=1}^{N_s} \left( \frac{1}{Le_i} - 1 \right) h_i \frac{\partial Y_i}{\partial s}, \quad (2.15)$$

the full set of conservation equations can be cast in a quasi-1D form, which we refer to as the flamelet equations:

$$\frac{\partial m}{\partial s} = -\rho K + \kappa m, \quad (2.16)$$

$$\frac{\partial F_i}{\partial s} - \dot{\omega}_i = -\rho K Y_i + \kappa F_i + Q_i, \quad (2.17)$$

$$\frac{\partial F_h}{\partial s} = -\rho K h + \kappa F_h + Q_h. \quad (2.18)$$

This set of equations describes the internal structure of the flame front in terms of  $Y_i(s)$ ,  $h_i(s)$  and the mass burning rate  $m(s)$  for a flamelet with a particular stretch field  $K(s)$  and curvature field  $\kappa(s)$ . When the set (2.16)–(2.18) is solved in combination with the kinematic equation (2.1) for all flame surfaces, the full set of conservation equations for species and enthalpy is solved. The terms  $Q_i$  and  $Q_h$  describe transport along the flame surfaces, which arises because the local iso-surfaces of the variables  $Y_i$  and  $h$  generally do not coincide with iso-surfaces of  $\mathcal{Y}$ . The terms  $Q_i$  and  $Q_h$  are given by

$$Q_i = \rho(\mathbf{u}_{fi} - \mathbf{u}_f) \cdot \nabla Y_i + \nabla \cdot \left( \frac{\lambda}{Le_i c_p} \nabla_{\parallel} Y_i \right), \quad (2.19)$$

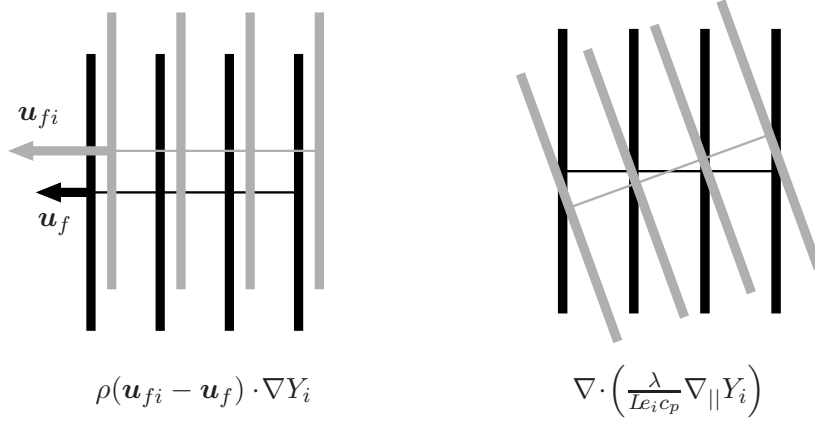


**Figure 2.2.** Schematic representation of the different contributions in  $Q_i$ . The black and gray lines denote iso-surfaces of  $\mathcal{Y}$  and  $Y_i$ , respectively.

and

$$Q_h = \rho(\mathbf{u}_{fh} - \mathbf{u}_f) \cdot \nabla h + \nabla \cdot \left( \frac{\lambda}{c_p} \nabla_{\parallel} h + \frac{\lambda}{c_p} \sum_{i=1}^{N_s} \left( \frac{1}{L_{e_i}} - 1 \right) h_i \nabla_{\parallel} Y_i \right), \quad (2.20)$$

with  $\mathbf{u}_{fi}$  and  $\mathbf{u}_{fh}$  the local velocities of the iso-surfaces of  $Y_i$  and  $h$ , respectively. In (2.19) and (2.20),  $\nabla_{\parallel}$  denotes the nabla operator in tangential direction only. As shown in figure 2.2, the first term on the right-hand side of (2.19) represents the relative movement of the iso-surfaces of  $Y_i$  with respect to the iso-surfaces of  $\mathcal{Y}$ . The second term denotes the diffusive transport of  $Y_i$  along the iso-surfaces of  $\mathcal{Y}$ .

So far, no approximations have been made. The set of flamelet equations (2.16)–(2.18) are found rigorously from the full set of conservation equations (1.22)–(1.24) by using the stretch rate equation (2.7) and the kinematic equation (2.4). All perturbations from local 1D flat flame behavior are gathered in the right-hand sides of the flamelet equations. It is expected that in most situations in premixed laminar flames these perturbations are small compared to the other terms in the flamelet equations, although this might not be justified under extreme circumstances, such as near local flame quenching. The stretch terms in (2.16)–(2.18) can be neglected when the Karlovitz number is small:

$$Ka = \frac{K \delta_f}{s_L} \ll 1, \quad (2.21)$$

with  $\delta_f$  the flame thickness. Curvature effects are negligible when the curvature radius  $\kappa^{-1}$  of the flame surfaces is much larger than the flame thickness:

$$|\kappa^{-1}| \gg \delta_f. \quad (2.22)$$

If the transient time scales are longer than the flame time scale  $\delta_f/s_L$ , the first term in  $Q$  can be neglected as well. The second term in  $Q$  was computed numerically for the tip of a 2D Bunsen flame in [31] and it appeared to be very small. The approximation that this term is negligible, is related to the assumption that the length scales of the distortions along the flame surfaces are much larger than the flame thickness.

If all perturbations from 1D flat-flame behaviour are neglected, the following set of 1D equations remains:

$$\frac{\partial m}{\partial s} = 0, \quad (2.23)$$

$$\frac{\partial(mY_i)}{\partial s} - \frac{\partial}{\partial s} \left( \frac{\lambda}{Le_i c_p} \frac{\partial Y_i}{\partial s} \right) = \dot{\omega}_i, \quad i = 1, \dots, N_s, \quad (2.24)$$

$$\frac{\partial(mh)}{\partial s} - \frac{\partial}{\partial s} \left( \frac{\lambda}{c_p} \frac{\partial h}{\partial s} \right) = \frac{\partial}{\partial s} \left( \frac{\lambda}{c_p} \sum_{i=1}^{N_s} \left( \frac{1}{Le_i} - 1 \right) h_i \frac{\partial Y_i}{\partial s} \right). \quad (2.25)$$

The balance equation (2.24) between convection, diffusion and reaction can be considered as a steady-state relation just like (1.40) and (1.49). Note that in the steady-state relations of conventional reduction techniques not only the multi-dimensional perturbations are neglected, but also the left-hand side of (2.24) describing the major parts of convection and diffusion.

The set of 1D equations (2.23)–(2.25) can be solved relatively easily with specialized 1D flame codes like CHEM1D [12]. A solution of this set of equations is called a flamelet and forms a curve in composition space, which can be regarded as a one-dimensional manifold.

## 2.2 Manifold construction

In this section it is described how the set of 1D equations (2.23)–(2.25) is used to create a manifold. As in the ILDM method a distinction is made between variables that are changed by chemical reactions (the species mass fractions  $Y_i$ ) and variables that are conserved by chemical reactions ( $Z_j$ ,  $p$  and  $h$ ). The composition of the chemical equilibrium mixture is completely determined by the values of the conserved variables, while the combustion process from the unburnt to burnt state is described by the reactive controlling variables, which are referred to as progress variables. Following Maas and Pope [54], we first consider the case of constant conserved variables. In section 2.2.3 it is discussed how variations in the conserved variables should be treated.

### 2.2.1 One-dimensional manifold

In order to construct a FGM, the set of 1D flamelet equations (2.23)–(2.25) is solved treating the system as an adiabatic, freely-propagating, premixed, flat flame. This implies that the boundary conditions at the unburnt side are of Dirichlet type

$$Y_i(s \rightarrow -\infty) = Y_{i,-\infty}, \quad h(s \rightarrow -\infty) = h_{-\infty}, \quad (2.26)$$

and at the burnt side of Neumann type

$$\frac{dY_i}{ds}(s \rightarrow \infty) = 0, \quad \frac{dh}{ds}(s \rightarrow \infty) = 0, \quad (2.27)$$

and that the mass burning rate  $m$  is an eigenvalue of the problem. The solution of this system is a 1D curve in composition space and is determined by its starting point  $(Y_{i,-\infty}, h_{-\infty})$ . The one-dimensional FGM in composition space is simply the flamelet starting at the point

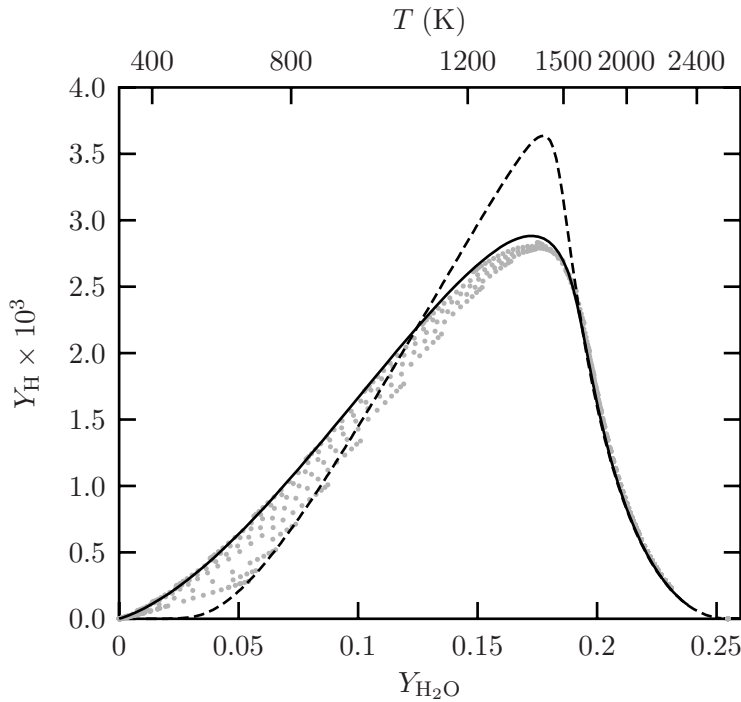


**Figure 2.3.** Projection of the 1D FGM (full line) and ILDM (dashed line) onto the  $\text{H}_2\text{O}$ – $\text{H}$  plane for a stoichiometric hydrogen/air mixture. The gray dots represent the chemical state at different positions in a 2D premixed hydrogen/air flame computed with detailed chemistry. The temperatures indicated at the top axis correspond to the FGM.

that represents the unburnt mixture for which the manifold is created. In this way the manifold connects the two most distinguished points in composition space: the point corresponding to the unburnt mixture  $(Y_{i,-\infty}, h_{-\infty}) = (Y_{i,u}, h_u)$  and the equilibrium point  $(Y_{i,\infty}, h_\infty) = (Y_{i,\text{eq}}, h_{\text{eq}})$ .

As an example the one-dimensional FGM and ILDM for a stoichiometric hydrogen/air mixture are shown in figure 2.3 together with a scatter plot of the chemical state at different positions in a 2D stationary premixed Bunsen flame computed with detailed chemical kinetics. The detailed reaction mechanism is a subset of the reaction mechanism listed in appendix A and includes 7 species and 7 reversible reactions. The mass fraction of atomic hydrogen  $Y_{\text{H}}$  is plotted as function of the mass fraction of water  $Y_{\text{H}_2\text{O}}$ , which is a suitable progress variable in this case, because it is continuously increasing in the flame from  $Y_{\text{H}_2\text{O},u} = 0$  in the unburnt mixture to the chemical equilibrium value  $Y_{\text{H}_2\text{O},\text{eq}} = 0.24$ . If  $Y_{\text{H}}$  had been used as controlling variable, it would not have led to a unique mapping.

Generally, Lewis-number (or differential diffusion) effects cause local enthalpy and element mass fraction variations in flames and thus also in the FGM database. In the ILDM method, however, the element composition and the enthalpy of the mixture are constant throughout the manifold and variations in the conserved variables can only be accounted for by using additional controlling variables. Therefore, to make a fair comparison of the methods in figure 2.3, Lewis numbers equal to 1 have been used in the computation of both the FGM and the 2D flame so that differential diffusion effects are absent in all three cases. An example of a FGM computed with Lewis numbers unequal to 1, is presented in section 2.2.3.

Because the composition is determined by chemical processes in the high temperature range ( $Y_{\text{H}_2\text{O}} > 0.19$ ,  $T > 1600$  K), the ILDM and FGM are there equivalent. However, in the 'colder' zone ( $Y_{\text{H}_2\text{O}} < 0.19$ ) diffusion processes disturb the balance between chemical production and consumption. Since the major parts of convection and diffusion are included in FGM, the FGM lies much closer to the data of the detailed chemistry computation than the ILDM. In order to get accurate results in this region, the ILDM should be extended with additional progress variables, which decreases the numerical efficiency of the method. For this simple hydrogen reaction mechanism two progress variable will probably be enough. For more complex fuels and mechanisms many more controlling variables are needed to create an accurate ILDM. The addition of extra dimensions to the ILDM in order to satisfy accuracy requirements is described by Schmidt *et al.* [77].

The 2D Bunsen flame plotted in figure 2.3 is stabilized on a cold burner rim and is therefore locally cooled. This results in lower H radical concentrations than for the adiabatic FGM. In section 2.2.3 it is explained how these non-adiabatic effects can be accounted for in FGM.

### 2.2.2 Multi-dimensional manifolds

Like in the ILDM method, the accuracy of the FGM method can be enhanced by increasing the dimension of the manifold. With each additional dimension an extra progress variable, as well as the corresponding differential equation, is introduced. In this way an extra degree of freedom is added to the reduced system, which results in a more accurate description of the full system. When the dimension of the manifold is increased, a larger part of the composition space is covered. The addition of dimensions can be continued until the manifold spans the complete composition space. In that case the full system is recovered.

A 2D FGM can be constructed from a set of flamelets starting at different points on a 1D curve in composition space with constant conserved variables. This set of 1D flamelets forms a 2D surface in composition space: the 2D FGM, which can be parametrized by  $N_{\text{pv}} = 2$  progress variables. This method to generate multi-dimensional manifolds has been introduced by Pope and Maas [71]. A unique choice of the starting curve — manifold generator in [71] — cannot be given, although it should include the unburnt mixture and must be chosen in such a way that the resulting manifold covers an as large as possible range of the progress variables. Following these arguments Pope and Maas proposed a specification of the starting curve based on the extreme values of major species [71]. For a methane/air system a sensible choice of the major species is:  $\text{CH}_4$ ,  $\text{O}_2$ ,  $\text{CO}$ ,  $\text{H}_2$ ,  $\text{CO}_2$ ,  $\text{H}_2\text{O}$  and  $\text{N}_2$ . A mixture of these major species is stable and does not react at room temperature ( $\dot{\omega}_i = 0$ ). The other (or minor) species are taken zero at the starting curve.

The exact choice of the starting curve determines the resulting manifold, but it may not be crucial. If we assume that two controlling variables are sufficient to represent the chemical composition in a premixed flame satisfactorily, then the flamelets will rapidly relax towards a 2D attracting manifold. Therefore, however the starting points are chosen, the resulting manifold will be close to the underlying manifold except near the starting curve itself, where chemistry is negligible anyhow. This is demonstrated in section 3.4.2, where two similar 2D manifolds are created by using different starting curves. This method to generate multi-dimensional manifolds can be extended to the general case of  $N_{\text{pv}}$  dimensions by choosing a  $(N_{\text{pv}} - 1)$ -dimensional starting 'plane'.

As an example a 2D FGM is computed for a stoichiometric methane/air mixture. The

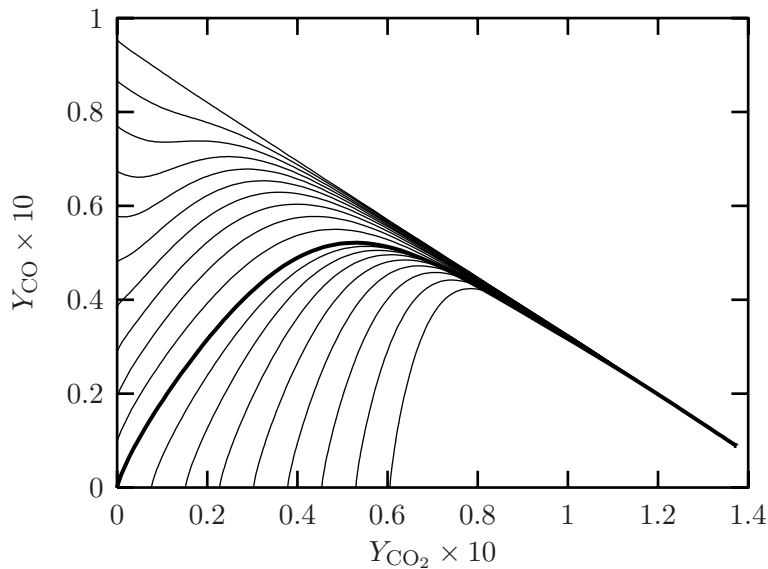


**Figure 2.4.** Projection of a two-dimensional FGM onto the  $\text{CO}_2$ – $\text{CO}$  plane for a stoichiometric methane/air mixture. The bold line denotes the one-dimensional manifold.

projection of this manifold on the  $\text{CO}_2$ – $\text{CO}$  plane is shown in figure 2.4. The origin of the plot corresponds to the unburnt mixture, which consists of  $\text{CH}_4$ ,  $\text{O}_2$  and  $\text{N}_2$  only, and it is connected with the equilibrium point by the 1D manifold. The projection of the starting curve coincides with the horizontal and vertical axis in figure 2.4. Along the horizontal axis  $\text{CO}_2$  and  $\text{H}_2\text{O}$  are added to the initial mixture, while along the vertical axis  $\text{CO}$  and  $\text{H}_2$  are added. Along the whole starting curve the enthalpy and the element mass fractions are kept constant by changing the values of  $Y_{\text{CH}_4}$ ,  $Y_{\text{O}_2}$  and  $T$ , which causes all flamelets to end up in the same chemical equilibrium. The different flamelets rapidly converge to a 1D manifold, which indicates that, apart from the conserved variables, one progress variable might be enough to describe the chemical state in that region.

For application in flame simulation codes, a manifold is parametrized by controlling variables. The species mass fractions or linear combinations of them can be used as controlling variables. In ILDM and FGM the selection of the controlling (or progress) variables is not related to fast or slow chemical processes as in the conventional reduction method. In fact any combination of species can be used as long as the parametrization of the manifold leads to a unique description of the mixture composition by the controlling variables. For the 1D manifold shown in figure 2.4 with a bold line,  $Y_{\text{CO}_2}$  is an appropriate controlling variable, while  $Y_{\text{CO}}$  would result in a non-unique mapping. On the other hand is  $Y_{\text{CO}}$  a suitable second controlling variable for the 2D manifold.

### 2.2.3 Conserved variables

In general, one or more of the conserved quantities  $p$ ,  $h$  and  $Z_j$  might vary in space or time due to other processes than chemical reaction, e.g. mixing and cooling/heating. If variations in a conserved variable are expected to be important in the application, then this variable should be added to the manifold as an additional controlling variable. In burner-stabilized flames, e.g., the enthalpy changes due to non-adiabatic effects resulting from flame stabilization. Furthermore, cooling due to radiation or walls may cause the enthalpy

to decrease. To account for these enthalpy changes, the FGM is extended with  $h$  being an additional parameter. The manifold is extended by solving the 1D flamelet equations (2.23)–(2.25) for different values of  $h_{-\infty}$ . Corresponding to the  $N_{pv}$ -dimensional manifold, we then obtain a  $(N_{pv} + 1)$ -dimensional manifold parametrized by  $N_{pv}$  progress variables and one additional controlling variable  $h$ .

Changes in the other conserved variables can be treated similarly, yielding a  $N_{cv}$ -dimensional manifold with  $N_{cv} = N_{pv} + N_{av}$  the total number of controlling variables and  $N_{av}$  the number of additional controlling variables.  $N_{av}$  has a maximum value of  $N_e + 1$ , i.e. the number of independent conserved variables. However, only a small number of additional controlling variables is needed for most applications, because in many cases several conserved variables can be assumed constant. In open systems, for instance, the pressure is constant and does not have to be used as an additional controlling variable.

In the remaining part of this chapter we discuss the application of FGM to laminar premixed burner-stabilized flames. Since these flames are purely premixed, the element mass fractions are constant apart from local changes due to differential diffusion effects, which are included in the manifold. Because the pressure is also constant in these flames, the enthalpy is the only conserved variable in which significant changes are expected ( $N_{av} = 1$ ). Since no large multi-dimensional perturbations are expected as well, one progress variable is used ( $N_{pv} = 1$ ), resulting in a 2D manifold. As explained in section 2.2.2 more progress variables can be used to increase the accuracy of the method. Since this implies that more differential equations have to be solved and the look-up procedure in the database becomes more complicated, the gain in computation time will decrease. Therefore, a small number of controlling variables is preferred.

## 2.3 Application of FGM

The application of FGM in flame simulations can be divided in two parts. The first part is the pre-processing step: the generation and storage of the flamelet data. This is explained in section 2.3.1. The second part, described in section 2.3.2, considers the equations to be solved during the flame computation itself.

### 2.3.1 Storage and retrieval

The implementation of FGM in a reacting-flow code is similar to the implementation of ILDM. The low-dimensional manifold is found by solving steady-state equations in a pre-processing step and the manifold is stored in a look-up table. In the FGM method a manifold is constructed by using solutions of the 1D flamelet equations (2.23)–(2.25).

To construct a 2D manifold with enthalpy variations, a series of flamelets is computed for different values of  $h_{-\infty}$  as mentioned in section 2.2.3. The first flamelet is solved for an initial mixture with a relatively high temperature, say  $T_{-\infty, \max} = 390$  K. For the following flamelets the enthalpy is decreased by lowering the temperature of the initial mixture in steps of approximately 30 K. The 1D flamelet equations are solved by using a modified Newton method, in which the previous flamelet is used as the initial guess of the new solution. Since the difference between two succeeding flamelet solutions is small, a few iterations are sufficient to reach a converged solution. When an initial temperature of about  $T_{-\infty, \min} = 240$  K is reached, another method to lower  $h_{-\infty}$  is applied, because lower tem-

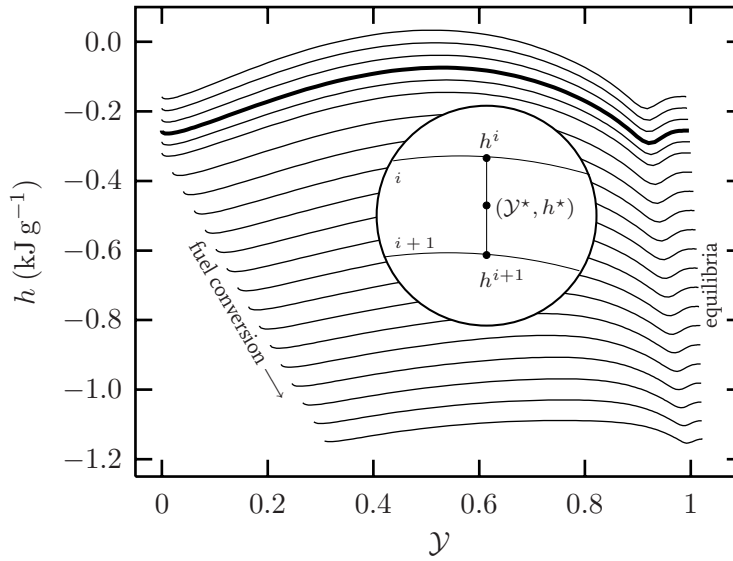


**Figure 2.5.** Projection of the two-dimensional FGM data set onto the  $\mathcal{Y}$ - $h$  plane for a stoichiometric methane/air mixture. The bold curve indicates the 1D manifold. In the circle a detail of the underlying flamelets is magnified.

peratures are not realistic. From hereon the enthalpy is decreased by converting a fraction of the initial fuel with oxygen into the products  $\text{CO}_2$  and  $\text{H}_2\text{O}$ , keeping the element composition constant and the initial temperature at  $T_{-\infty, \text{min}}$ . This process is continued until the flame temperature  $T_b$  becomes too low and the flame extinguishes.

This method to lower  $h_{-\infty}$  is not unique and the initial mixtures could be chosen otherwise. However, as argued in section 2.2.2 and demonstrated in section 3.4.2, the exact choice of the starting points is not crucial.

The resulting data set is shown in figure 2.5 for a stoichiometric methane/air mixture, where  $Y_{\text{O}_2}$  and  $h$  have been appointed as controlling variables. The mass fraction of oxygen is chosen as progress variable, because it is continuously decreasing in these flamelets. The progress variable is scaled using the initial and equilibrium value  $Y_{\text{O}_2, -\infty}$  and  $Y_{\text{O}_2, \text{eq}}$  of the 1D manifold ( $T_{-\infty} = 300 \text{ K}$ ):

$$\mathcal{Y} = \frac{Y_{\text{O}_2} - Y_{\text{O}_2, -\infty}}{Y_{\text{O}_2, \text{eq}} - Y_{\text{O}_2, -\infty}}. \quad (2.28)$$

Since at low enthalpy the mass fraction of  $\text{O}_2$  can be smaller than  $Y_{\text{O}_2, \text{eq}}$  at  $h = h_u$ , the value of  $\mathcal{Y}$  can be larger than 1 (see figure 2.5). Because enthalpy is conserved in the flamelet equations, the initial and equilibrium value of  $h$  are the same in each flamelet. However, due to differential diffusion effects the enthalpy changes locally in the flamelets. This also holds for the element mass fractions, which are governed by a similar equation as the enthalpy. Since these local variations are included in the manifold, additional controlling variables are not needed to model differential diffusion effects, while in ILDM these changes can only be accounted for by using additional controlling variables.

In literature several techniques to store manifold data have been proposed, ranging from artificial neural networks [15] and *in situ* adaptive tabulation [70] to orthogonal polynomials [90]. The most important criteria for judging these storage techniques are the memory required for the storage of the table, the CPU time required to retrieve a value,

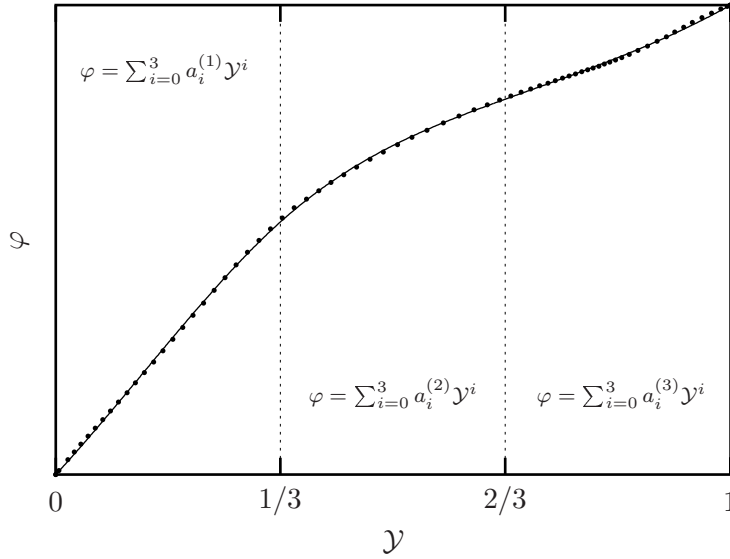


**Figure 2.6.** Piece-wise polynomial fit (line) to the data points (dots). In this example the  $\mathcal{Y}$  range is divided in 3 regions and in each region the data is fitted with a cubic polynomial.

and the accuracy of the retrieved value. In the following a method is explained which exploits the characteristics of the data set, resulting in a fast, accurate, and stable look-up procedure.

For each separate flamelet all dependent variables  $\varphi$ , that are needed in combustion simulations, and the enthalpy are stored as a function of the progress variable. To realize this, the  $\mathcal{Y}$  range is divided into equal-sized regions, and a cubic polynomial is fitted to the data points in each region (see figure 2.6). The resulting fit, consisting of the separate cubic polynomials, and its first derivative are forced to be continuous at the region boundaries. In order to predict the inlet and equilibrium composition accurately, the fit matches the data set exactly at both compositions. The accuracy of the fit can be improved by increasing the number of regions or the order of the polynomials.

To retrieve data from the manifold for given values of the controlling variables the following procedure is followed. First it is determined where the entry  $(\mathcal{Y}^*, h^*)$  is located. Therefore, the enthalpy is evaluated in two succeeding flamelets at  $\mathcal{Y} = \mathcal{Y}^*$ , yielding  $h^i$  and  $h^{i+1}$  for flamelets  $i$  and  $i + 1$  such that  $h^{i+1} < h^* < h^i$  (cf. figure 2.5). In the next step, intermediate values for the dependent variables are evaluated in both flamelets:  $\varphi^i$  and  $\varphi^{i+1}$ . The final value  $\varphi^*$  is obtained using a linear interpolation between these values:

$$\varphi^* = \frac{h^* - h^{i+1}}{h^i - h^{i+1}} \varphi^i + \frac{h^i - h^*}{h^i - h^{i+1}} \varphi^{i+1}. \quad (2.29)$$

Due to this linear interpolation as a function of  $h$ , the first derivative of  $\varphi$  with respect to  $h$  is discontinuous at the flamelets, which may be a problem in gradient-based solvers. This problem can be solved by using a higher-order interpolation. However, since the dependent variables change very smoothly in the direction of  $h$ , this imperfection has no consequences in our case.

One of the main advantages of this storage technique is that the boundaries of the tabulated domain are known very accurately. Therefore, effective measures can be taken if

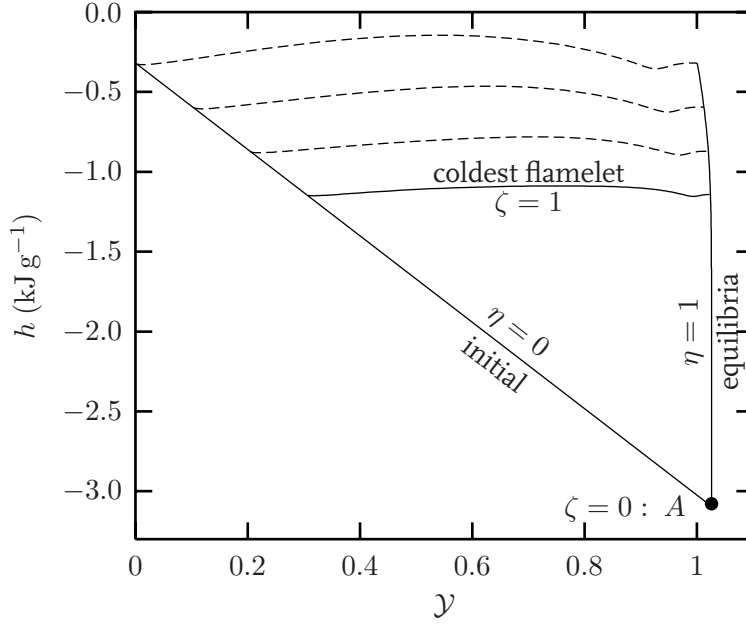


Figure 2.7. Interpolation in the low-enthalpy region.

an entry is outside this domain, resulting in a robust look-up method. Such a measure is needed, for instance, when burnt gases are cooled intensively, e.g. due to a local heat sink. The enthalpy of the mixture then drops below that of the 'coldest' flamelet, and the composition enters the so-called low-enthalpy region, shown in figure 2.7. Since no flamelet data is available there, the manifold must be continued into this region. A similar problem occurs in ILDM: at low temperatures the steady-state equations do not yield a solution and the manifold is continued into the cold region by linear extrapolation [55]. Recently, Gicquel *et al.* [29] proposed a method very similar to FGM called flame prolongation of ILDM (FPI) to tackle this problem. They prolonged the ILDM into the cold region by using the compositions in a 1D flame. Effectively, the 1D ILDM becomes exactly the same as the 1D FGM by using this prolongation technique. Application of FPI to multi-dimensional manifolds with two or more progress variables is not discussed in [29].

In FGM the manifold is prolonged into the low-enthalpy region as follows. First the low-enthalpy region is mapped onto the unit square  $(\eta, \zeta) = [0, 1] \times [0, 1]$  by using

$$\eta = \frac{\mathcal{Y} - \mathcal{Y}_{-\infty}}{\mathcal{Y}_{\text{eq}} - \mathcal{Y}_{-\infty}} \quad \text{and} \quad \zeta = \frac{h - h_{\text{min}}}{h^L - h_{\text{min}}}, \quad (2.30)$$

where  $h^L(\eta)$  is the enthalpy at the coldest flamelet and  $h_{\text{min}}$  the enthalpy of the chemical equilibrium with  $T = T_{\text{min}}$  (point A in figure 2.7). The profiles of the dependent variables along the coldest flamelet  $\varphi(\eta, 1)$ , the initial mixtures  $\varphi(0, \zeta)$  and the chemical equilibria  $\varphi(1, \zeta)$  are known. The values in the low-enthalpy region are approximated by interpolation using these profiles:

$$\varphi(\eta, \zeta) = \varphi(\eta, 0) + [\varphi(\eta, 1) - \varphi(\eta, 0)] [\eta f(\zeta) + (1 - \eta)g(\zeta)], \quad (2.31)$$

with

$$f(\zeta) = \frac{\varphi(1, \zeta) - \varphi(1, 0)}{\varphi(1, 1) - \varphi(1, 0)} \quad \text{and} \quad g(\zeta) = \frac{\varphi(0, \zeta) - \varphi(0, 0)}{\varphi(0, 1) - \varphi(0, 0)}. \quad (2.32)$$

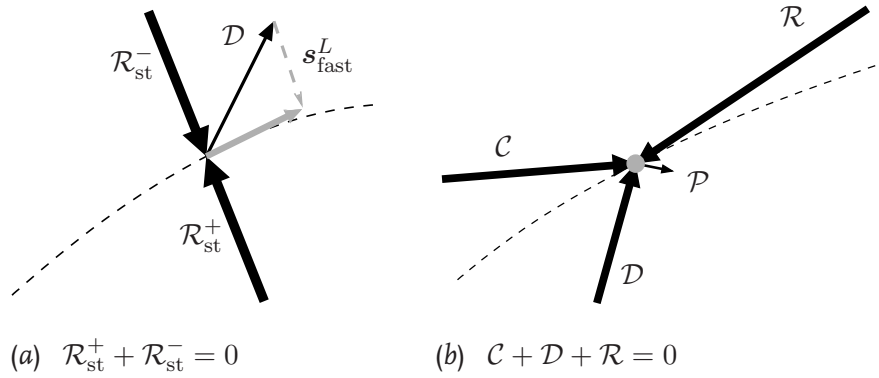


**Figure 2.8.** Projection of the different terms onto the manifold (dashed line) in the ILDM (a) and FGM (b) method. The different terms and their projections are represented by black and gray arrows, respectively.

When  $\varphi(1, 1) = \varphi(1, 0)$  or  $\varphi(0, 1) = \varphi(0, 0)$ , linear relations are used instead of (2.32), i.e.  $f(\zeta) = \zeta$  and  $g(\zeta) = \zeta$ . Since in most practical cases extensive cooling takes place in the burnt gases after the flame front, most entries in the low-enthalpy region are very close to chemical equilibria ( $\eta = 1$ ), where almost no interpolation error is made. Although this procedure to continue the manifold in the low-enthalpy region is rather 'ad-hoc' and might need some more attention, it appears to work quite well.

### 2.3.2 Reduced set of equations

After the FGM is stored in a database, it can be linked to a standard CFD code. This means that together with the momentum and continuity equations (1.22) and (1.23), the CFD code has to solve differential equations for the controlling variables. In ILDM these conservation equations for the controlling variables are derived by a projection of the full system onto the manifold. The different terms in the governing equations are projected using the left eigenvectors  $s_{fast}^L$  corresponding to the fast chemical processes [55]. Due to the definition of the ILDM the convection and the chemical source terms remain unchanged and only the diffusion term is affected by the projection. The projection of the diffusion term in ILDM is schematically shown in figure 2.8 (a), where it can be seen that the diffusion term  $\mathcal{D}$  is restricted to the manifold due to the balance between the large chemical production  $\mathcal{R}_{st}^+$  and consumption  $\mathcal{R}_{st}^-$  terms in the steady-state relation. Since the burning velocity of premixed laminar flames is determined by a balance between reaction and diffusion, an accurate projection of the diffusion terms is important. Although the eigenvector projection is mathematically the only correct one, other (simplified) projection techniques have been used successfully [25, 26, 30].

As shown in figure 2.8 (b), the steady-state relations in the FGM method are given by a balance between 1D convection  $\mathcal{C}$ , diffusion  $\mathcal{D}$  and reaction  $\mathcal{R}$ :  $\mathcal{C} + \mathcal{D} + \mathcal{R} = 0$ . The vector  $\mathcal{P}$  represents the multi-dimensional perturbations in (2.17), which are projected onto the manifold by the large terms  $\mathcal{C}$ ,  $\mathcal{D}$  and  $\mathcal{R}$ . The main difference with ILDM is that in FGM the steady-state relations (2.24) hold for all species, effectively 'freezing' the mixture composition. Therefore, the multi-dimensional perturbations are not only projected *onto* the manifold, but *in* the manifold as well. This results in  $\mathcal{P} = 0$ , which is of course related to the assumption that the multi-dimensional perturbations are neglected. If a flame is

extremely stretched or curved locally, the perturbations cannot be neglected and the dimension of the manifold should be increased, reducing the component of  $\mathcal{P}$  perpendicular to the manifold.

Since in the FGM method all species are assumed to be in a '1D steady state', a projection of the full set of equations onto the manifold does not result in differential equations for the controlling variables like in ILDM. Therefore, ordinary conservation equations for the controlling variables  $\mathcal{Y}$  and  $h$  are used in FGM. The differential equation for  $\mathcal{Y}$  reads

$$\frac{\partial(\rho\mathcal{Y})}{\partial t} + \nabla \cdot (\rho\mathbf{u}\mathcal{Y}) - \nabla \cdot \left( \frac{\lambda}{Le_{\mathcal{Y}}c_p} \nabla \mathcal{Y} \right) = \dot{\omega}_{\mathcal{Y}}, \quad (2.33)$$

which does include the multi-dimensional perturbation for the progress variable  $\mathcal{P}_{\mathcal{Y}}$ . Because the multi-dimensional perturbations depend on the choice of progress variable, the final result also depends on this choice. This is not the case in ILDM if the eigenvector projection is applied. However, if the multi-dimensional perturbations are small, the differences between results computed with different progress variables will be negligible.

The conservation equation for the enthalpy is given by

$$\frac{\partial(\rho h)}{\partial t} + \nabla \cdot (\rho\mathbf{u}h) - \nabla \cdot \left( \frac{\lambda}{c_p} \nabla h \right) = \nabla \cdot \mathcal{H}, \quad (2.34)$$

where  $\mathcal{H}$  represents the enthalpy flux due to differential diffusion:

$$\mathcal{H} = \frac{\lambda}{c_p} \sum_{i=1}^{N_s} \left( \frac{1}{Le_i} - 1 \right) h_i \nabla Y_i, \quad (2.35)$$

being a function of the species mass fraction gradients. Application of the chain rule yields

$$\mathcal{H} = \frac{\lambda}{c_p} \sum_{i=1}^{N_s} \left( \frac{1}{Le_i} - 1 \right) h_i \left( \frac{\partial Y_i}{\partial \mathcal{Y}} \nabla \mathcal{Y} + \frac{\partial Y_i}{\partial h} \nabla h \right), \quad (2.36)$$

stating that  $\mathcal{H}$  depends on the gradients of  $\mathcal{Y}$  and  $h$ . This may lead to unrealistic energy fluxes through inert walls, where  $\frac{\partial Y_i}{\partial n} = 0$  but  $\frac{\partial h}{\partial n} \neq 0$ . This problem is caused by the introduction of a manifold and is thus present in all manifold techniques. In FGM this problem can be circumvented by assuming that locally the enthalpy is given by the flamelet relation  $h = h^{1D}(\mathcal{Y})$ , which is a function of  $\mathcal{Y}$  only. This approximation is related to the assumption that locally no heat losses occur. Using this relation between  $h$  and  $\mathcal{Y}$ , the enthalpy flux  $\mathcal{H}$  can be written as a function of the gradient of  $\mathcal{Y}$  only:

$$\mathcal{H} = c \nabla \mathcal{Y}, \quad \text{with} \quad c = \frac{\lambda}{c_p} \sum_{i=1}^{N_s} \left( \frac{1}{Le_i} - 1 \right) h_i \left( \frac{\partial Y_i}{\partial \mathcal{Y}} + \frac{\partial Y_i}{\partial h} \frac{\partial h^{1D}}{\partial \mathcal{Y}} \right). \quad (2.37)$$

The coefficient  $c$  is stored in the FGM database together with the variables needed to solve the conservation equations, i.e.  $\rho$ ,  $\lambda$ ,  $c_p$ ,  $T$  and  $\omega_{\mathcal{Y}}$ . This is obviously much more efficient and accurate than storing the species mass fractions and computing these variables at runtime.

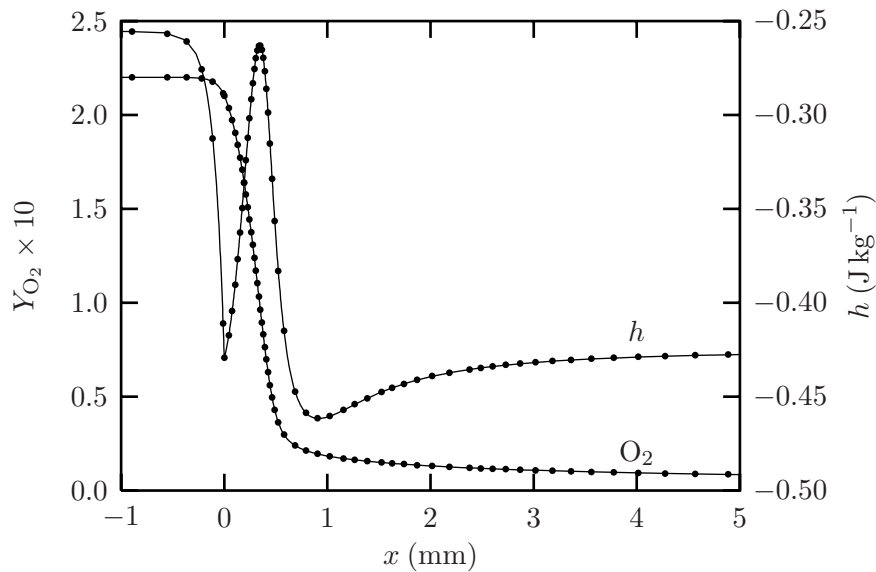


**Figure 2.9.** Profiles of the controlling variables  $Y_{O_2}$  and  $h$  in a one-dimensional burner-stabilized flame with  $m = 0.30 \text{ kg m}^{-2} \text{ s}^{-1}$ . Line: detailed chemistry; symbols: FGM. The symbols do not represent the computational grid; a much finer grid has been used in the calculations.

## 2.4 Test results

To demonstrate the performance of the FGM method, two test cases of premixed laminar methane/air flames have been simulated by using a 2D manifold as presented in the previous section. Results are shown for one and two-dimensional burner-stabilized flames, and they are compared with results obtained with the full kinetics mechanism, which consists of 16 species and 25 reversible reactions (appendix A).

### 2.4.1 One-dimensional validation

Apart from numerical inaccuracies, the most elementary premixed flame – the freely propagating flat flame – should be reproduced exactly by FGM. Burner-stabilized 1D flames, however, are subjected to non-adiabatic effects due to heat losses to the burner and are therefore more challenging. The burner outflow is positioned at  $x = 0$  and the burner area  $x < 0$  is kept at a constant temperature of  $T_{\text{burner}} = 300 \text{ K}$ . Stationary solutions are computed for different values of the mass burning rate  $m$  ranging from  $0.05$  to  $0.40 \text{ kg m}^{-2} \text{ s}^{-1}$ . The adiabatic mass burning rate of this stoichiometric methane/air flame is  $m = 0.421 \text{ kg m}^{-2} \text{ s}^{-1}$ , which corresponds to a laminar burning velocity of  $s_L = 0.375 \text{ m s}^{-1}$ . The flames are computed with the 1D flame solver CHEM1D [12] developed at the Eindhoven University of Technology. This code uses an exponential finite-volume discretization in space and the resulting system is solved using a fully implicit, modified Newton technique [86]. Adaptive gridding is implemented to increase the resolution around the flame front.

For  $m = 0.30 \text{ kg m}^{-2} \text{ s}^{-1}$  the profiles of the controlling variables  $Y_{O_2}$  and  $h$  are shown in figure 2.9. It can be seen that the results of the FGM method are in excellent agreement with those of the detailed reaction mechanism. Although the enthalpy is conserved in the flamelets that are used to construct the manifold, the enthalpy drop due to heat losses in the

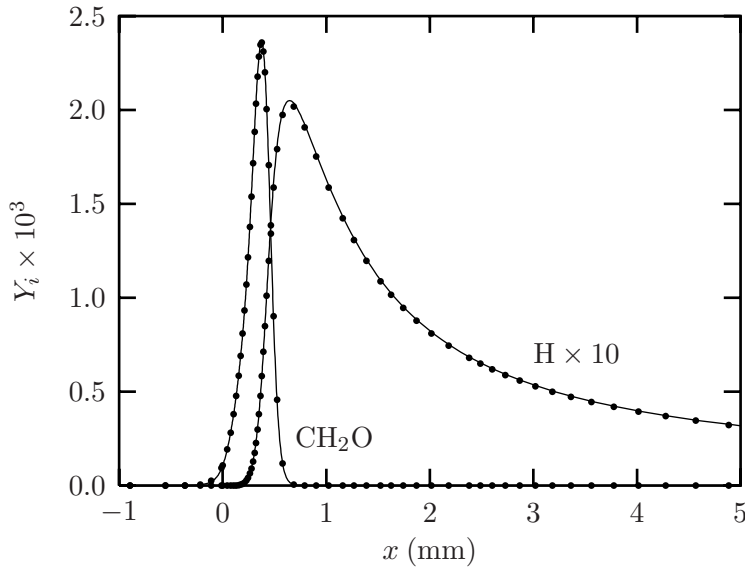


**Figure 2.10.** Profiles of the radicals  $Y_{\text{CH}_2\text{O}}$  and  $Y_{\text{H}}$  in a one-dimensional burner-stabilized flame with  $m = 0.30 \text{ kg m}^{-2} \text{ s}^{-1}$ . Line: detailed chemistry; symbols: FGM. The symbols do not represent the computational grid; a much finer grid is used in the calculations.

burner is modelled correctly with FGM. Beside these non-adiabatic effects in the burner, the large gradients in  $h$  in the flame front due to Lewis-number effects ( $0 < x < 1 \text{ mm}$ ) are reproduced very well. The mass fractions of  $\text{CH}_2\text{O}$  and  $\text{H}$  are displayed as function of  $x$  in figure 2.10. Even for these radicals, which are very difficult to reproduce accurately using ILDM, the resemblance between the FGM and detailed results is striking.

In figure 2.11 two global observables of 1D burner-stabilized flames are presented as function of the mass burning rate. These global observables are the non-adiabatic flame temperature  $T_{\text{b}}$  and the stand-off distance  $d$ , here defined as the position where the absolute value of the chemical source term  $|\dot{\omega}_{\text{O}_2}|$  reaches its maximum. The flame temperature is measured in the burnt mixture at  $x = 10 \text{ cm}$ , and is presented in the form of an Arrhenius plot. The differences in the flame temperature are smaller than 5 K and, therefore, almost invisible in the figure. Although the results for the stand-off distance are somewhat poorer, the deviation is within 1 percent of the flame thickness and therefore, also hardly visible in figure 2.11. Because at low mass burning rates the deviation from an adiabatic flamelet increases, the difference between the FGM and detailed computations increases as well.

## 2.4.2 Two-dimensional validation

The potential of the FGM method is demonstrated by a calculation of a 2D burner-stabilized laminar premixed flame. In this test case almost all the features found in premixed laminar flames — such as flame cooling, differential diffusion, stretch and curvature — are present. We have simulated a methane/air flame with an equivalence ratio of  $\phi = 0.9$  which stabilizes on a 2D slot burner in a box. The computational domain of the burner configuration is shown in figure 2.12. The burner slot is 6 mm wide, while the box is 24 mm wide. The burner and box walls are kept at a constant temperature of  $T_{\text{wall}} = 300 \text{ K}$ . The velocity profile at the inlet is parabolic with a maximum velocity of  $v_{\text{max}} = 1.0 \text{ m s}^{-1}$ .

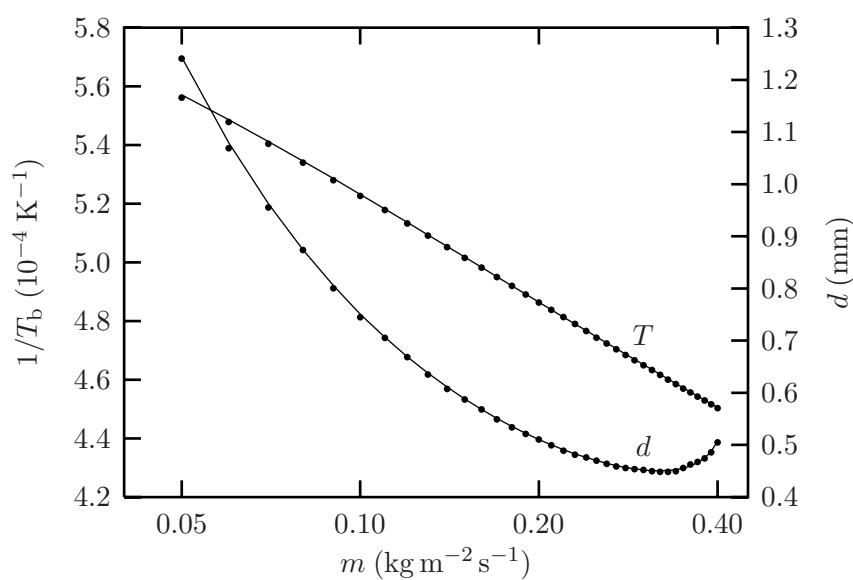


**Figure 2.11.** Arrhenius plot for the flame temperature  $T_b$  and the stand-off distance  $d$  as function of the mass burning rate  $m$  (log scale). Line: detailed chemistry; symbols: FGM.

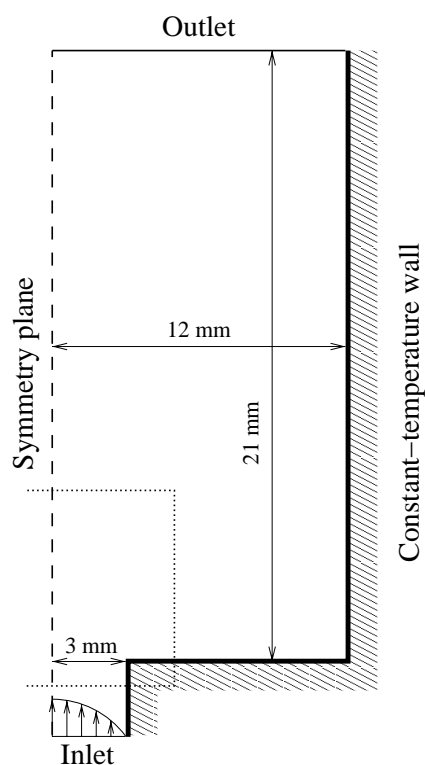


**Figure 2.12.** Numerical configuration used for the 2D computation. Results are shown for the region enclosed by the dotted line.

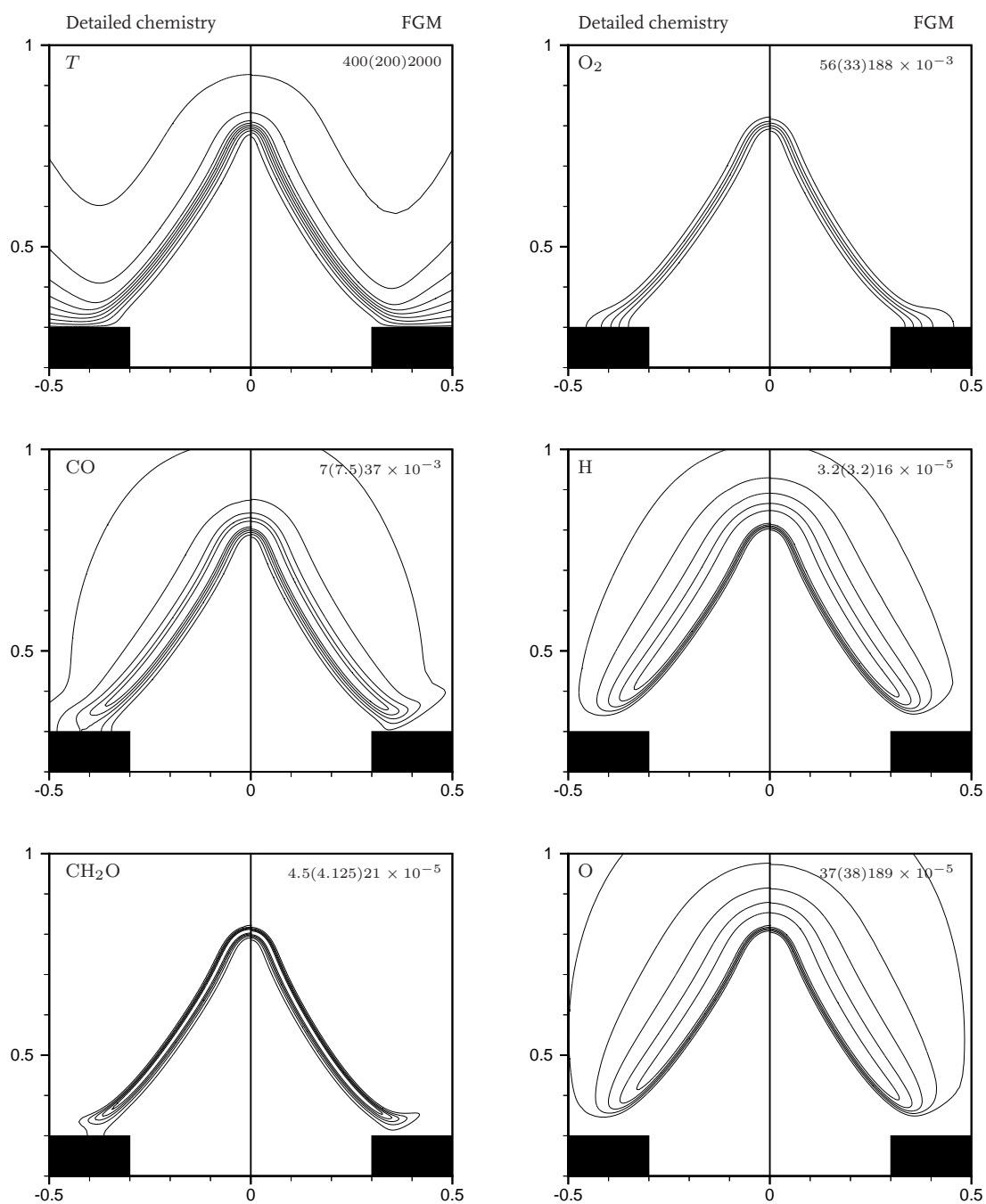


**Figure 2.13.** Isocontours of  $T$ ,  $Y_{O_2}$ ,  $Y_{CO}$ ,  $Y_H$ ,  $Y_{CH_2O}$  and  $Y_O$  computed using detailed chemistry (left) and FGM (right). The contours are drawn at equal intervals covering the entire range of each variable (indicated in the upper right corner of each graph). The same isolevels are used for detailed and FGM computations. The space coordinates are given in cm.

Isocontours of  $T$  and the mass fractions of  $O_2$ ,  $CO$ ,  $H$ ,  $CH_2O$  and  $O$  are shown in figure 2.13 on a portion of the computational domain for both the detailed and reduced chemistry computations. It can be seen that the results obtained with the FGM method are in excellent agreement with the detailed chemistry computations: not only the position of the flame front is predicted very well, but the absolute values of the mass fractions are reproduced as well. Flame cooling governing the stabilization of the flame on the burner is captured very well by FGM, although one can hardly speak of flamelets in this cold region. Also in the flame tip, where stretch and curvature are very important, the reduced chemistry computations appear to coincide with the detailed chemistry calculations. Close to the burner wall there are some differences in the  $Y_{CO}$  contours: the contours do not attach to the wall in the FGM case. Since  $Y_{CO}$  follows directly from the manifold database, which does not include diffusion along the flame front, the  $CO$  concentration is under-predicted by FGM in this diffusion-dominated area. To take this into account the manifold should be extended with a second progress variable.

The main difference between the detailed and reduced chemistry computations is the computation time. The computation with detailed chemistry took approximately two weeks to converge, while the FGM results were obtained within a few hours. These figures are only a rough indication of the gain in computation time, because different numerical solvers, grids and initial fields have been used. In the next section a more accurate study of the numerical efficiency of FGM is discussed.

### 2.4.3 Computational efficiency

Besides the accuracy, the efficiency is another important aspect of reduction methods. In order to give a further indication of the efficiency of FGM, the computation times of detailed and reduced chemistry simulations with ILDM and FGM are compared. For all models we determined the time needed to perform a time-dependent flame simulation at the same conditions. 1D burner-stabilized flames have been modelled for a period of  $10^{-3}$  s. At  $t = 0$  the mass flow rate has been reduced from 90% to 85% of the adiabatic mass burning rate. To solve the equations we have used the fully implicit solver CHEM1D [12] with adaptive time stepping. The FGM method has also been used with an explicit time stepper using constant time steps.

Two different mixtures are considered: a stoichiometric hydrogen/air and a stoichiometric methane/air mixture. The hydrogen reaction mechanism contains 7 species and is a subset of the methane reaction mechanism listed in appendix A. The manifolds used are 2D with one progress variable and the enthalpy as additional controlling variable. The same look-up procedure is used for both manifold methods. Lewis numbers equal to 1 are used in order to prevent variations in the element mass fractions. The computations are performed on a Silicon Graphics R10000 workstation and the results are shown in table 2.1.

For the hydrogen/air mixture the CPU time per time step  $t_{\text{step}}$  reduces a factor 2 when a manifold is applied. This speed up is caused by the reduction of the number of differential equations to be solved. For the detailed chemistry simulation of the methane/air mixture,  $t_{\text{step}}$  is 3 times larger than for the hydrogen/air mixture, because approximately 3 times as much differential equations and reaction rates have to be computed. For the reduced chemistry computations, however,  $t_{\text{step}}$  is independent of the number of species and reactions in the detailed reaction model. Therefore, the speed up is almost a factor 6 for the methane/air mixture. In this case the speed up is not only caused by a smaller number of equations to

**Table 2.1.** Results of time-dependent 1D flame simulations using different reaction models. The computation time per time step,  $t_{\text{step}}$ , the total simulation time,  $t_{\text{total}}$ , and the error (2.38) are shown.

Mixture	Chemistry model		$t_{\text{step}}$ (ms)	$t_{\text{total}}$ (s)	Error (%)
H <sub>2</sub> /air	Detailed	$N_s = 7, N_r = 7$	226	481	0
	ILDm	$N_{\text{pv}} = 1, N_{\text{av}} = 1$	110	63	8.63
	FGM	$N_{\text{pv}} = 1, N_{\text{av}} = 1$	112	62	0.08
CH <sub>4</sub> /air	Detailed	$N_s = 16, N_r = 25$	657	998	0
	ILDm	$N_{\text{pv}} = 1, N_{\text{av}} = 1$	–	–	–
	FGM	$N_{\text{pv}} = 1, N_{\text{av}} = 1$	110	46	0.05
	FGM explicit	$N_{\text{pv}} = 1, N_{\text{av}} = 1$	9	21	0.05

be solved, but by a faster evaluation of the chemical source terms as well. For the simple hydrogen mechanism with only 7 reactions, the direct computation of the chemical source term is as fast as the retrieval from the manifold database.

Another advantage of using reduced models is that larger time steps can be taken, because the smallest time scales have been eliminated. Therefore, the total CPU time  $t_{\text{total}}$  of the hydrogen/air computations using reduced chemistry is 8 times less than the detailed chemistry simulation. For the methane/air flame, the total speed up becomes a factor 20. An even higher efficiency is reached if an explicit time-integration scheme is used for the reduced chemistry computations. In that case the CPU time is reduced by almost a factor of 50 compared to the methane/air simulation using detailed chemistry. For more complex reaction mechanisms (GRI-mech:  $N_s = 49, N_r = 279$  [83]) and multi-dimensional systems the speed up will be even larger.

Since the same storage and retrieval method is used for the ILDM and FGM computations, the CPU times are almost the same. The results computed with the 2D FGM are, however, more accurate than the results computed with the 2D ILDM. To have an indication of the accuracy, the time evolution of the enthalpy  $h(0, t)$  at the burner edge is compared with results obtained with detailed chemistry. The error is defined as the absolute difference with the enthalpy  $h^{\text{det}}$  computed with detailed chemistry averaged over the total simulation period  $\Delta t$ , viz.

$$\text{Error} = \frac{1}{\Delta t \Delta h} \int_0^{\Delta t} |h(0, t) - h^{\text{det}}(0, t)| dt. \quad (2.38)$$

The error is scaled with the total variation in the enthalpy  $\Delta h = h^{\text{det}}(0, 0) - h^{\text{det}}(0, \Delta t)$ . For the hydrogen/air mixture the error in the ILDM computation is almost 9%. This error is mainly caused by the error in the adiabatic burning velocity, which is 8% too low in the ILDM case. The error of the FGM computations is smaller than 0.1% for both gas mixtures. For the methane/air mixture it is not possible to perform an ILDM computation, because an applicable 2D ILDM cannot be generated. Only in a small region around chemical equilibrium, enough chemical processes can be assumed in steady state. A 3D ILDM with two progress variables can be found for temperatures higher than 1200 K, but the accuracy is still too low and the mass burning rate is overestimated by a factor 2 [25].

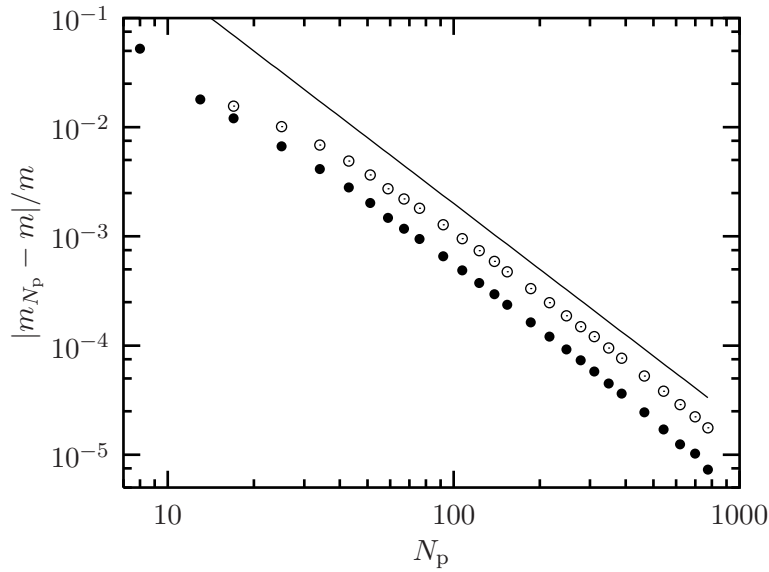


**Figure 2.14.** Relative error in the mass burning rate  $(m_{N_p} - m)/m$  as function of the number of grid points  $N_p$  in the flame front. Open symbols: detailed chemistry; filled symbols: FGM. The line indicates a slope of  $-2$ .

Three progress variables and the enthalpy would result in a 4D manifold. Besides that these high-dimensional manifolds require a large amount of memory and are less efficient than low-dimensional manifolds.

The computation of the 2D FGM databases used in these simulations involved approximately 30 minutes, which is quite long compared to the CPU times listed in table 2.1. Obviously, it is not efficient to construct a FGM for a single 1D flame simulation. However, the computation time that can be gained by using FGM in a series of multi-dimensional flame simulations is orders of magnitude larger than the time needed to construct the database.

Another important numerical aspect of flame simulations is the computational grid. Related to the wide range of time scales, there is also a large difference in length scales in premixed laminar flames. In order to resolve the thin reaction layer, where peaks in the different radical concentrations occur (cf. figure 2.10), many grid points with fine spacing are required to get an accurate representation of the solution. When FGM is applied, these small scales do not have to be resolved, because the flame is described by the relatively slowly varying progress variable. To demonstrate this, adiabatic 1D flames have been computed on grids with a different number of grid points. In figure 2.14 the relative error in the mass burning rate is plotted as function of the number of grid points  $N_p$  in the flame front. The relative error is defined as  $(m_{N_p} - m)/m$ , where  $m_{N_p}$  is the mass burning rate computed with  $N_p$  grid points in the flame front. The value of  $m$  is found by Richardson extrapolation.

The detailed chemistry and FGM results show the same behaviour: for large  $N_p$  the error decreases quadratically with the number of grid points, indicating that the space discretization is second order. At lower values of  $N_p$  the behaviour is only first order, which is typical for the discretization scheme of Thiart [89] used in the code. Because the smallest scales do not have to be resolved, the error of the FGM computations is approximately 50% smaller than detailed chemistry computations with the same number of grid points. In other words, when FGM is applied, 25 percent less grid points are required to reach the

same accuracy as in the detailed chemistry computations.

## 2.5 Conclusions

In this chapter the FGM method has been introduced and it has been used to compute burner-stabilized premixed laminar flames. Since a manifold is generated by using flamelets in FGM, it can be considered as a combination of a manifold and a flamelet approach. It combines the advantages of both approaches. FGM shares the basic idea with flamelet methods that a multi-dimensional flame can be regarded as a set of 1D flames. It is assumed that the structure of the flame front is similar in both types of flames and that the mixture composition is governed by a balance between 1D convection, diffusion and reaction. Since the main parts of convection and diffusion are included in the flamelet equations, the FGM is more accurate in regions where reaction is balanced by convection and diffusion than methods based on local chemical equilibria. In high-temperature regions, where chemistry is dominant, the flamelets are attracted by the ILDM and the ILDM and FGM are identical. Because FGM is more accurate in 'low'-temperature regions, less controlling variables are needed, which makes it an efficient reduction method. Test results of burner-stabilized methane/air flames show that only one progress variable apart from the enthalpy is sufficient to reproduce detailed chemistry simulations very well. A comparison with results obtained using a similar 2D ILDM is not possible, because for methane/air mixtures an ILDM with one progress variable can only be found in a small region around chemical equilibrium. This makes the application of this ILDM in flame simulations practically impossible. When two progress variables are used, a usable ILDM can be constructed. However, it overestimates the mass burning rate by a factor of two [25], which would probably result in flash-back for the 2D flame considered in this chapter, while the FGM with one progress variable predicts the correct position of the flame front.

The implementation of FGM in a flame simulation is typical for a manifold method. The reaction rates and other essential variables are stored in a database, which is used to solve the differential equations for the controlling variables. Because ordinary conservation equations are solved, the implementation in CFD codes is relatively easy compared with flamelet methods. In existing flamelet methods a kinematic equation for the scalar  $G$  is solved [64, 95]. In this so-called  $G$ -equation the burning velocity enters explicitly and the influence of flame stretch and curvature have to be modelled. Moreover, while the conservation equations for the controlling variables are valid throughout the complete domain, the  $G$ -equation is only valid at one value  $G = G^0$ , which denotes the position of the flame sheet. Everywhere else  $G$  is simply defined as the distance to the flame sheet ( $|\nabla G| = 1$ ), resulting in a flame of constant thickness. In FGM the flame thickness is in general not constant and, as the burning velocity, it follows from the conservation equations for the controlling variables. A disadvantage of solving conservation equations for the controlling variables, however, is that the flame front needs to be resolved. This requires a large number of grid points compared to flamelet methods which do not have to resolve the internal structure of the flame front.

An advantage of FGM is that the number of progress variables is not limited to one as in existing flamelet approaches. Although the test results show that one progress variable and the enthalpy are sufficient to reproduce detailed chemistry simulations very well, more progress variables can be added to increase the accuracy of the method. Addition

of progress variables might cause problems in the look-up procedure as described in section 2.3.1, because the different flamelets converge to form a lower-dimensional manifold (cf. figure 2.4). However, this problem can be solved by using a modified look-up technique. When the difference between the flamelets is too small (and the dimension of the manifold has actually decreases locally), the values are retrieved from the flamelet(s) in the lower-dimensional manifold.

A disadvantage of FGM compared to ILDM is that a general procedure to generate multi-dimensional manifolds cannot be derived. Since the researcher has to determine the starting points of the flamelets, the construction of a FGM cannot be automated to the same degree as that of an ILDM, where only the dimension of the manifold has to be prescribed by the researcher.

The test results presented in this chapter demonstrate the enormous potential of FGM. Results of computations with detailed chemistry have been reproduced very accurately within a fraction of the computation time. Since a FGM with one progress variable reaches the same accuracy for a methane/air flame as an ILDM with at least 3 dimensions, the dimension of the look-up database can be low. This not only reduces the computation time, but it also makes the numerical implementation relatively easy.

In the following chapters we investigate the effect of the multi-dimensional perturbations on the accuracy of the method. The influence of flame stretch is studied systematically in the next chapter. Deviations from purely premixed behaviour are examined in chapter 4.



# Flame Stretch

## 3.1 Introduction

FGM has been developed to model multi-dimensional premixed laminar flames efficiently. Flame stretch and curvature effects play an important role in multi-dimensional flames, because they can have a large influence on the mass burning rate. Since a FGM is constructed by using flat stretchless flamelets, these multi-dimensional effects are not included in the manifold. However, in this chapter we investigate whether flame stretch effects (possibly in combination with differential diffusion) can be taken into account using the FGM method. Moreover, it is investigated whether a FGM can be extended with extra controlling variables in order to reach a higher accuracy in stretched flame simulations.

In order to investigate the influence of flame stretch, steady premixed counterflow flames are modelled with both detailed reaction kinetics and FGM. These flames are very suitable to investigate flame stretch alone, because other effects such as flame curvature and unsteady effects are not present. Although a relatively simple configuration is studied in this chapter, it is believed that the results apply to stretch effects in 3D unsteady flames as well. Since the counterflow configuration provides a convenient tool for studying stretched flames, a number of experimental [76], analytical [79] and numerical [17, 84] studies have been reported on this configuration in literature.

The outline of this chapter is as follows. In the next section a relation between flame stretch and the mass burning rate is derived by using the Integral Analysis [16] following the basic ideas of De Goey and Ten Thijs Boonkkamp [33]. This relation is used in the analysis of the numerical results. Premixed counterflow flames are discussed in section 3.3. The governing equations are presented and relations for the variations in the element mass fractions and enthalpy are given. The results of the numerical computations are presented in section 3.4. Three different diffusion models are used in the simulations and their results are discussed in separate parts.

## 3.2 Mass burning rate of premixed flames

A key feature of premixed flames is the burning velocity or mass burning rate. The propagation and stabilization of a premixed flame is governed by a local balance between gas velocity and burning velocity (cf. the kinematic equation (2.4)). Therefore, a lot of effort is made to measure the mass burning rate of premixed flames. Not only for laminar flames, but for turbulent premixed flames as well (see e.g., [1, 52, 64]).

It is well known that flames stretch, caused for instance by local velocity gradients near the flame front, may have an important influence on the mass burning rate. First started

by Karlovitz *et al.* [41] and Markstein [57], many researchers have studied the influence of flame stretch since. In the following subsections a relation for the mass burning rate of both stretchless and stretched flames is derived.

### 3.2.1 Mass burning rate of stretchless flames

Before the effect of flame stretch is investigated, we first consider the mass burning rate of stretchless flames, i.e. for  $K = 0$ . Note that stretchless flames may still be curved, i.e.  $\kappa \neq 0$ . By using Integral Analysis [16] the mass burning rate  $m_b^0$  of a stretchless flame can be computed from the quasi-1D equation for  $\mathcal{Y}$ :

$$\mathcal{F}(s) - \frac{\partial}{\partial s} \mathcal{G}(s) = \mathcal{S}(s), \quad (3.1)$$

with  $\mathcal{F}$ ,  $\mathcal{G}$  and  $\mathcal{S}$  the convective, diffusive and reactive terms, respectively, which are defined by

$$\mathcal{F}(s) = \frac{\partial}{\partial s} (\sigma m \mathcal{Y}), \quad (3.2)$$

$$\mathcal{G}(s) = \sigma \frac{\lambda}{Le_{\mathcal{Y}} c_p} \frac{\partial \mathcal{Y}}{\partial s}, \quad (3.3)$$

$$\mathcal{S}(s) = \sigma \dot{\omega}_{\mathcal{Y}}. \quad (3.4)$$

We multiply (3.1) with  $\mathcal{G}$  and subsequently integrate the resulting equation over  $s$  from  $s_u$  to  $s_b$ . Because the diffusion fluxes are zero in the (un)burnt mixture, the integral over the diffusion term drops out and we find

$$\int_{s_u}^{s_b} \mathcal{F}(s) \mathcal{G}(s) ds = \int_{s_u}^{s_b} \mathcal{S}(s) \mathcal{G}(s) ds. \quad (3.5)$$

The term  $\mathcal{G}$  in the left-hand side of this equation can be obtained by integrating (3.1) over the preheat zone, where  $|\mathcal{S}| \ll |\mathcal{F}|$ . This yields the approximation

$$\mathcal{G}(s) = \int_{s_u}^s (\mathcal{F}(\eta) - \mathcal{S}(\eta)) d\eta \approx \int_{s_u}^s \mathcal{F}(\eta) d\eta, \quad (3.6)$$

which, inserted into the left-hand side of (3.5), leads to

$$\int_{s_u}^{s_b} \mathcal{F}(s) \left( \int_{s_u}^s \mathcal{F}(\eta) d\eta \right) ds = \frac{1}{2} \left( \int_{s_u}^{s_b} \mathcal{F}(s) ds \right)^2 \approx \int_{s_u}^{s_b} \mathcal{S}(s) \mathcal{G}(s) ds. \quad (3.7)$$

This approximation is justified if the reaction zone is much thinner than the preheat zone, so that the major contribution to the integral of  $\mathcal{F}\mathcal{G}$  in (3.5) stems from the preheat zone. Evaluation of the integrals in (3.7) yields

$$\int_{s_u}^{s_b} \mathcal{F}(s) ds = \sigma_b m_b^0, \quad (3.8)$$

$$\int_{s_u}^{s_b} \mathcal{S}(s) \mathcal{G}(s) ds = \int_0^1 \sigma^2 \frac{\lambda}{Le_{\mathcal{Y}} c_p} \dot{\omega}_{\mathcal{Y}} d\mathcal{Y}, \quad (3.9)$$

where we used  $\mathcal{Y}_u = 0$  and  $\mathcal{Y}_b = 1$ . Substitution of these expressions into (3.7) results in the following approximation for the mass burning rate of a stretchless flame:

$$m_b^o(h_b^o, Z_{jb}^o) \approx \left( 2 \int_0^1 \left( \frac{\sigma}{\sigma_b} \right)^2 \frac{\lambda}{Le_Y c_p} \dot{\omega}_Y d\mathcal{Y} \right)^{1/2}. \quad (3.10)$$

It should be realized that this is not equal to the adiabatic mass burning rate of a flat flame, due to the factor  $(\sigma/\sigma_b)^2$ . However, for a sufficiently thin reaction layer the curvature factor  $\sigma/\sigma_b \approx 1$  and the expression reduces to the adiabatic mass burning rate of a flat flame.

In (3.10) we explicitly emphasized the dependency of the mass burning rate on the enthalpy  $h_b^o$  and element composition  $Z_{jb}^o$  of the burnt mixture, because the integral in (3.10) effectively runs only over the thin reaction layer, in which  $\dot{\omega}_Y \neq 0$  and in which the system approaches the equilibrium state. If we assume that the chemical composition lies in a 1D manifold near the equilibrium state, then the term  $(\lambda \dot{\omega}_Y)/(Le_Y c_p)$ , which formally depends on all flame variables, can be written as function of  $\mathcal{Y}$  only. In this case the integral over  $\mathcal{Y}$  is independent of the initial composition and depends only on the equilibrium composition, which is completely described by the pressure (assumed to be constant), enthalpy and element composition in the burnt mixture, i.e.  $h_b^o$  and  $Z_{jb}^o$ .

### 3.2.2 Mass burning rate of stretched flames

The mass burning rate of stretched flames can be evaluated following the same procedure as in the previous section. The mass burning rate is again determined from (3.1), but now with  $\mathcal{F}(s)$  given by

$$\mathcal{F}(s) = \frac{\partial}{\partial s}(\sigma m \mathcal{Y}) + \sigma \rho K \mathcal{Y}, \quad (3.11)$$

while  $\mathcal{G}$  and  $\mathcal{S}$  are still given by (3.4). The integral of  $\mathcal{F}$  in (3.8) now becomes

$$\int_{s_u}^{s_b} \mathcal{F}(s) ds = \sigma_b m_b + \int_{s_u}^{s_b} \sigma \rho K \mathcal{Y} ds, \quad (3.12)$$

which yields the following expression for the mass burning rate

$$m_b(h_b, Z_{jb}) \approx \left( 2 \int_0^1 \left( \frac{\sigma}{\sigma_b} \right)^2 \frac{\lambda}{Le_Y c_p} \dot{\omega}_Y d\mathcal{Y} \right)^{1/2} - \frac{1}{\sigma_b} \int_{s_u}^{s_b} \sigma \rho K \mathcal{Y} ds. \quad (3.13)$$

Comparison of the first term on the right-hand side with (3.10) indicates that this term can be related to the mass burning rate of a stretchless flame  $m_b^o$  with enthalpy and element composition of the burnt mixture given by the 'stretched' variables  $h_b$  and  $Z_{jb}$  instead of their 'stretchless' counterparts  $h_b^o$  and  $Z_{jb}^o$ . Combining (3.10) with (3.13) then gives

$$m_b(h_b, Z_{jb}) \approx (1 - \mathcal{K}a) m_b^o(h_b, Z_{jb}), \quad (3.14)$$

where we have introduced the Karlovitz integral  $\mathcal{K}a$

$$\mathcal{K}a = \frac{1}{\sigma_b m_b^o} \int_{s_u}^{s_b} \sigma \rho K \mathcal{Y} ds, \quad (3.15)$$

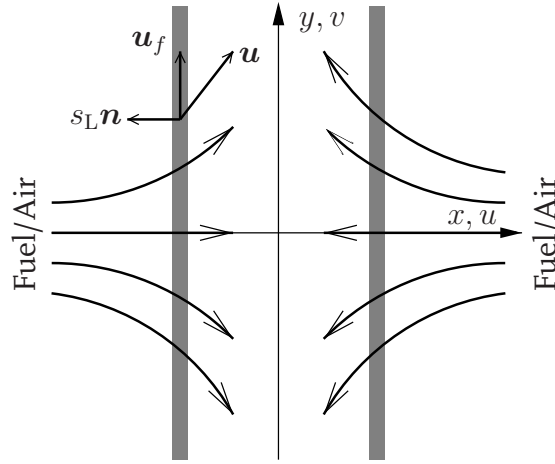


**Figure 3.1.** Schematic overview of the premixed counterflow configuration. The gray regions indicate the flame fronts. The curved lines indicate the flow direction.

which is a dimensionless number indicating the ratio between flame stretch and the mass burning rate. Theoretically, it can be shown that other choices for  $\mathcal{Y}$  give the same final result for  $m_b$ . Equation (3.14) is used in the analysis of the numerical results in section 3.4.

### 3.3 Premixed counterflow flames

To investigate the influence of flame stretch on the accuracy of FGM, premixed flames in a planar stagnation flow are modelled. A schematic overview of the so-called unburnt-to-unburnt or back-to-back configuration is shown in figure 3.1. Two identical premixed fuel/air jets impinge on each other forming a stagnation plane with on both sides a flat premixed laminar flame.

Since these flames are considered to be flat and steady, the combustion variables  $\rho$ ,  $T$ ,  $h$  and  $Y_i$  only depend on the coordinate  $x$  perpendicular to the flame surfaces. The  $y$ -component  $v$  of the flow velocity and the pressure are functions of both space coordinates  $x$  and  $y$ . Since the flame is stationary, the velocity of the flame surfaces is given by  $\mathbf{u}_f = v\mathbf{e}_y$ , with  $\mathbf{e}_y$  the unit vector in  $y$ -direction, and the burning velocity  $s_L$  equals the  $x$ -component  $u$  of the flow velocity. Using  $\mathbf{u}_f = v\mathbf{e}_y$  in (2.7) results in the following expression for the local stretch rate:

$$K = \frac{\partial v}{\partial y}. \quad (3.16)$$

Using this expression in the continuity equation yields

$$\frac{\partial(\rho u)}{\partial x} = -\rho K. \quad (3.17)$$

Since the combustion variables only depend on  $x$ , the burning velocity  $s_L$  and thus  $u$  only depend on  $x$  as well. Therefore, differentiation of (3.17) with respect to  $y$  gives us that  $K$  is a function of  $x$  only.

Combining (3.16) with the conservation equations for mass (1.22), species (1.25) and enthalpy (1.24), we obtain a set of 1D equations:

$$\frac{dm}{dx} = -\rho K, \quad (3.18)$$

$$\frac{d(mY_i)}{dx} - \frac{d}{dx} \left( \frac{\lambda}{Le_i c_p} \frac{dY_i}{dx} \right) - \dot{\omega}_i = -\rho K Y_i, \quad (3.19)$$

$$\frac{d(mh)}{dx} - \frac{d}{dx} \left( \frac{\lambda}{c_p} \frac{dh}{dx} \right) = \frac{d}{dx} \left( \frac{\lambda}{c_p} \sum_i^{N_s} h_i \left( \frac{1}{Le_i} - 1 \right) \frac{dY_i}{dx} \right) - \rho K h, \quad (3.20)$$

where  $m = \rho u$ . Realizing that  $\partial x = \partial s$  and  $u = s_L$ , we see that this set of 1D equations is equal to the flamelet equations (2.16)–(2.18) without curvature ( $\kappa = 0$ ,  $\sigma = 1$ ) and  $Q$ -terms. Therefore, flame stretch is the only multi-dimensional perturbation involved in these premixed counterflow flames.

The stretch field  $K$  is yet unknown, but Dixon-Lewis has shown in [19] that a differential equation for  $K$  can be derived from the momentum equations (1.23). Using (3.16) and (3.18), the  $x$ -momentum equation can be reduced to

$$\frac{\partial p}{\partial x} = -m \frac{du}{dx} + \frac{d}{dx} \left[ \frac{2}{3} \mu \left( 2 \frac{du}{dx} - K \right) \right] + \mu \frac{dK}{dx}. \quad (3.21)$$

In a similar way, the  $y$ -momentum equation can be simplified to

$$m \frac{dK}{dx} + \rho K^2 - \frac{d}{dx} \left( \mu \frac{dK}{dx} \right) = -\frac{1}{y} \frac{\partial p}{\partial y}. \quad (3.22)$$

Since the right-hand side of (3.21) only depends on  $x$ , it is clear that the pressure derivative  $\partial p / \partial x$  is a function of  $x$  only. Differentiation of (3.21) with respect to  $y$  and changing the order of differentiation then gives that  $\partial p / \partial y$  is a function of  $y$  only. Combining this result with (3.22), it can be concluded that the right-hand side of (3.22) is a constant, i.e.

$$J = -\frac{1}{y} \frac{\partial p}{\partial y}, \quad (3.23)$$

which denotes the pressure curvature in  $y$ -direction. The  $y$ -momentum equation (3.22) then yields the following differential equation for  $K$ :

$$m \frac{dK}{dx} - \frac{d}{dx} \left( \mu \frac{dK}{dx} \right) = J - \rho K^2. \quad (3.24)$$

In the unburnt mixture, where  $\rho = \rho_u$ , the flow is assumed to behave as a potential flow with a constant velocity gradient  $a$ , i.e.

$$\frac{\partial u}{\partial x} = -a \quad \text{and} \quad K = \frac{\partial v}{\partial y} = a. \quad (3.25)$$

In order to have  $K(x \rightarrow -\infty) = a$  in the unburnt mixture, the right-hand side of (3.24) must be zero there. Therefore, the constant  $J$  is related to the velocity gradient  $a$  as follows

$$J = \rho_u a^2. \quad (3.26)$$

The velocity gradient  $a$  is often referred to as the applied strain. For weak stretch, when  $K \rightarrow 0$  and  $a \rightarrow 0$ , the right-hand side of (3.24) can be neglected as well and the local

stretch rate is constant:  $K(x) = a$ . Note that the differential equation (3.24) for  $K$  is derived for this special case only. In general, the stretch field cannot be found from a differential equation, but it should follow from its definition (2.7).

Since the premixed counterflow problem is symmetric, only the left side of figure 3.1 with  $x \leq 0$  and  $u \geq 0$  is considered. Moreover, the stagnation plane at  $x = 0$  is treated as symmetry plane. Together with the potential flow in the unburnt mixture at  $x = -\infty$  this yields the following boundary conditions:

$$m(0) = 0, \quad (3.27)$$

$$\frac{dK}{dx}(0) = 0, \quad K(-\infty) = a, \quad (3.28)$$

$$\frac{dY_i}{dx}(0) = 0, \quad Y_i(-\infty) = Y_{iu}, \quad i = 1, \dots, N_s, \quad (3.29)$$

$$\frac{dh}{dx}(0) = 0, \quad h(-\infty) = h_u. \quad (3.30)$$

Conservation equations for the  $N_e$  element mass fractions  $Z_j$  can be derived by taking the proper linear combinations of (3.19):

$$\frac{d(mZ_j)}{dx} - \frac{d}{dx} \left( \frac{\lambda}{c_p} \frac{dZ_j}{dx} \right) = \frac{d}{dx} \left( \frac{\lambda}{c_p} \sum_i^{N_s} w_{ji} \left( \frac{1}{Le_i} - 1 \right) \frac{dY_i}{dx} \right) - \rho K Z_j, \quad (3.31)$$

where the first term at the right-hand side is due to differential diffusion. Note the resemblance between equation (3.31) and the conservation equation for the enthalpy (3.20). When unity Lewis numbers are applied for all species, the differential diffusion term drops out and the enthalpy and the element mass fractions are constant and conserved, i.e.  $Z_j = Z_{ju}$  and  $h = h_u$ . Furthermore, if the Lewis numbers of species that include element  $j$  are equal ( $Le_i = Le_j$  if  $w_{ji} \neq 0$ ), the differential diffusion flux for this element reads

$$\frac{\lambda}{c_p} \sum_i^{N_s} w_{ji} \left( \frac{1}{Le_i} - 1 \right) \frac{dY_i}{dx} = \frac{\lambda}{c_p} \left( \frac{1}{Le_j} - 1 \right) \frac{dZ_j}{dx}. \quad (3.32)$$

Using this result and (3.18) in (3.31) yields the following differential equation for the mass fraction of element  $j$ :

$$m \frac{dZ_j}{dx} - \frac{d}{dx} \left( \frac{1}{Le_j} \frac{\lambda}{c_p} \frac{dZ_j}{dx} \right) = 0, \quad (3.33)$$

effectively stating that the mass fraction of element  $j$  is constant, i.e.  $Z_j = Z_{ju}$ .

In general, however, the element mass fractions and enthalpy are changing in stretched flames. Integrating (3.31) from unburnt ( $x = -\infty$ ) to burnt ( $x = x_b$ ) yields

$$Z_{jb} - Z_{ju} = - \frac{1}{m_b} \int_{-\infty}^{x_b} \rho K (Z_j - Z_{ju}) dx + \frac{\mathcal{G}_{jb}}{m_b}, \quad (3.34)$$

where  $\mathcal{G}_{jb}$  is the diffusive flux of element  $j$  at  $x = x_b$ . Subtracting the unstretched case

$$Z_{jb}^o - Z_{ju} = \frac{\mathcal{G}_{jb}^o}{m_b^o}, \quad (3.35)$$

from (3.34) gives us a relation for the variations in the element mass fractions in the burnt mixture  $\Delta Z_{jb} = Z_{jb} - Z_{jb}^o$ , due to a combination of flame stretch and differential diffusion:

$$\Delta Z_{jb} = -\frac{1}{m_b} \int_{-\infty}^{x_b} \rho K (Z_j - Z_{ju}) dx + \frac{\mathcal{G}_{jb}}{m_b} - \frac{\mathcal{G}_{jb}^o}{m_b^o}. \quad (3.36)$$

If  $x_b$  is taken far enough from the reaction layer in the burnt mixture, then the diffusive fluxes  $\mathcal{G}_{jb}$  at this point can be neglected. This yields the following expression for the variation in the element mass fractions [33]:

$$\Delta Z_{jb} = -\frac{1}{m_b} \int_{-\infty}^{x_b} \rho K (Z_j - Z_{ju}) dx. \quad (3.37)$$

A similar expression can be derived for the enthalpy variation:

$$\Delta h_b = -\frac{1}{m_b} \int_{-\infty}^{x_b} \rho K (h - h_u) dx. \quad (3.38)$$

For weak stretch, the stretch rate may be assumed constant  $K = a$ , and the other variables may be replaced by their stretchless values. This leads to a linear relation between the variations and the applied strain  $a$ :

$$\Delta Z_{jb} \approx c_j a, \quad \text{with} \quad c_j = -\frac{1}{m_b^o} \int_{-\infty}^{x_b} \rho^o (Z_j^o - Z_{ju}) dx, \quad (3.39)$$

and

$$\Delta h_b \approx c_h a, \quad \text{with} \quad c_h = -\frac{1}{m_b^o} \int_{-\infty}^{x_b} \rho^o (h^o - h_u) dx. \quad (3.40)$$

Equations (3.39) and (3.40) imply that the variations in element mass fractions and enthalpy are coupled in the case of weak stretch. This result can be used in the construction of a manifold. Since the variations are not independent, only one additional controlling variable is needed to account for the changes in  $Z_{jb}$  and  $h_b$ . At higher stretch rates the coupling is distorted and the different elements and enthalpy should be treated more independently.

As explained in section 3.2 the enthalpy  $h_b$  and element composition  $Z_{jb}$  of the burnt mixture influence the mass burning rate  $m_b$ . Because an accurate representation of  $m_b$  is essential for premixed flame models, variations in  $h_b$  and  $Z_{jb}$  should be taken into account.

## 3.4 Numerical simulations

In this section the results of the numerical computations are presented. The set of governing equations (3.18–3.20, 3.24) is solved using the fully implicit 1D flame solver CHEM1D developed at the Eindhoven University of Technology [12]. The conservation equation for

$N_2$  is replaced by  $\sum Y_i = 1$  to ensure mass conservation. For all computations presented in this chapter, the unburnt gas is a stoichiometric methane/air mixture at 300 K and atmospheric pressure. The diffusive transport of species is modelled by using constant Lewis numbers. Three different cases are considered in this chapter:

1. Unity Lewis numbers are assumed for all species ( $Le_i = 1$ ). The unity Lewis number assumption is often used in theoretical research and in turbulent flame modelling. The element mass fractions and the enthalpy are constant and conserved in this case. Therefore, additional controlling variables to account for changes in  $Z_j$  and  $h$  are not needed here.
2. All Lewis numbers are equal to 1.1 ( $Le_i = 1.1$ ). According to (3.33) all element mass fractions are constant in this case, but the enthalpy is not. Variations in the enthalpy can be taken into account by adding an additional controlling variable ( $h$ ) to the manifold. For this case we investigate how the implementation of the additional controlling variable in the manifold influences the final result.
3. All Lewis numbers are constant but not the same ( $Le_i = const$ ). This is the most realistic model used in this chapter. Since differential diffusion effects are present in this case, variations in both enthalpy and element mass fractions occur.

In the following subsections the results for these three cases are presented.

The computations are performed with FGM and with the full reaction mechanism listed in appendix A. In this chapter a linear combination of species is chosen as progress variable  $\mathcal{Y}$ . In [33] De Goey and Ten Thijs Boonkkamp used the mass fraction of methane as progress variable. However, from a numerical point of view,  $Y_{CH_4}$  is not suitable as progress variable in the FGM method, although it is continuously decreasing in a premixed methane/air flame. Since methane is completely converted in the first part of the flame, it cannot be used to parameterize the variations in the mixture composition in the final stage of a premixed flame. The mass fraction of oxygen has a similar problem: it cannot describe the composition changes at the unburnt side accurately enough. Since  $H_2$  diffuses the most upstream in the preheat zone, it is used in the progress variable:

$$\mathcal{Y} = \frac{Y_{H_2}/M_{H_2} + Y_{H_2O}/M_{H_2O} + Y_{CO_2}/M_{CO_2}}{Y_{H_2\text{ eq}}/M_{H_2} + Y_{H_2O\text{ eq}}/M_{H_2O} + Y_{CO_2\text{ eq}}/M_{CO_2}}. \quad (3.41)$$

The mass fraction of  $CO_2$  and  $H_2O$  are included to ensure that  $\mathcal{Y}$  is continuously increasing. The progress variable is scaled by using the equilibrium values  $Y_{i\text{ eq}}$  for unchanged enthalpy and element mass fractions, i.e.  $h_{\text{eq}} = h_u$  and  $Z_{j\text{ eq}} = Z_{j\text{ u}}$ . The progress variable runs from zero in the unburnt to one in the burnt mixture.

### 3.4.1 Results for $Le_i = 1$

Before the results computed with FGM are shown, the computations using the full chemical reaction scheme are considered. Steady solutions are computed for strain rates varying from  $a = 30$  to  $3037\text{ s}^{-1}$ . At higher strain rates the flame extinguishes.

Profiles of  $Y_{O_2}$ ,  $Y_{CO}$  and  $K$  are shown in figure 3.2 for a relatively low and high strain rate:  $a = 100$  and  $2000\text{ s}^{-1}$ , respectively. Since the problem is symmetric, only the part at the left of the stagnation plane corresponding to negative  $x$  values is shown. In the

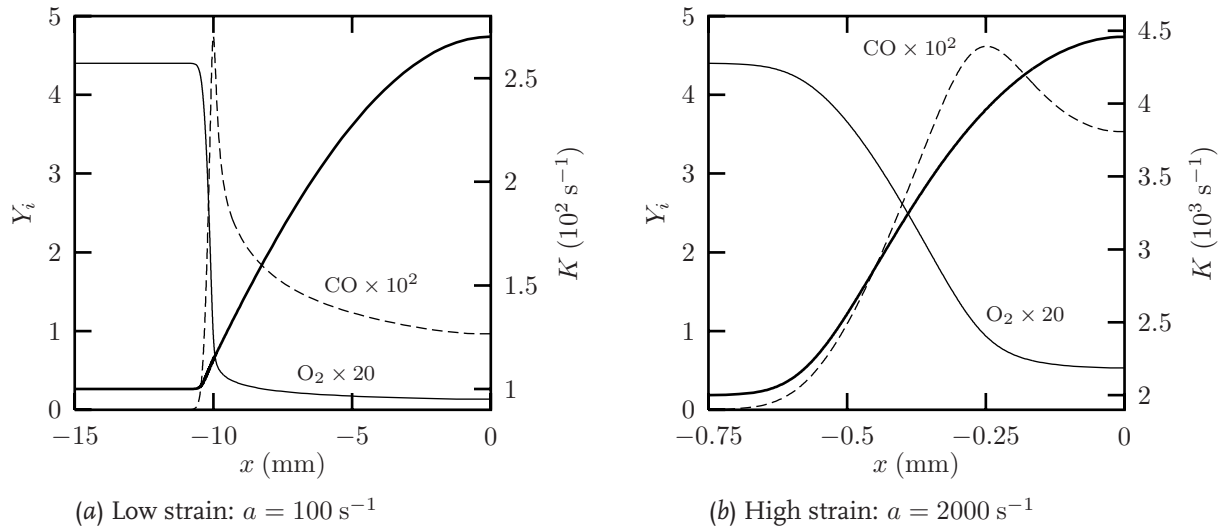


**Figure 3.2.** Profiles of  $Y_{\text{O}_2}$  (full),  $Y_{\text{CO}}$  (dashed), and the local stretch rate  $K$  (bold) in a counterflow flame for a low (a) and high (b) applied strain rate. Note the different scale of the  $x$ -axis in both plots.

unburnt mixture the local stretch rate is equal to the applied strain rate:  $K = a$ . After the flame front the stretch rate increases and finally reaches a maximum at the stagnation plane:  $K(0) = 270$  and  $4458 \text{ s}^{-1}$  for  $a = 100$  and  $2000 \text{ s}^{-1}$ , respectively. An expression for the stretch rate at the stagnation plane can be found by substitution of the boundary conditions at  $x = 0$  in equation (3.24):

$$K(0) \approx a \sqrt{\rho_u / \rho_{\text{eq}}}, \quad (3.42)$$

where the density  $\rho(0)$  at the stagnation plane is approximated by the equilibrium value  $\rho_{\text{eq}}$ . For the low strain rate the theoretical value  $K(0) = 274 \text{ s}^{-1}$  agrees well with the numerical value. For the high strain rate the theoretical value  $K(0) = 5475 \text{ s}^{-1}$  is too high, because in this case the mixture is not burnt completely and therefore, the density at the stagnation plane is higher than  $\rho_{\text{eq}}$ .

The main difference between the results in figure 3.2 (a) and (b) is not only that the stretch rate is higher in (b), but also that the flame is located much closer to the stagnation plane. For  $a = 100 \text{ s}^{-1}$  the flame stabilizes at  $x = -10 \text{ mm}$ , while at  $a = 2000 \text{ s}^{-1}$  the complete flame structure is within 1 mm of the stagnation plane. The applied strain also compresses the flame, resulting in a smaller flame thickness. This is not visible in figure 3.2, because the scales of the  $x$ -axes differ in (a) and (b). In order to make a comparison between the flame structures for different strain rates possible, the mass fraction of  $\text{O}_2$  and  $\text{CO}$  are translated and plotted as a function of  $x - x_b$  in figure 3.3. We have chosen the point  $x_b$  in the flue gases where the source term of the progress variable  $\dot{\omega}_y$  has been decreased by a factor of 10 from its maximum value. The profiles of  $Y_{\text{O}_2}$  clearly show that the flame is compressed by the applied strain. Besides this compression, an additional effect due to the applied strain can be observed in the  $Y_{\text{CO}}$  profiles. Since the flame is compressed by the applied strain, the gradients in the flame front become larger, which results in an enhanced diffusive transport. This enhanced diffusion results on its turn in a decrease of the maximum concentration of species related to slow chemical time scales. Therefore, the maximum concentration of  $\text{CO}$  decreases in figure 3.3 with increasing strain rate. These

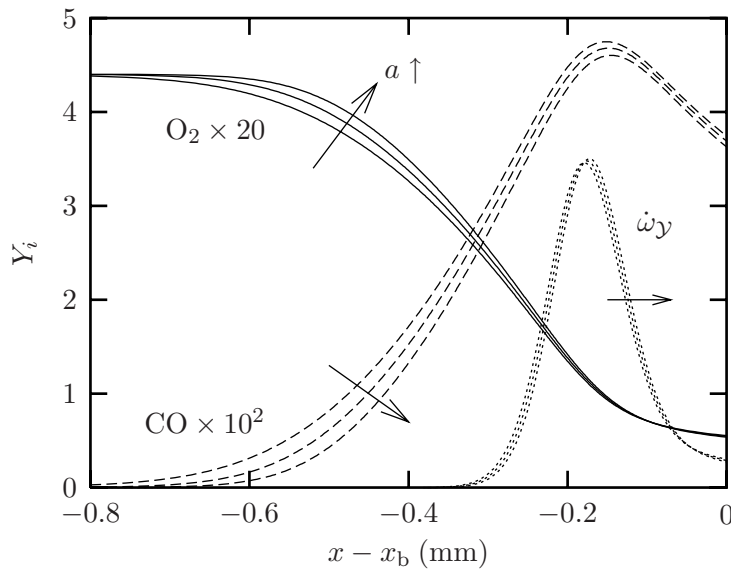


**Figure 3.3.** Mass fraction of  $O_2$  and  $CO$  as function of  $x - x_b$  in a counterflow flame with  $a = 30, 500$  and  $1000 \text{ s}^{-1}$ . The arrows indicate increasing strain rate. Full line:  $Y_{O_2}$ ; dashed line:  $Y_{CO}$ ; dotted line:  $\dot{\omega}_\gamma$ .

composition changes, however, have a negligible effect on the chemical source term of the progress variable  $\dot{\omega}_\gamma$ , as can be seen in figure 3.3. The shape of the curve does not change, but it is shifted a little towards  $x = x_b$ .

That the internal structure of the reaction layer is hardly changed by flame stretch, can also be seen in figure 3.4 (a), where a few solutions for different strain rates are plotted in composition space. The curves for the different strain rates follow almost the same path in the  $(\mathcal{Y}, Y_{CO})$ -plane. Note again that the small decrease of the maximum  $CO$  concentration due to the applied strain has a negligible effect on  $\dot{\omega}_\gamma$ .

The results shown in figure 3.4 (a) already indicate that a 1D FGM constructed using only one stretchless flamelet could give reasonably good results for these counterflow flames, because the correlation between the different species hardly changes. However, we want to study whether the accuracy of the method can be enhanced when the manifold is extended to two dimensions. Therefore, a 2D FGM is constructed, which captures the small decrease of the  $CO$  peak. This 2D manifold is constructed using stretchless flamelets which are computed for different initial compositions, but with the same enthalpy and element composition. The composition of the unburnt gases is changed by converting a part of the initial  $CH_4$  and  $O_2$  into  $CO_2$  and  $H_2O$ . The enthalpy of the initial mixture is kept constant by changing the temperature  $T_{-\infty}$ . A projection of this manifold on the  $(\mathcal{Y}, Y_{CO})$ -plane is shown in figure 3.4 (b). The flamelet with the lowest  $CO$  peak concentration corresponds to a conversion of 15% of the initial oxygen. The different flamelets end up in the same chemical equilibrium point, because the equilibrium composition is purely determined by the enthalpy and element composition of the burnt mixture, which is the same for all flamelets. The curve corresponding to a counterflow flame with  $a = 1000 \text{ s}^{-1}$  follows a similar path as the stretchless flamelets in the 2D FGM, but crosses several of them (see figure 3.4 (b)). The mass fraction of  $CO$  is used as second controlling variable for the parametrization of this 2D manifold, because the largest relative variation occurs in the  $Y_{CO}$  profile.

This 2D FGM, as well as the 1D FGM, are used to compute counterflow flames. In fig-

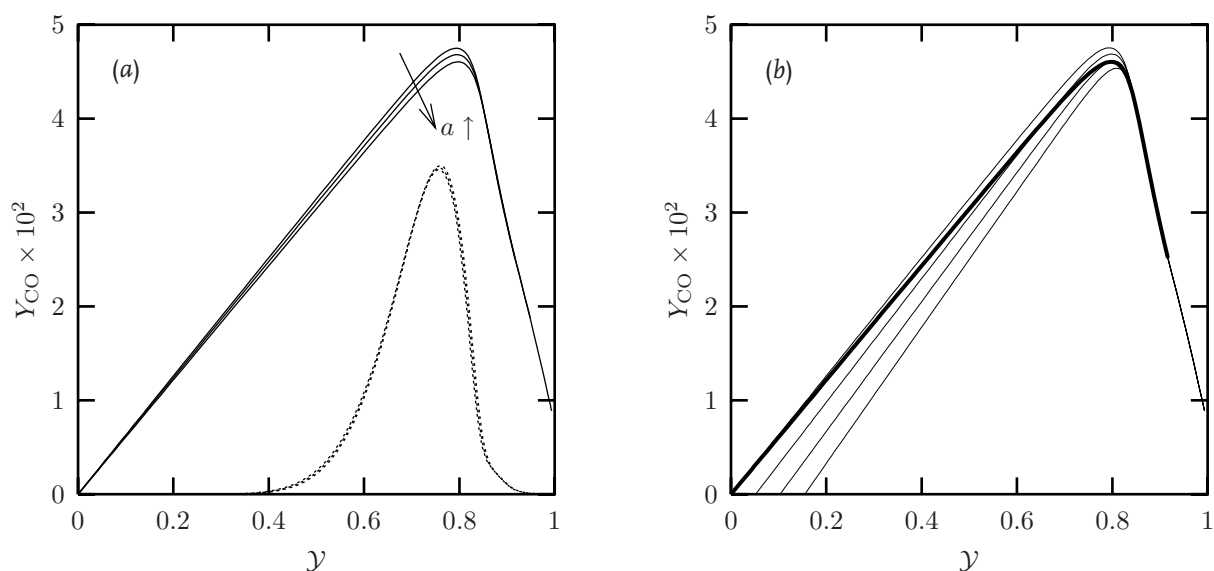


**Figure 3.4.** (a) Mass fraction of CO as function of the progress variable  $\gamma$  in a counterflow flame with  $a = 30, 500$  and  $1000 \text{ s}^{-1}$ . The arrow indicates increasing strain rate. The (three) dotted lines represent the scaled source term of the progress variable  $w_\gamma$  for the same strain rates. (b) Projection of the flamelets used to construct a 2D FGM on the  $(\gamma, Y_{CO})$ -plane. The bold line represents a counterflow flame with  $a = 1000 \text{ s}^{-1}$ .

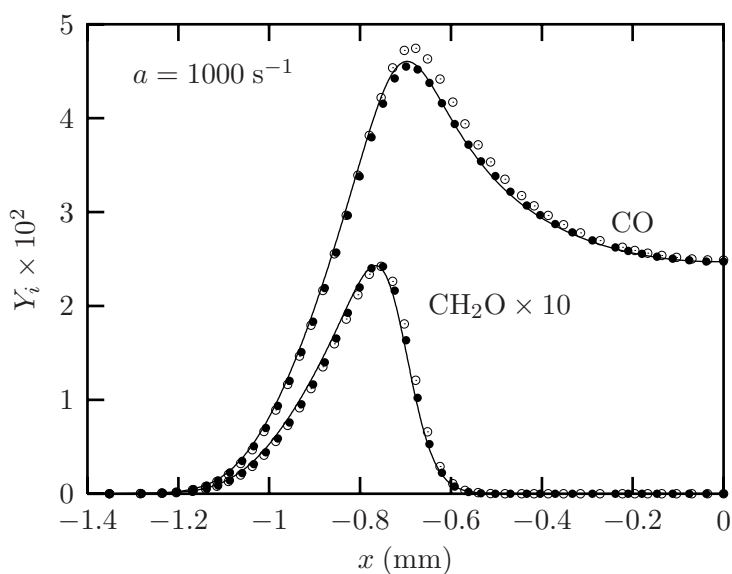


**Figure 3.5.** Mass fraction of CO and  $\text{CH}_2\text{O}$  in a counterflow flame with  $a = 1000 \text{ s}^{-1}$ . Full line: detailed chemistry; open symbols: 1D FGM; filled symbols: 2D FGM.

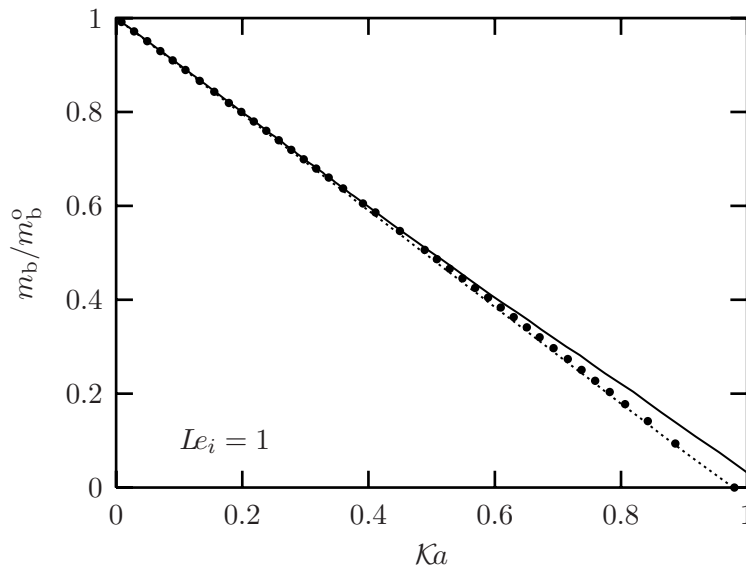


**Figure 3.6.** Scaled mass burning rate  $m_b/m_b^0$  as function of the Karlovitz integral  $Ka$  for  $Le_i = 1$ . Full line: detailed chemistry; dotted line: 1D FGM; filled symbols: 2D FGM.

ure 3.5 the mass fraction profiles of CO and CH<sub>2</sub>O in a counterflow flame with  $a = 1000 \text{ s}^{-1}$  are shown. These species are selected, because CO is affected most by flame stretch, and CH<sub>2</sub>O is a radical that is hard to predict using conventional reduction techniques. The results of the 1D FGM agree well with the detailed chemistry computations. Both the absolute values and the position of the flame front are reproduced very well. The small remaining difference in the profile of  $Y_{\text{CO}}$  is accounted for by the 2D FGM. When the 2D manifold is used, the results improve and are nearly identical to the detailed chemistry results.

The scaled mass burning rate  $m_b/m_b^0$  of these counterflow flames is plotted against the Karlovitz integral  $Ka$  in figure 3.6. The theory according to (3.14) predicts a slope of  $-1$  and agrees well with the numerical results for  $Ka < 0.5$ : a slope of  $-1.004$  is found for the detailed chemistry calculations.<sup>1</sup> The results computed with a 1D FGM are close to the detailed chemistry simulations: a slope of  $-1.023$  is found. At  $Ka = 1$ , corresponding to a strain rate of  $a = 2375 \text{ s}^{-1}$ , the flames are pushed so close to the stagnation plane that  $x_b = 0$  and  $m_b = 0$ . Even for these high strain rates the 1D manifold gives similar results as the detailed reaction mechanism. When the 1D FGM is applied, extinction occurs at strain rates higher than  $a = 3036 \text{ s}^{-1}$ , which is only 0.03% smaller than the value found for the detailed chemistry computations. This confirms that only one progress variable is enough to represent the main effect of flame stretch on the mass burning rate.

For  $Ka < 0.5$  the mass burning rates computed with the 2D FGM are better than the 1D manifold results: a slope of  $-1.009$  is found, which is closer to the detailed chemistry value. At higher strain rates ( $Ka > 0.5$ ), the detailed chemistry computations show a small relative increase of the mass burning rate compared to the theory ( $+2\%$ ). At these strain rates, both flames are pushed close together and they interact across the stagnation plane. Radicals that are present in the burnt gases, like H, O and OH, diffuse from one flame to the other. This results in a higher radical concentration in the reaction layer, which increases the reaction rates and, therefore, the mass burning rate. Since this effect is neglected in

<sup>1</sup>The numerical error in the values of the slopes is  $\pm 5 \times 10^{-4}$ .

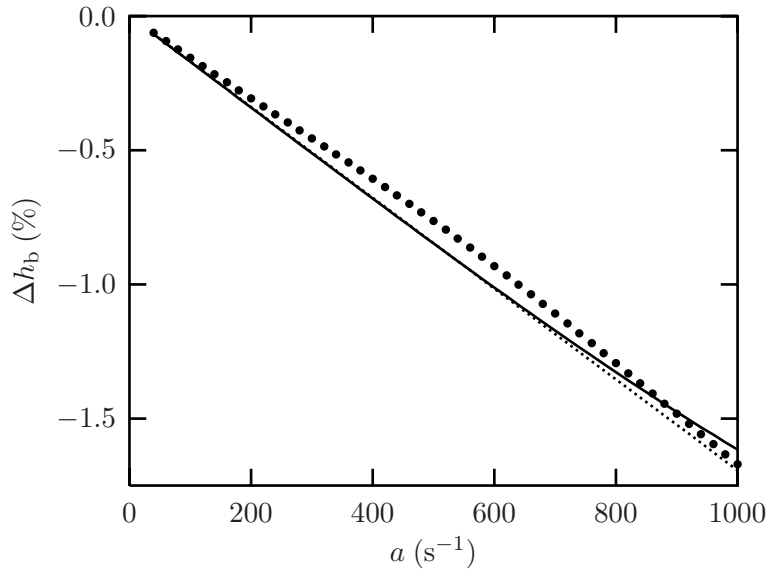


**Figure 3.7.** Variation in enthalpy  $\Delta h_b$  as function of the applied strain  $a$ . The values of  $\Delta h_b$  are scaled with  $c_{pb}^o(T_b^o - T_u)$ . Symbols: numerical; full line: theory according to (3.38); dotted line: theory according to (3.40).

the construction of both the 1D and 2D FGM, the small relative increase in  $m_b$  compared to the theory cannot be reproduced by these manifolds. How this additional effect can be included in a manifold, is explained in appendix B.

### 3.4.2 Results for $Le_i = 1.1$

In the second diffusion model, which is considered in this chapter, all Lewis numbers are assumed to be  $Le_i = 1.1$ . In this case the enthalpy changes, but the element mass fractions are constant. This makes it a suitable case to investigate how variations in a conserved variable can be accounted for by the FGM method. Counterflow flames are computed for strain rates varying from  $a = 30$  to  $1000 \text{ s}^{-1}$ . In figure 3.7 the variation in the enthalpy  $\Delta h_b$  is plotted as a function of the applied strain rate. Since the absolute value of the enthalpy has no physical meaning and depends on the reference temperature (cf. equation (1.8)), the values of  $\Delta h_b$  are scaled with  $c_{pb}^o(T_b^o - T_u)$ . The numerical results computed with the full reaction mechanism show that the enthalpy decreases for increasing strain rate. At a strain rate of  $a = 1000 \text{ s}^{-1}$  the enthalpy of the burnt mixture is decreased by approximately 1.7%, which corresponds to  $38 \text{ J g}^{-1}$ . The results agree well with the theoretical relations (3.38) and (3.40), which are shown in figure 3.7 as well. The agreement between these two relations justifies the use of stretchless variables in (3.40), especially at low strain rates. The difference between theory and numerical results originates from the diffusive fluxes  $\mathcal{G}_{hb}$ , which are neglected in both (3.38) and (3.40).

The variation of  $h_b$  has an effect on the mass burning rate. To capture this effect, the 1D manifold is extended with the enthalpy as an additional controlling variable. Such a 2D FGM is constructed by using flamelets of different enthalpy. There is a freedom of choice in how the enthalpy of a flamelet is changed. Here we consider two manifolds where the enthalpy is varied in different ways. In the first manifold (FGM A) the enthalpy of the flamelets is changed by lowering the temperature of the initial mixture  $T_{-\infty}$ . In

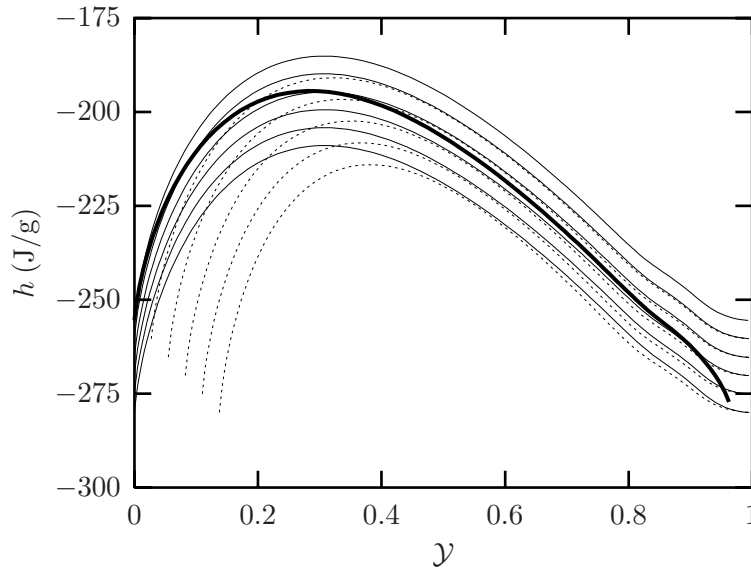


**Figure 3.8.** Projection of the flamelets used to construct a 2D FGM on the  $(\mathcal{Y}, h)$ -plane. Full lines: 2D FGM A; dotted lines: 2D FGM B; bold line: counterflow flame with  $a = 400 \text{ s}^{-1}$ .

the second manifold (FGM B) this is done by converting a part of the initial  $\text{CH}_4$  and  $\text{O}_2$  into  $\text{CO}$  and  $\text{H}_2$  and keeping the temperature  $T_{-\infty}$  constant. A projection of the flamelets used to construct these 2D FGM's on the  $(\mathcal{Y}, h)$ -plane is shown in figure 3.8. All flamelets in manifold A start at  $\mathcal{Y} = 0$ , whereas the flamelets in manifold B start at larger values, because the fraction of  $\text{H}_2$  is increased in the unburnt mixture. The flamelet in manifold B with the lowest enthalpy corresponds to a conversion of 5% of the initial oxygen. Although the initial part of the flamelets near the starting curve is different in both manifolds, the last part in the reaction layer near  $\mathcal{Y} = 1$  is almost the same. This confirms that the choice of the starting points is not crucial. The bold line in figure 3.8 represents the path in composition space from a counterflow flame with  $a = 400 \text{ s}^{-1}$ . It starts at  $(\mathcal{Y}, h) = (0, h_u)$  and shows a similar behaviour as the stretchless flamelets. However, flame stretch causes enthalpy loss in the counterflow flame and therefore, the flame path crosses several unstretched flamelets. For  $\mathcal{Y} > 0.9$ , the counterflow flame is influenced by the stagnation plane, resulting in an additional enthalpy decrease compared to the stretchless flamelets.

The effect of the enthalpy variation on the mass burning rate is shown in figure 3.9, where the mass burning rate  $m_b$  is plotted as function of  $\mathcal{K}a$ . The mass burning rate of the counterflow flames is scaled with the mass burning rate of a stretchless flame with enthalpy  $h_b^0$  and element composition  $Z_{j_b}^0$ , i.e.  $m_b^0(Z_{j_b}^0, h_b^0)$ . The decrease of the enthalpy results in a lower temperature of the burnt mixture, which, on its turn, causes the reaction rates to decrease. This leads to a small additional decrease of the mass burning rate, which can be seen in the results of the detailed chemistry computations: in this case the slope is  $-1.1$  instead of  $-1$ .

The results computed with a 1D FGM do not show this behaviour, because enthalpy changes are not accounted for in this manifold. On the other hand, both 2D FGM's can represent the additional decrease in the mass burning rate. The results are similar for both manifolds, although they are constructed with different flamelets. However, there are some differences between the results of FGM A and B that are caused by the small difference

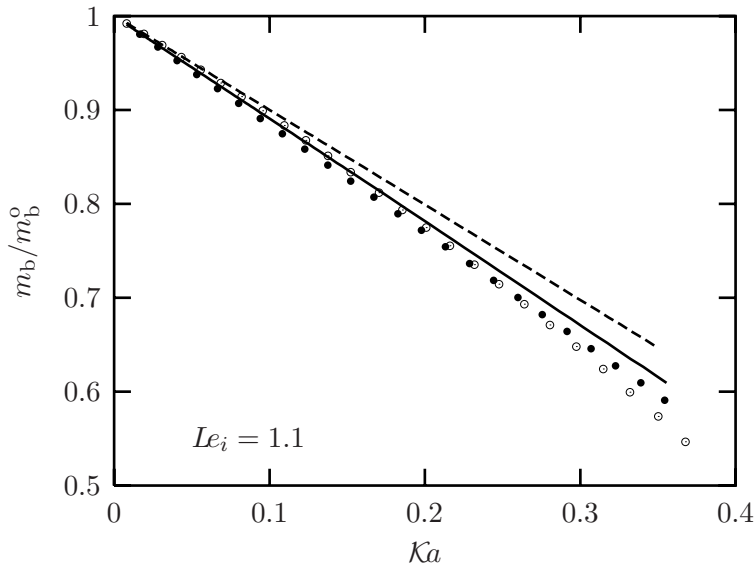


**Figure 3.9.** Scaled mass burning rate  $m_b/m_b^0(Z_{j_b}^0, h_b^0)$  as function of the Karlovitz integral for  $Le_i = 1.1$ . Full line: detailed chemistry; dashed line: 1D FGM; filled symbols: 2D FGM A; open symbols: 2D FGM B.

between the manifolds at the burnt side (around  $\mathcal{Y} = 0.8$  in figure 3.8). At low strain rates ( $Ka < 0.15$ ) the effect on  $m_b$  is slightly overestimated by FGM A, while it is underestimated by FGM B. For  $Ka > 0.15$  both manifolds result in too low values for  $m_b$ . At these higher strain rates the flame is perturbed by the boundary condition at the stagnation plane, which is not included in the manifolds. Note that since the additional effect on  $m_b$  is only small, the relative error in the results of the 2D manifolds seems large.

### 3.4.3 Results for $Le_i = \text{const}$

The third diffusion model we consider, is the most realistic model used in this chapter. The Lewis numbers are assumed to be constant and are taken from [85]. In this case variations in both enthalpy and element mass fractions occur due to the combined effect of flame stretch and differential diffusion. More realistic diffusion models can be treated in the same way, because they cause variations in  $Z_j$  and  $h$  as well.

The variations  $\Delta Z_{j_b}$  and  $\Delta h_b$  are presented in figure 3.10 for counterflow flames computed with the full reaction mechanism. It can be seen that not only the enthalpy changes, but the element mass fractions as well. The numerical results for the element mass fraction coincide well with the theory according to (3.39). At strain rates higher than  $a = 300 \text{ s}^{-1}$  the numerical results start to deviate from the theoretical results, because the weak-stretch assumption is not applicable anymore. The computed variations in  $h_b$ , however, are almost a factor of 2 larger than theory predicts. This difference is caused by the diffusive flux  $\mathcal{G}_{h_b}$ , which is neglected in the theory. However, since  $x_b$  is chosen close to the reaction layer, the gradients of  $Y_i$  cannot be neglected. Especially, the gradients of species with Lewis numbers far from unity, like H and  $\text{H}_2$ , are important for the diffusive fluxes at  $x_b$ . Because of the large value of the specific enthalpy of the hydrogen radical  $h_{\text{H}}$ , variations in the gradient of  $Y_{\text{H}}$  due to stretch have a non-negligible effect on  $\mathcal{G}_{h_b}$ .

The variations in enthalpy and element composition of the burnt gases have an effect on

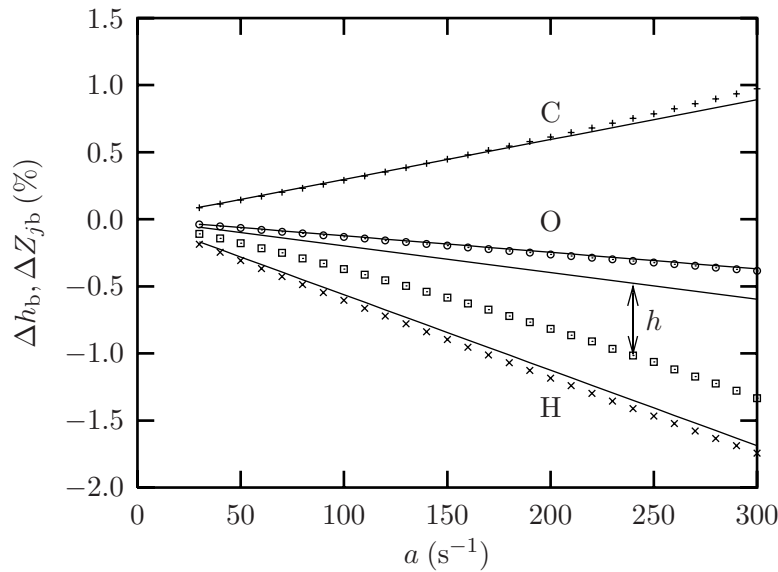


**Figure 3.10.** Relative variation in element mass fraction  $\Delta Z_{jb}$  and enthalpy  $\Delta h_b$  as function of the applied strain  $a$ . Symbols: numerical; lines: theory according to (3.39) and (3.40).

the mass burning rate. To represent this effect with FGM, the variations in  $Z_{jb}$  and  $h_b$  must be taken into account with additional controlling variables. However, since the variations  $\Delta Z_{jb}$  and  $\Delta h_b$  are coupled for weak stretch, only one additional controlling variable is needed. At higher stretch rates this coupling weakens and more dimensions should be added to the manifold.

In this section a 2D manifold (FGM C) is constructed from flamelets with different initial conditions similar to the 2D manifolds discussed in the previous subsection. The different element mass fractions and the enthalpy of the unburnt mixture are changed simultaneously following their relation  $\Delta Z_{Cb} : \Delta Z_{Hb} : \Delta Z_{Ob} : \Delta h$  found from the numerical results in figure 3.10. This relation can also be obtained by using the theoretical expressions (3.39), which are based on one stretchless flamelet. It is therefore not necessary to compute stretched flames with detailed chemistry in order to construct the FGM. The element composition is changed by varying the initial values of  $Y_{CH_4}$ ,  $Y_{O_2}$ ,  $Y_{CO_2}$  and  $Y_{N_2}$ . The initial temperature is used to change the enthalpy of the flamelets.

Counterflow flames with  $Le_i = const$  are computed by using this FGM and the full reaction mechanism. The results for the mass burning rate are presented in figure 3.11 as function of the Karlovitz integral. Since the burnt mixture becomes richer and colder for increasing stretch rates (see figure 3.10), there is an extra decrease in  $m_b$ . The slope found for  $Ka < 0.1$  is in this case  $-1.7$  instead of  $-1$ . The 1D manifold cannot represent this, because it does not take variations in  $Z_{jb}$  and  $h_b$  into account. The 2D FGM, however, includes these variations and reproduces the detailed chemistry results very well. Only at high strain rates, where the stagnation plane influences the results and where higher-order stretch effects play a role, the results deviate from the detailed chemistry computations.

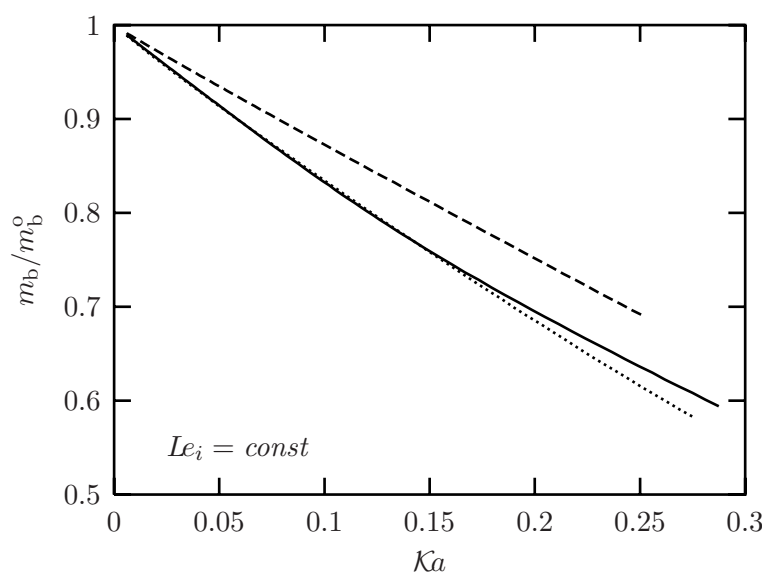


**Figure 3.11.** Scaled mass burning rate as function of the Karlovitz integral for  $Le_i = const$ . Full line: detailed chemistry; dashed line: 1D FGM; dotted line: 2D FGM C.

### 3.5 Conclusions

More insight in the effect of flame stretch is obtained by modelling premixed methane/air counterflow flames with detailed chemistry and FGM. Flame stretch is one of the main perturbations from local 1D flame behaviour that is neglected in the flamelet equations (2.23)–(2.25). Steady counterflow flames are very suitable to study flame stretch, because other perturbations such as curvature and unsteady effects are not present.

Steady counterflow flames have been computed for various applied strain rates. For increasing strain rate, the flame front is not only pushed closer to the stagnation plane, but the flame is also compressed by the applied strain, resulting in a smaller flame thickness. The correlations between the mass fractions of the different species, however, hardly change. Only a small decrease of the maximum concentration of CO is observed. However, this has no effect on the chemical source term  $\dot{\omega}_y$ , which remains almost unchanged.

The mass burning rate of premixed laminar flames is influenced significantly by flame stretch. The mass burning rate of counterflow flames with  $Le_i = 1$  decreases linearly as function of  $Ka$ , which is in very good agreement with theoretical predictions. A similar correspondence was found by De Goeij and Ten Thijs Boonkamp [33] for flames with a constant stretch rate  $\rho K$ . For Lewis numbers unequal to 1, variations in the enthalpy and element mass fractions occur, which result in an additional change of the mass burning rate as function of  $Ka$ . For  $Le_i = const$  the additional decrease of the mass burning rate is 70%. The computed variations in  $Z_{j,b}$  and  $h_b$  agree well with the theoretical expressions (3.39) and (3.40) for small strain rates. At higher strain rates higher-order stretch effects and disturbances due to the stagnation plane become important.

The results of counterflow flames computed with a 1D FGM agree well with results obtained with detailed chemistry for Lewis numbers equal to 1. The results are not only satisfactory for weak stretch, but for strain rates close to extinction as well. If a higher accuracy is desired, a second reactive progress variable can be added to the manifold. Although this is common practice in manifold methods, flamelet databases with more than

one progress variable have never been mentioned in literature so far. By using a 2D FGM we were able to reproduce the small decrease of the CO peak for increasing strain.

A multi-dimensional FGM is constructed by using flamelets with different initial compositions. Although there is a freedom of choice in the initial composition, the flamelets relax to the underlying attracting manifold and finally end up in the same chemical equilibrium. This is confirmed by the results presented in section 3.4.2 with two differently constructed 2D FGM's to account for enthalpy changes.

The results for Lewis numbers equal to 1 show that a manifold with only one progress variable is sufficient to model the main effect of flame stretch on the mass burning rate. Although the length scale related to flame stretch is in the order of the flame thickness for high strain rates ( $Ka = O(1)$ ), it is still larger than the reaction layer thickness. Therefore, the reaction layer is hardly affected by flame stretch and the chemical source term  $\dot{\omega}_\gamma$  is almost the same as in stretchless flamelets. Since  $\dot{\omega}_\gamma$  is unchanged by flame stretch and an ordinary conservation equation is solved for the progress variable, the mass burning rate is predicted correctly by FGM. The differential diffusion effects can be modelled by FGM when the variations in  $Z_{jb}$  and  $h_b$  are taken into account. Since the variations in the element mass fractions and the enthalpy are linearly coupled, one additional controlling variable is sufficient to include these changes.

Concluding from the results presented in this chapter, it appears that FGM can be used with confidence to model stretch effects in multi-dimensional flames.

# Partially Premixed Flames

## 4.1 Introduction

In the preceding chapters, FGM has been applied to purely premixed flames only. However, in many engineering applications of combustion, fuel and oxidizer are not perfectly mixed before entering the combustion chamber and combustion occurs under partially premixed conditions. Partially premixed combustion is an intermediate regime between the limiting cases of premixed and non-premixed combustion. It is well known that these limiting cases of premixed and non-premixed combustion can be modelled by using their 1D counterparts: the premixed and diffusion flamelets, respectively. For partially premixed combustion it is not clear whether to use premixed or diffusion flamelets and different approaches can be found in literature (see e.g. [61]).

Since fuel and oxidizer are not perfectly mixed in partially premixed flames, variations in the element mass fractions  $Z_j$  and enthalpy  $h$  are inevitable. The element mass fraction of carbon in a methane/air mixture for instance, varies between  $Z_C = 0.75$  in pure methane and  $Z_C = 0$  in pure air. In non-premixed flames, the local equivalence ratio, which is determined by the local element composition, is usually described by the mixture fraction  $Z$ . The mixture fraction is defined in such way that it is a conserved scalar unchanged by chemical reaction. For hydrocarbon mixtures it can be expressed in terms of the element mass fractions  $Z_C$ ,  $Z_H$  and  $Z_O$  as follows [4]:

$$Z = \frac{Z^* - Z_{\text{ox}}^*}{Z_{\text{fu}}^* - Z_{\text{ox}}^*}, \quad \text{with} \quad Z^* = 2Z_C + \frac{1}{2}Z_H - Z_O, \quad (4.1)$$

where the subscripts fu and ox denote pure fuel and oxidizer quantities, respectively. The mixture fraction has been scaled such that  $Z = 1$  in the fuel stream and  $Z = 0$  in the oxidizer stream. A differential equation for  $Z$  can be derived by taking the proper linear combination of the species conservation equations (1.25). If all Lewis numbers are assumed to be one, this differential equation for  $Z$  reads

$$\frac{\partial(\rho Z)}{\partial t} + \nabla \cdot (\rho \mathbf{u} Z) = \nabla \cdot \left( \frac{\lambda}{c_p} \nabla Z \right). \quad (4.2)$$

When Lewis numbers not equal to 1 are used, an additional term appears due to differential diffusion. For the special case of  $Le_i = 1$ , the differential equations for  $Z$ ,  $h$  and all  $Z_j$  ((4.2), (1.24) and (1.28), respectively) are exactly the same. Furthermore, when similar boundary conditions are applied, these variables will all behave the same and are related as follows:

$$Z = \frac{Z_j - Z_{j \text{ ox}}}{Z_{j \text{ fu}} - Z_{j \text{ ox}}} = \frac{h - h_{\text{ox}}}{h_{\text{fu}} - h_{\text{ox}}}. \quad (4.3)$$

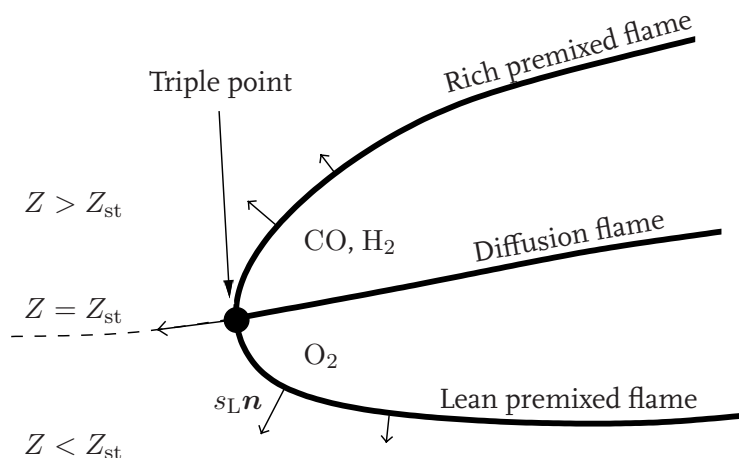


**Figure 4.1.** Schematic representation of a triple flame. The arrows indicate the local burning velocity.

In order to prevent differential diffusion effects, Lewis numbers equal to 1 are used in this chapter. In the FGM method a manifold is generated from purely premixed flamelets with a constant value of  $Z$ , apart from small local variations due to differential diffusion. To account for relatively large, global variations in the mixture fraction due to mixing,  $Z$  is added to the FGM as additional controlling variable. This is similar to the addition of  $h$  as controlling variable to account for non-adiabatic effects as described in chapter 2.

The applicability of FGM to partially premixed flames is studied by simulating triple flames. A triple flame is a flame structure generated by flame propagation in a partially premixed system. A schematic representation of such a triple (or tribrachial) flame structure is shown in figure 4.1. In a partially premixed field the mixture fraction determines the local equivalence ratio and thereby the value of the mass burning rate. A plot of the mass burning rate against the mixture fraction is shown in figure 4.2. Since premixed flame speeds are maximum for near stoichiometric conditions, a flame in a partially premixed field propagates preferentially along surfaces of stoichiometric mixture, i.e. near  $Z = Z_{st}$ . On the fuel-lean side of such a surface there is a lean premixed flame branch and on the fuel-rich side there is a rich premixed flame branch, both propagating with a lower burning velocity than the leading edge of the flame, called the triple point. For very rich or lean mixtures, the mixture fraction is beyond the flammability limits and the flame extinguishes. After the partially premixed flame front, two streams, one containing unburnt intermediates like CO and H<sub>2</sub>, and the other unburnt oxidant, come together and burn as a diffusion flame.

The interest in the study of triple flames is largely motivated by the potential role these structures play in flame propagation in partially premixed mixtures. Triple flames are of fundamental interest for the understanding of stabilization of lifted (turbulent) diffusion flames. A thorough review of the different concepts about lift-off mechanisms and blow-out criteria is given by Pitts [68]. The role of triple flames in the stabilization of jet flames is discussed by Müller *et al.* [59].

In addition to diffusion flame stabilization, triple flames can also play an important role

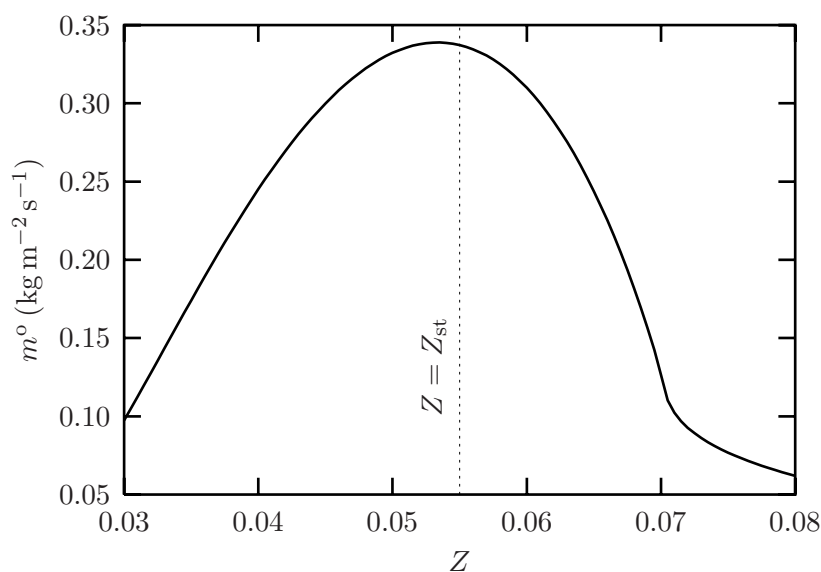


**Figure 4.2.** Mass burning rate  $m^o$  of an unstretched premixed methane/air flame as function of the mixture fraction  $Z$  for Lewis numbers equal to 1.

in the ignition processes of non-premixed systems. Numerical simulations of autoignition in non-uniform mixtures by Réveillon, Domingo and Vervisch [21, 72] clearly show that flame propagation in turbulent partially premixed systems is governed by triple flames. In addition, Peters [65] notes that  $\text{NO}_x$  emissions are likely to be large in such transient cases, and therefore an understanding of triple flames can provide essential information concerning pollutant formation.

One of the first observations of triple flames was made by Phillips [67], who investigated flame propagation in a methane/air mixing layer. More recently, a number of experimental studies on triple flames have been reported in literature. Kioni *et al.* [43] have studied the development of a triple flame in a mixing layer with a linear profile of the mixture fraction. Measurements and simulations of velocities and species distributions in a lifted laminar axisymmetric diffusion flame have been reported by Plessing *et al.* [69]. The propagation of unsteady triple flames in laminar non-premixed jets is studied experimentally by Ko and Chung [44]. Numerical simulations have been used by Ruetsch *et al.* [75] to address the relation between heat release and triple flame velocities, and by Echehki and Chen [23] and Im and Chen [39] to study the chemical structure of methanol-air and hydrogen-air triple flames. Theoretical studies considering the propagation velocity of triple flames have been reported by Buckmaster and Matalon [10], who studied the influence of Lewis number effects, and by Dold [20] and Hartley and Dold [35] who studied the effect of the mixture fraction gradient in the region of the triple point. Ghosal and Vervisch [28] included the effect of heat release in their theoretical study of the effect of the mixture fraction gradient on the propagation speed. The effect of confinement on the propagation velocity of triple flames was investigated numerically by Ruetsch and Broadwell [74].

In this chapter FGM is applied to partially premixed flames. The structure and propagation of triple flames are studied by using detailed chemistry and FGM simulations. Additionally, we investigate the influence of mixture fraction variations on the FGM method. For small  $Z$  variations the use of premixed flamelets seems justified. When the gradients in  $Z$  are increased, the deviations from local premixed behaviour increase and FGM is tested

more severely.

Since a FGM is constructed by using purely premixed flamelets, variations in the mixture fraction should be taken into account by using  $Z$  as an additional controlling variable. A description of the triple flame simulations and the manifold that is used in the reduced computations, is given in the next section. The results of detailed chemistry and FGM computations are compared in section 4.3.1. The propagation speed  $s_P$  of triple flames and its relation with the mixture fraction gradient are discussed in section 4.3.2. Not only variations in the mixture fraction cause deviations from 1D premixed flat flame behaviour in triple flames, but flame stretch and curvature as well. Therefore, the local mass burning rate at the premixed flame branches is investigated in section 4.3.3 using a flamelet analysis. Finally, results for diffusion flamelets in the triple flame are compared with results for 1D counterflow diffusion flames.

## 4.2 Numerical simulations

To simulate steady triple flames, the set of conservation equations (1.22)–(1.25) is solved in a stream function/vorticity formulation [50] in the 2D domain depicted in figure 4.2. The length and width of the domain are given by  $L_x$  and  $L_y$ , respectively. Since these dimensions are much larger than the flame thickness, a non-equidistant grid is used in order to reduce the number of grid points as much as possible. The total number of grid points used in the simulations is  $201 \times 201 = 40401$ . The results presented in this chapter were run on different grids to check that the number of grid points does not affect the final result. To keep the different grid nodes distinguishable in figure 4.2, only  $41 \times 41$  grid lines are shown. The inlet is located at the left of the domain ( $x = 0$ ). At the right side of the domain ( $x = L_x$ ), outlet boundary conditions are applied:

$$\frac{\partial u}{\partial x} = 0, \quad \frac{\partial v}{\partial x} = 0, \quad \frac{\partial Y_i}{\partial x} = 0, \quad \frac{\partial T}{\partial x} = 0. \quad (4.4)$$

The top and bottom boundaries are treated as symmetry planes, i.e.

$$\frac{\partial u}{\partial y} = 0, \quad v = 0, \quad \frac{\partial Y_i}{\partial y} = 0, \quad \frac{\partial T}{\partial y} = 0. \quad (4.5)$$

This is in contrast to many other simulations of triple flames, for which non-reflecting boundary conditions are applied in  $y$ -direction. The effect of the confinement due to symmetry boundary conditions on the propagation velocity of a triple flame is discussed by Ruetsch and Broadwell [74]. They found that the propagation speed of a triple flame is reduced by the lateral confinement.

The composition of the unburnt mixture at the inlet is prescribed by the following mixture fraction profile [27]:

$$Z_{\text{inlet}} = \frac{1}{2}(Z_1 + Z_2) + \frac{1}{2}(Z_1 - Z_2) \cos \left\{ \frac{\pi}{2} [1 - \cos(\pi y/L_y)] \right\}, \quad (4.6)$$

with  $Z_1 = 0.03$  and  $Z_2 = 0.08$  the mixture fraction at  $y = 0$  and  $y = L_y$ , respectively. These values are chosen in such way that the methane/air mixture lies within the flammability limits and that the stoichiometric value  $Z_{\text{st}} = 0.055$  lies at the center of the inlet ( $y = L_y/2$ ).

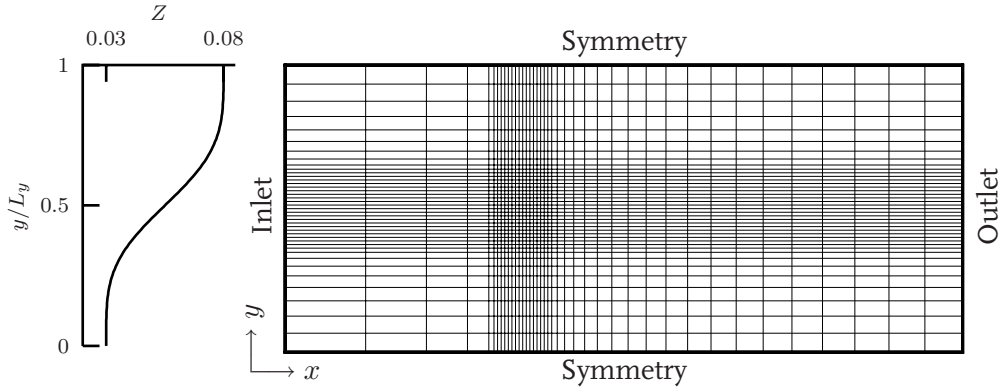


Figure 4.3. Geometry and boundary conditions for the triple flame computations.

The thickness of the mixing layer  $\delta_m$  is characterized by the slope of the mixture fraction profile at  $y = L_y/2$  and the overall change in mixture fraction, which gives

$$\delta_m(x) = (Z_2 - Z_1) \left( \frac{\partial Z}{\partial y} \Big|_{y=L_y/2} \right)^{-1}. \quad (4.7)$$

The mixing length at the inlet is a parameter of the simulation and is given by  $\delta_m^{\text{inlet}} = \delta_m(0) = 4L_y/\pi^2$ . However, it is important to realize that  $\delta_m$  does not remain constant and increases as function of  $x$  due to the diffusive nature of the flow. At the location of maximum heat release the mixing length is denoted by  $\delta_m^i$  and is more physically relevant to the flame's behaviour than  $\delta_m(0)$ .

The triple flame is stabilized in the computational domain by adjusting the inlet velocity using a procedure similar to the one implemented by Ruetsch *et al.* [75]. This method requires the flame surface velocity  $\mathbf{u}_f$ , which is determined by combining the kinematic equation (2.1) and the transport equation for  $\mathcal{Y}$ :

$$\mathbf{u}_f \cdot \mathbf{n} = \frac{-1}{\rho |\nabla \mathcal{Y}|} \left\{ \rho \mathbf{u} \nabla \mathcal{Y} - \nabla \cdot \left( \frac{\lambda}{c_p L_e \gamma} \nabla \mathcal{Y} \right) - \dot{\omega}_{\mathcal{Y}} \right\}. \quad (4.8)$$

This relation is evaluated on the centerline ( $y = L_y/2$ ) in the preheat zone, yielding the velocity correction  $\mathbf{u}_f \cdot \mathbf{e}_x$  to be applied at the inlet. If the correction would be applied to the inlet alone, it would take a number of iterations before the velocity change reaches the flame, which is both CPU intensive and may result in stability problems. Therefore, the correction is applied to all points in the flow, as a Galilean transformation, in order to reach a steady state more quickly. When the flow field reaches a steady state, the inlet velocity  $u_{\text{inlet}}$ , corresponds exactly to the propagation speed  $s_p$  of the triple flame.

We consider triple flames in a partially premixed methane/air mixture at atmospheric pressure with an unburnt temperature of  $T_u = 300$  K. The reaction mechanism given in appendix A is used for the description of the chemical processes involved in the oxidation of methane. This mechanism considers  $C_1$ -chemistry only and is therefore not very accurate under fuel-rich conditions. However, due to the relatively small number of species and reactions, this mechanism is more attractive to use in detailed chemistry computations than more complete reaction mechanisms.

The thermal conductivity and viscosity are computed from the simplified transport models (1.15) and (1.16) given in chapter 1. The species diffusivities are evaluated by using

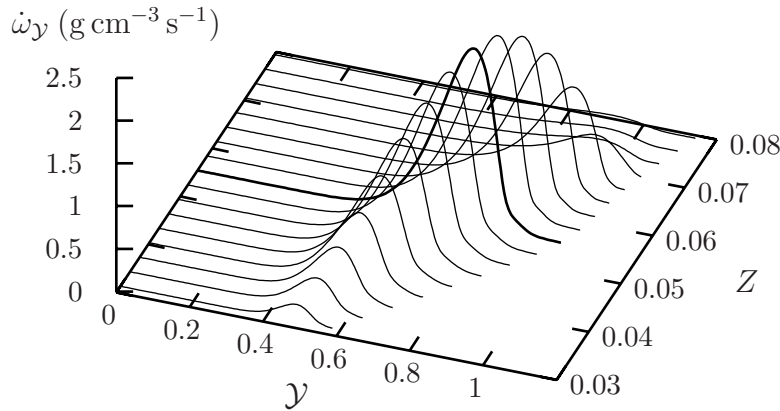


**Figure 4.4.** The chemical source term  $\dot{\omega}_Y$  of the progress variable in the flamelets used to construct a 2D FGM for partially premixed flames. Not all flamelets are shown. The bold line represents the stoichiometric flamelet.

Lewis numbers equal to 1 for all species ( $Le_i = 1$ ). This rather crude assumption results in a mass burning rate, that is significantly lower than when Lewis numbers not equal to 1 are applied. The mass burning rate of a stretchless stoichiometric flame equals  $m_{st}^o = 0.337$  and  $0.421 \text{ kg m}^{-2} \text{ s}^{-1}$  for  $Le_i = 1$  and  $Le_i \neq 1$ , respectively. Although the absolute values are different, the behaviour of the mass burning rate as function of the mixture fraction is similar. The main reason to use Lewis numbers equal to 1 is that it simplifies the analysis of the results. Since differential diffusion effects are absent in this case, the enthalpy and element mass fractions are not changed by flame stretch. It is expected that the simplified reaction and diffusion models do not prohibit us to draw general conclusions about the structure and propagation of triple flames.

In the FGM method a manifold is constructed from 1D premixed flamelets. Since the mixture fraction in such flamelets is conserved, changes in the mixture fraction as they occur in partially premixed flames, have to be taken into account by adding  $Z$  as controlling variable to the manifold. The procedure to add  $Z$  as extra controlling variable is similar to the one described in chapter 2 for adding  $h$  as variable to account for enthalpy changes. Because the triple flames considered here are adiabatic, the enthalpy is not used as additional controlling variable. In order to add the mixture fraction as additional controlling variable, the 1D flamelet equations (2.23)–(2.25) are solved for different values of the initial mixture fraction  $Z_{-\infty} = Z(x = -\infty)$ . In this work, the value of  $Z_{-\infty}$  is simply changed by varying the ratio between fuel and air in the initial mixture. It is changed in the range of  $0.0280 < Z_{-\infty} < 0.0820$  with steps of  $\Delta Z = 0.0005$ . The resulting 2D manifold is shown in figure 4.4, where the chemical source term  $\dot{\omega}_Y$  of the progress variable is plotted as function of the controlling variables  $Y$  and  $Z$ . The same progress variable as in chapter 3 is used, which is defined by (3.41). Because Lewis numbers equal to 1 are used, there are no differential diffusion effects and  $Z = Z_{-\infty}$  in each flamelet. Since the progress variable is scaled with its equilibrium value at stoichiometric conditions, the equilibrium values at other mixture fractions are not equal to 1. The equilibrium values for fuel-lean mixtures are

**Table 4.1.** Parameters and primary results of the triple flame simulations with FGM. The length of the domain is  $L_x = 23.6$  mm for all flames.

Flame	$L_y$ (mm)	$\delta_m^{\text{inlet}}/\delta_f^{\text{st}}$	$\delta_m^{\text{i}}/\delta_f^{\text{st}}$	$s_P/s_L^{\text{st}}$
I	10.0	12.2	26.5	1.84
II	8.0	9.8	21.7	1.75
III	6.0	7.3	17.3	1.60
IV	5.0	6.1	15.3	1.50
V	3.75	4.6	13.2	1.31
VI	2.5	3.1	13.5	1.02

smaller, because less  $\text{H}_2$  and  $\text{H}_2\text{O}$  are formed. For fuel-rich mixtures, the opposite holds.

A series of triple flames is computed with different mixing lengths. For smaller mixing lengths, the deviation from a purely premixed system becomes more prominent. The mixing length (or mixture fraction gradient) is changed by varying the width of the domain  $L_y$ . The length of the domain is kept constant at  $L_x = 23.6$  mm, which corresponds to  $L_x = 70 \delta_f^{\text{st}}$ , with  $\delta_f^{\text{st}} = 0.337$  mm the premixed flame thickness at stoichiometric conditions. The flame thickness is defined as

$$\delta_f = \int_{s_u}^{s_b} \tilde{\mathcal{Y}} \, ds, \quad (4.9)$$

following the ideas of the Integral Analysis explained in section 3.2. In (4.9) the progress variable is scaled such that  $\tilde{\mathcal{Y}}_b = 1$  for fuel-rich and lean conditions as well. To avoid that the flow boundary conditions at the inlet affect the propagation speed, the triple point is stabilized far away from the inlet at a distance of  $x \approx 23 \delta_f^{\text{st}}$ . The triple point is defined as the point of maximum heat release at the stoichiometric mixture fraction contour.

The parameters and primary results of the triple flame simulations are shown in table 4.1. The numerical configuration described in this section is chosen similar to the one used by Favier *et al.* [27]. A comparison of the results presented in this chapter with their results is given by Herrmann [36].

All flames have been computed by using the 2D FGM discussed above. Flame IV has been computed with detailed chemistry as well. Using a code that was not optimized for detailed chemistry, the computation time of this simulation exceeded several weeks, while the FGM simulation lasted approximately two days. Because of the very long CPU-times, detailed chemistry simulations have been limited to one case only.

## 4.3 Results

In this section the results of the triple flame simulations are presented. First some general characteristics of triple flames are described and the results computed with detailed chemistry and FGM are compared. In subsection 4.3.2 results are presented for different mixing lengths and the propagation speed  $s_P$  of the triple flames is discussed. Finally, the structure of both premixed and diffusion flamelets in a triple flame are studied.

### 4.3.1 Comparison detailed chemistry/FGM

Before the results of detailed chemistry and FGM are compared, a description of the general structure of the methane/air triple flame is given in terms of temperature and species profiles. Iso-contours of temperature  $T$  and the species mass fractions  $Y_{\text{CH}_4}$ ,  $Y_{\text{O}_2}$ ,  $Y_{\text{CO}}$ ,  $Y_{\text{H}}$  and  $Y_{\text{CH}_2\text{O}}$  are shown in figure 4.5 for Flame IV computed with detailed chemistry and FGM. Notice that not the whole computational domain is shown, but only 12 mm of the complete  $x$  range. The ticks on the axes are separated by 1 mm.

The most characteristic scalar field of a flame is that of temperature. The premixed flame branches can clearly be identified. The temperature rises from 300 K in the unburnt mixture to approximately 2000 K behind the premixed flame branches depending on the local stoichiometry. The highest temperatures of approximately 2150 K are found in regions of near-stoichiometric mixture. However, because heat is conducted away from the stoichiometric line, these temperatures are almost 100 K lower than the maximum equilibrium temperature of 2240 K.

In the unburnt gases the mass fraction of methane equals the mixture fraction and ranges from  $Y_{\text{CH}_4} = 0.08$  at the fuel-rich side to  $Y_{\text{CH}_4} = 0.03$  at the fuel-lean side. Due to diffusion and redirection of the flow in lateral direction, the gradient in  $Y_{\text{CH}_4}$  (and therefore in  $Z$  as well) decreases as function of  $x$  in front of the triple flame. In the premixed flame front, methane is decomposed into more stable fuels like CO and  $\text{H}_2$ . A large amount of CO can be found in the mixture behind the fuel-rich premixed flame branch. On the lean side,  $\text{O}_2$  survives through the premixed flame and diffuses towards the stable reactants behind the fuel-rich branch.

The radical profiles for H and formaldehyde ( $\text{CH}_2\text{O}$ ) in Flame IV are shown in figure 4.5 as well. Both species concentrations peak on the fuel-rich side close to the triple point. The  $\text{CH}_2\text{O}$  concentration shows a second peak in the fuel-rich premixed flame branch at the boundary of the domain. Following the  $\text{C}_1$  path discussed in chapter 1, formaldehyde is converted through HCO into CO in the premixed flame branch. The H radicals are produced behind the fuel consumption layer near the burnt gas side of the premixed flame, and diffuse upstream towards the unburnt gas, where they play an important role in the break up of the fuel.

The propagation speed of Flame IV computed by using detailed chemistry is  $s_{\text{P}} = 44.0 \text{ cm s}^{-1}$ . When FGM is used, the propagation speed is  $s_{\text{P}} = 44.7 \text{ cm s}^{-1}$ ; a difference less than two percent. This small difference indicates that FGM yields accurate results for these triple flames. This is confirmed by the temperature and species profiles shown in figure 4.5. For most variables the results of the detailed and reduced chemistry computations agree very well. For the temperature and the major species, hardly any difference can be observed. Because transport processes along the iso-surfaces of  $\mathcal{Y}$  are not included in FGM, the CO formed on the fuel-rich side cannot diffuse along the premixed flame towards the fuel-lean side. Therefore, the CO concentration behind the fuel-rich premixed flame branch is a few percent over-predicted by FGM.

The radical mass fractions  $Y_{\text{H}}$  and  $Y_{\text{CH}_2\text{O}}$  are very hard to predict using existing reduction methods. However, when using FGM the results agree well with the results of detailed chemistry computations. Since the radical concentrations are mainly determined by the concentrations of the major species, the small over-prediction of CO on the fuel-rich side results locally in a lower value of  $Y_{\text{CH}_2\text{O}}$ .

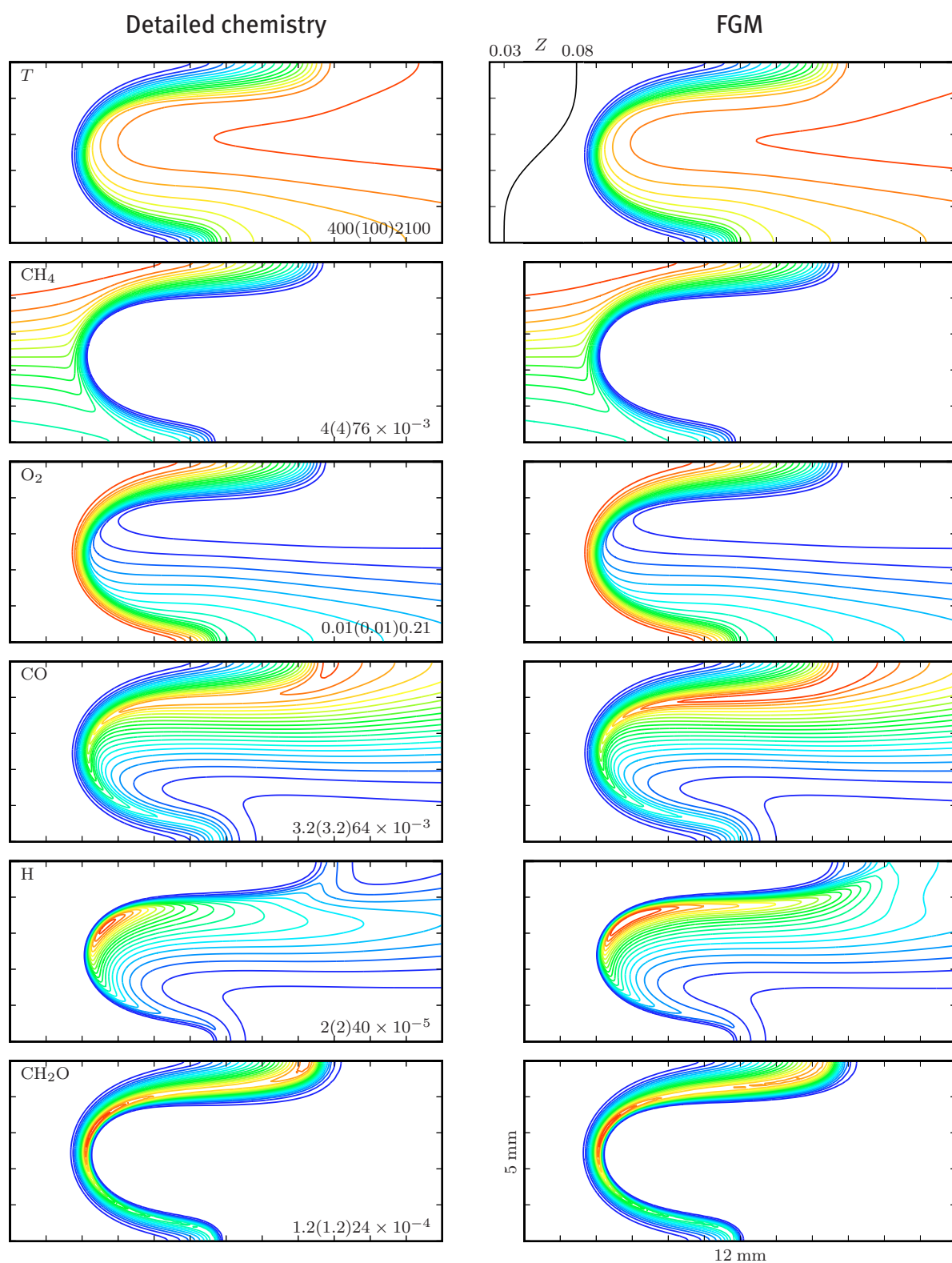


**Figure 4.5.** Iso-contours of  $T$ ,  $Y_{CH_4}$ ,  $Y_{O_2}$ ,  $Y_{CO}$ ,  $Y_H$  and  $Y_{CH_2O}$  for Flame IV computed with detailed chemistry (left) and FGM (right). Only a part ( $12 \times 5$  mm) of the complete computational domain (figure 4.2) is shown. The contours are drawn at equal intervals indicated in the lower right corner covering the entire range of each variable. The same iso-levels are used for the detailed chemistry and FGM results.

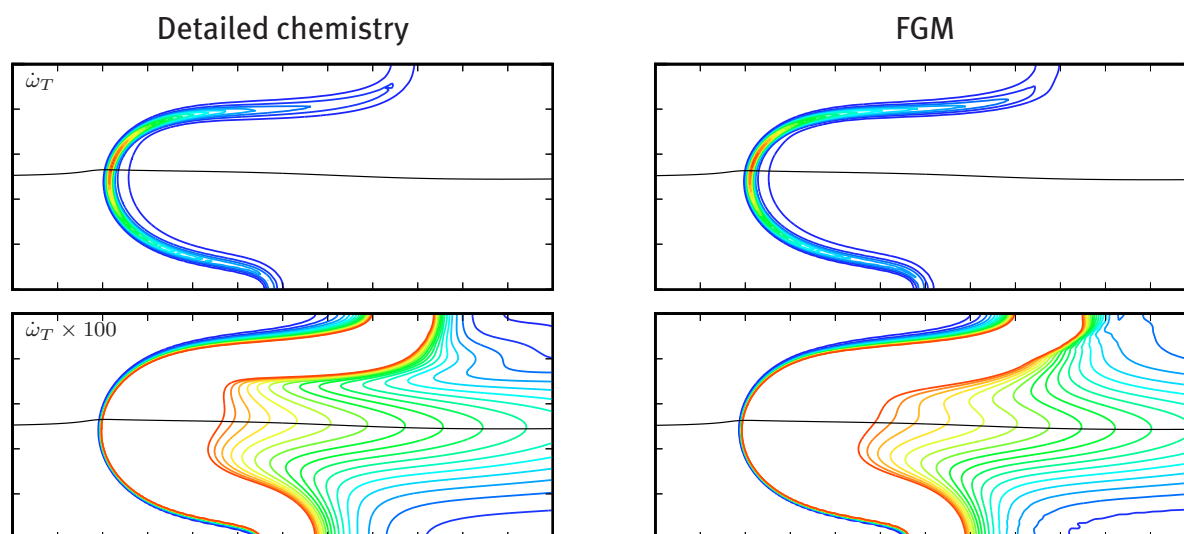


**Figure 4.6.** Heat release  $\dot{\omega}_T$  in Flame IV computed with detailed chemistry (left) and FGM (right). The same iso-levels are used in all graphs:  $25(25)450 \times 10^7 \text{ J m}^{-3}$ . The lower graphs show the original data multiplied by 100. The black lines denote the stoichiometric mixture fraction iso-contours.

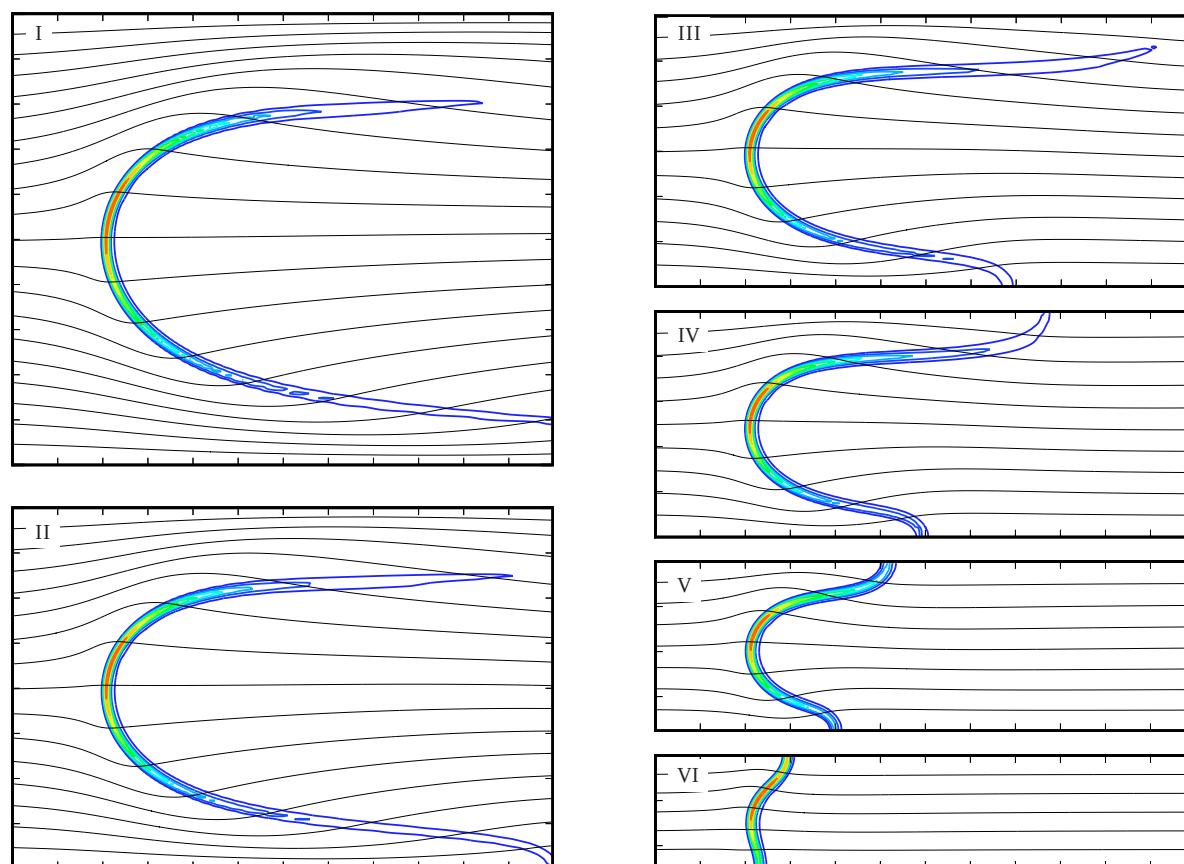


**Figure 4.7.** Chemical source term  $\dot{\omega}_y$  of the progress variable for different mixing lengths. The contours are drawn at equal intervals covering the entire range:  $25(25)450 \times 10^7 \text{ J m}^{-3}$ . The black lines represent streamlines.

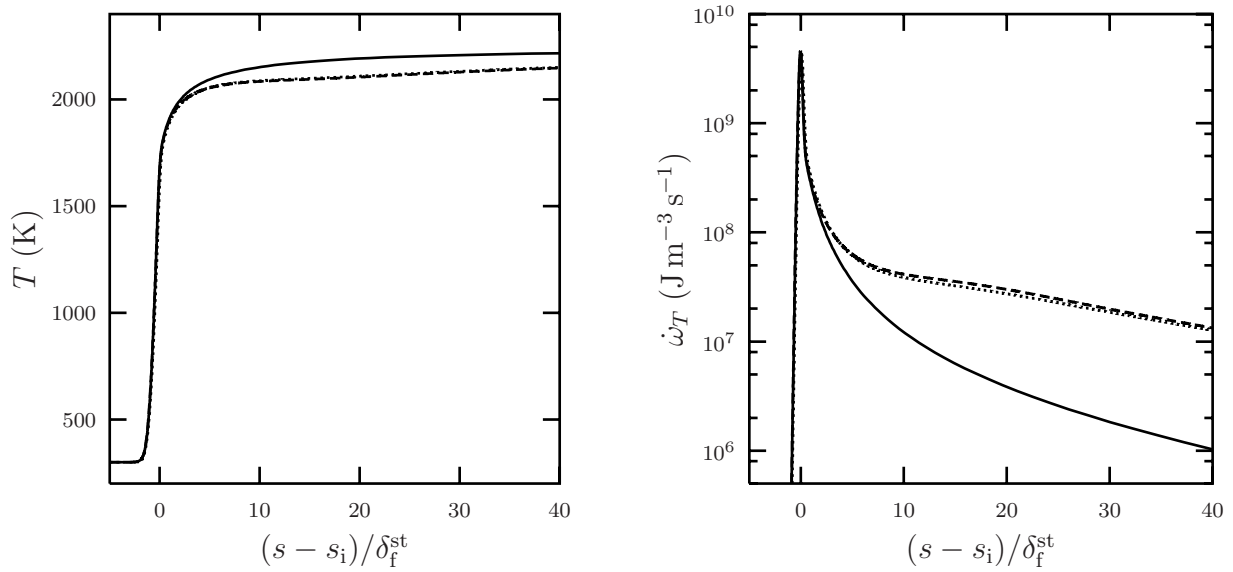


**Figure 4.8.** Temperature  $T$  (left) and heat release  $\dot{\omega}_T$  (right; log-scale) in Flame IV along the stoichiometric mixture-fraction contour. Dashed line: detailed chemistry; dotted line: FGM. The full line represents a stoichiometric 1D premixed flame.

Besides temperature, the heat release  $\dot{\omega}_T$  defined as

$$\dot{\omega}_T = - \sum_i^{N_s} h_i \dot{\omega}_i, \quad (4.10)$$

is an important characteristic of flames. The heat release distributions in Flame IV computed with detailed chemistry and FGM are shown at the left and right in figure 4.6, respectively. The original data is plotted in the upper graphs, while the lower graphs present the same data multiplied by 100 in order to show the structure of the small values. The triple flame structure of this flame can clearly be identified in this figure. Although the heat release in the premixed flame branches is approximately two orders of magnitude larger, the trailing diffusion flame can be observed by its heat release in both detailed chemistry and FGM computations.

Another way to indicate the presence of a diffusion flame is to compare profiles of temperature and heat release along the stoichiometric contour in a triple flame with those of a stoichiometric 1D premixed flame. These profiles are plotted in figure 4.8 as function of the arc-length  $s$ . The arc-length is made dimensionless with the flame thickness  $\delta_f^{\text{st}}$  and its origin is chosen at the point of maximum heat release  $s = s_i$ . The profiles coincide in the premixed flame region. Behind the premixed reaction zone differences between the 1D flame and the triple flames can be observed. Due to lateral diffusion of heat, the temperature in the triple flames is almost 100 K lower than in the 1D case. On the other hand, diffusion of excess oxygen and intermediate fuels behind the premixed flame branch towards the stoichiometric line cause an increase in the reaction rate resulting in a higher heat release than in the 1D flame. For increasing mixture fraction gradient, these differences become larger. The difference between the temperature profiles computed with detailed chemistry and FGM is not visible in figure 4.8.

The heat release in the diffusion flame computed with FGM is approximately 5% higher than for the detailed chemistry computation. This difference is caused by a small local

difference in  $\mathcal{Y}$ . Because the  $\text{H}_2\text{O}$  concentration behind the fuel-rich flame branch is higher in the detailed chemistry computation,  $\mathcal{Y}$  has a higher value than in the FGM computation. Since in the FGM case  $\mathcal{Y}$  is further away from the chemical equilibrium value, the heat release is higher than in the detailed chemistry computation. Because the values of  $\dot{\omega}_T$  are small in the trailing diffusion flame, the relative difference seems high (5%). However, the difference in  $\mathcal{Y}$  is only 0.5%.

### 4.3.2 Flame propagation and mixing length

So far we have not considered the velocity field in our analysis. In this section we discuss the velocity field of a triple flame and the effect of the mixing length  $\delta_m$ . In figure 4.7 the chemical source term  $\dot{\omega}_\gamma$  of the progress variable is shown for the different triple flames. If we compare the heat release profiles in figure 4.6 with the profiles of  $\dot{\omega}_\gamma$  in figure 4.7, we can conclude that  $\dot{\omega}_\gamma$  and  $\dot{\omega}_T$  are closely correlated. The flow field is presented by means of streamlines, which are superimposed on the  $\dot{\omega}_\gamma$  contours in figure 4.7.

Due to the homogeneous Neumann boundary conditions at the symmetry planes, the profile of  $Z$  in  $y$ -direction is flattened by lateral diffusion and the mixture fraction gradient decreases as function of  $x$ . As a result the maximum and minimum value of  $Z$  in the premixed flame branch tend to the stoichiometric value and are less extreme than their values at the inlet. This effect has an increasing influence for decreasing  $\delta_m^{\text{inlet}}$ . It results in an increase of the reaction rate near the boundaries and in an attachment of the premixed flame branches to the boundaries (see figure 4.7). For Flame VI the minimum and maximum value of  $Z$  in the premixed flame front are  $Z = 0.045$  and  $Z = 0.063$ , respectively. Furthermore, the effective mixing length  $\delta_m^i$  at the triple point of Flame VI is larger than for Flame V, although the mixing length  $\delta_m^{\text{inlet}}$  at the inlet is smaller (see table 4.1). So, for these small domain widths, smaller  $\delta_m^{\text{inlet}}$  do not lead to smaller  $\delta_m^i$ . Therefore, the mixture fraction gradient cannot be increased further with this method for a more stringent test of the FGM method.

Heat release in the premixed flame branches strongly influences the flow field ahead of the flame structure. Thermal expansion in the premixed flame front causes an increase in the component of the velocity normal to the flame front. This jump in the normal velocity bends the streamlines towards the stoichiometric line. To accommodate this redirection of the flow, the streamlines ahead of the flame diverge. Due to this divergence, the velocity directly ahead of the triple flame is lower than the oncoming velocity far upstream. Since the velocity directly ahead of the triple point is almost equal to the premixed burning velocity  $s_L^{\text{st}}$ , the propagation speed of the triple flame structure is higher than  $s_L^{\text{st}}$ . The propagation speeds  $s_P$  of triple flames with different mixing lengths are given in table 4.1. For smaller mixing lengths the curvature of the premixed flame front increases and the divergence ahead of the flame decreases, resulting in lower propagation speeds. As argued by Ruetsch and Broadwell [74], the confinement of the triple flame also affects the propagation speed. Since the flow is confined in  $y$ -direction, the divergence ahead of the flame is smaller than for the unconfined case. Therefore, a comparison of the propagation speed with theoretical expressions [35, 28], which only consider unconfined flames, does not make much sense.

The effect of flow divergence on the propagation speed is elucidated in figure 4.9, where the dimensionless mass flow rate is plotted along the stoichiometric mixture-fraction contour. The dimensionless mass flow is defined as  $\rho(\mathbf{u} \cdot \mathbf{e}_s)/m_{\text{st}}^0$ , with  $\mathbf{e}_s$  the unit vector along the  $Z = Z_{\text{st}}$  contour. This figure shows clearly that the mass flow rate decreases ahead

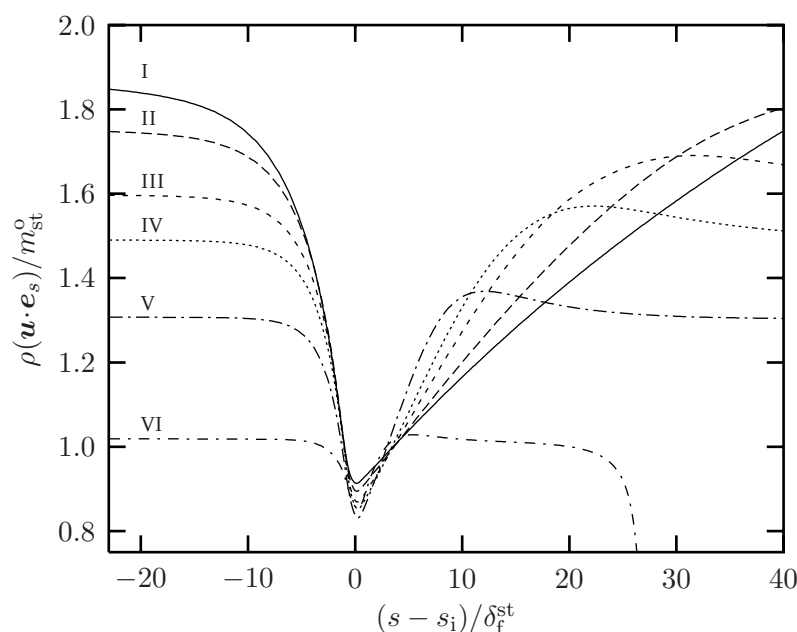


**Figure 4.9.** Dimensionless mass flow  $\rho(\mathbf{u} \cdot \mathbf{e}_s)/m_{st}^0$  along the stoichiometric mixture-fraction contour for flames I–VI computed with FGM.

of the flame. Therefore, the upstream value is higher than the mass flow rate at the triple point, which is approximately the same as the mass burning rate of a stoichiometric premixed flame  $m_{st}^0$ . Behind the premixed flame front the streamlines converge causing an increase in the mass flow. Far downstream the flow becomes uniform and  $\rho(\mathbf{u} \cdot \mathbf{e}_s)$  becomes equal to its value at the inlet. However, behind the flame front of flame VI the mixture fraction is almost constant. Therefore, the stoichiometric mixture-fraction contour of flame VI bends towards the rich side for  $s - s_i > 20\delta_f^{st}$ . As a result  $\mathbf{e}_s$  is diverted in lateral direction and  $\rho(\mathbf{u} \cdot \mathbf{e}_s)$  decreases for flame VI.

Although the propagation speed  $s_p$  of most triple flames is significantly larger than the mass burning rate of a stoichiometric premixed flame, the local mass burning rate at the triple point is 10 to 20% lower than  $m_{st}^0$ . This decrease of the mass burning rate is caused by flame stretch. Since the stretch rate increases with increasing curvature of the premixed flame front, this effect is larger for smaller mixing lengths. The influence of flame stretch on the local mass burning rate at the premixed branches is studied in more detail in the next section.

### 4.3.3 Flamelet analysis

In this section we discuss the structure and behaviour of flamelets in the premixed and diffusion flame branches.

#### Premixed flamelets

In the previous section, we have found that the propagation speed of a triple flame is governed by flow divergence ahead of the flame and the local mass burning rate in the premixed flame branch. The latter is investigated with a flamelet analysis similar to the analysis of the mass burning rate of counterflow flames in chapter 3. In order to do so, the 1D

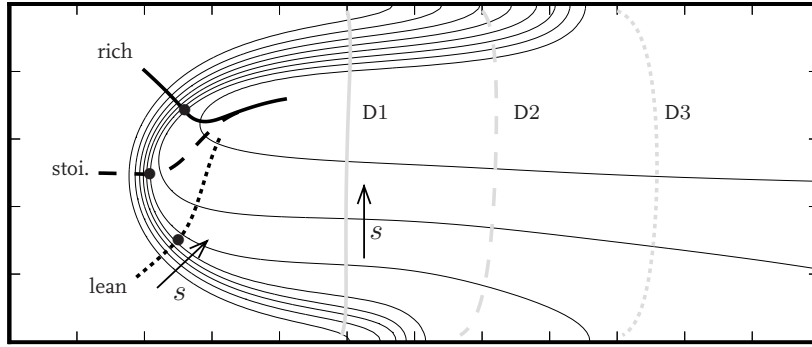


**Figure 4.10.** Premixed (black) and diffusion (gray) flamelets in Flame IV. Full black line: premixed fuel-rich flamelet; dotted black line: premixed fuel-lean flamelet; dashed black line: premixed near-stoichiometric flamelet. Full gray line: diffusion flamelet D1; dashed gray line: diffusion flamelet D2; dotted gray line: diffusion flamelet D3. The thin lines are iso-contours of the progress variable  $\mathcal{Y}$ . The bullets indicate the position of the inner layer  $s_i$  in the premixed flamelets.

flamelets have to be reconstructed from the triple-flame solution. This is done by integrating in the direction normal to the iso-surfaces of the progress variable. The 1D flame path is then given by

$$\mathbf{x}(s) = \mathbf{x}_{-\infty} - \int_{s_u}^s \mathbf{n} ds', \quad (4.11)$$

with  $\mathbf{x}_{-\infty}$  the starting point in the unburnt mixture. In figure 4.10, three premixed flamelets in Flame IV are shown: one starting on the fuel-rich side, one on the fuel-lean side and one near stoichiometric conditions. Since the iso-contours of  $Z$  and  $\mathcal{Y}$  are not perpendicular ( $\nabla Z \cdot \nabla \mathcal{Y} \neq 0$ ), the flamelets cross iso-contours of  $Z$  and thus,  $Z$  changes in the premixed flamelets. Because the progress variable contains the mass fraction of  $\text{H}_2$  and  $\text{H}_2\text{O}$ , the progress variable reaches a higher value at fuel-rich conditions. Therefore, the flamelets bend towards the fuel-rich side in the burnt gases.

Temperature profiles in these three flamelets are shown in figure 4.11. In this figure the temperature is plotted as function of the arc-length  $s$ , which is scaled with the flame thickness  $\delta_f^{\text{st}}$ . The origin is chosen at the position of maximum heat release. This reaction layer in a premixed flame is often referred to as the inner layer [78]. The slope of the temperature profile in the preheat zone of the near-stoichiometric flamelet is steeper than for the fuel-rich and fuel-lean case. This is caused by the higher flow velocity in the preheat zone of the near-stoichiometric flamelet. This can be seen in the right graph of figure 4.11, in which the mass burning rate  $m$  in the flamelets is plotted. In the preheat zone the mass burning rate decreases due to flame stretch. Behind the inner layer, this continues for the fuel-lean and near-stoichiometric flamelets. The mass burning rate of the fuel-rich flamelet, however, increases behind the inner layer.

The explanation for this behaviour can be found in figure 4.12, in which the dimensionless stretch rate  $\rho K \delta_f^{\text{st}} / m_{\text{st}}^{\text{o}}$  and curvature term  $\kappa m \delta_f^{\text{st}} / m_{\text{st}}^{\text{o}}$  in these flamelets are shown. The definitions of  $\rho K$  and  $\kappa$  are given by (2.8) and (2.12), respectively. The mass burning rate is changed by flame stretch and curvature according to (2.16). A positive stretch rate decreases  $m$  as function of  $s$ , while positive curvature leads to an increase of  $m$ . In the preheat

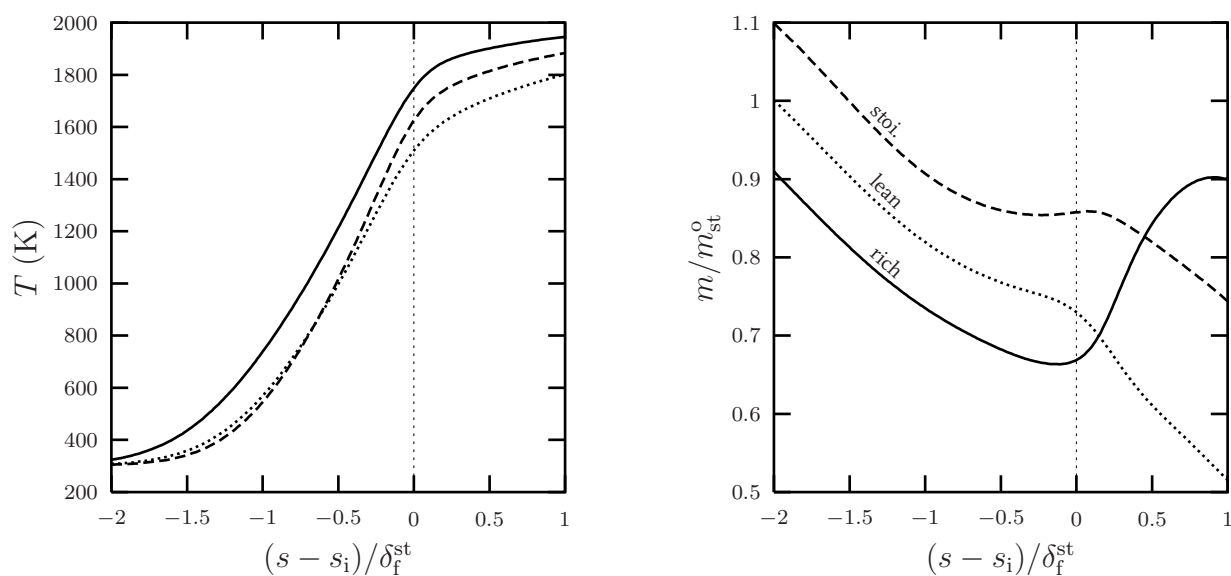


**Figure 4.11.** Temperature and dimensionless mass burning rate profiles along the premixed flamelets shown in figure 4.10. Full line: fuel-rich; dotted line: fuel-lean; dashed line; near stoichiometric.

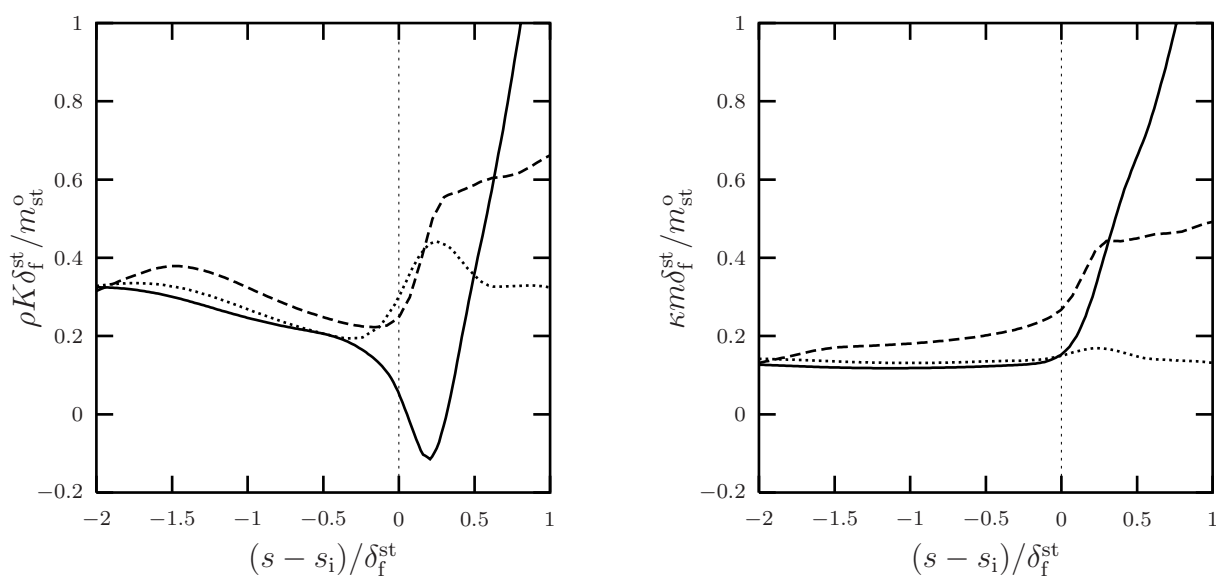


**Figure 4.12.** Dimensionless flame stretch  $\rho K \delta_f^{\text{st}}/m_{\text{st}}^{\circ}$  and curvature  $\kappa m \delta_f^{\text{st}}/m_{\text{st}}^{\circ}$  terms for the premixed flamelets shown in figure 4.10. Full line: fuel-rich; dotted line: fuel-lean; dashed line; near stoichiometric.

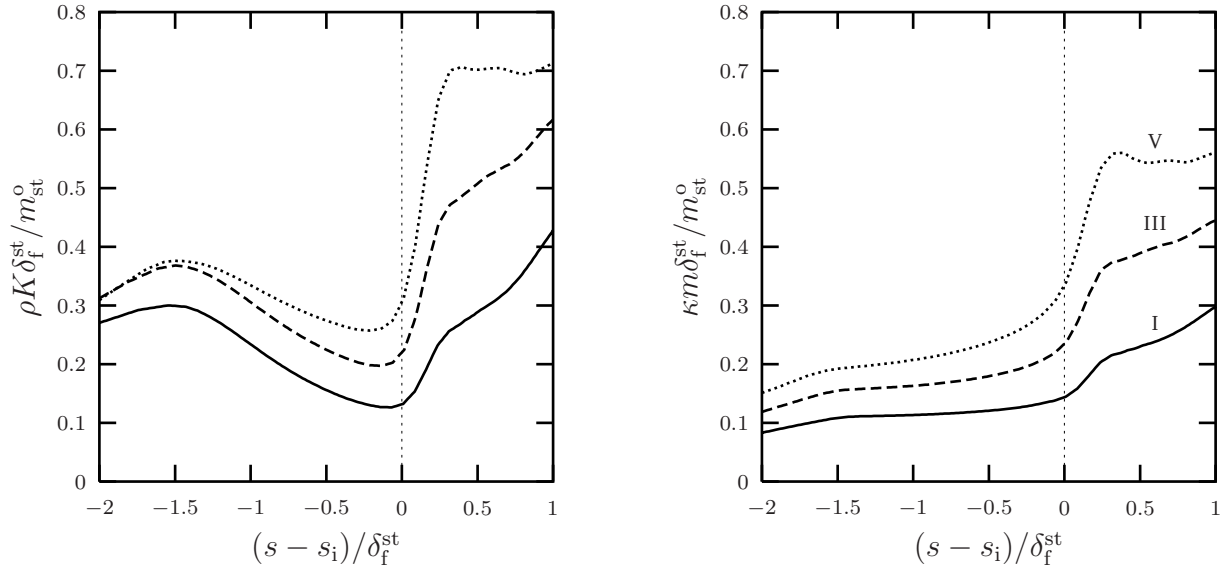


**Figure 4.13.** Dimensionless flame stretch  $\rho K \delta_f^{st} / m_{st}^0$  and curvature  $\kappa m \delta_f^{st} / m_{st}^0$  terms for the near-stoichiometric premixed flamelets in Flame I (full), III (dashed) and V (dotted).

zone the stretch term is larger than the curvature term and therefore, the mass burning rate decreases. Behind the inner layer the curvature of the flame surfaces increases, especially for the fuel-rich case. In the fuel-rich flamelet the curvature term becomes larger than the flame stretch term, resulting in an increase of the mass burning rate.

In figure 4.13 the flame stretch  $\rho K$  and curvature  $\kappa m$  terms are shown for the near-stoichiometric flamelets in Flame I, III and V. The profiles are similar for the different flames. However, for smaller mixing lengths the premixed flame front becomes more curved and, because curvature contributes to stretch, the stretch rate increases. Figure 4.12 and 4.13 clearly show that  $\rho K$  is not small, which makes the use of weak-stretch approximations in theoretical studies doubtful. Moreover, since the stretch rate changes significantly through the flamelet, constant stretch-rate assumptions are not applicable either.

In section 3.2 we derived an expression for the mass burning rate  $m_b$  in the burnt mixture of stretched flames. However, the mass burning rate  $m_i$  at the position of the inner layer, where most heat is released, is more physically relevant. This value governs the propagation of the premixed flame front through the mixture. Furthermore, Groot and De Goey [34] have shown that the unstretched mass burning rate is independent of flame curvature, only when  $m$  is evaluated in the inner layer. The mass burning rate in the inner layer is related to  $m_b$  by the continuity equation:

$$m_b \sigma_b - m_i \sigma_i = - \int_{s_i}^{s_b} \sigma \rho K ds. \quad (4.12)$$

For the unstretched case this yields

$$(m_b \sigma_b)^0 = (m_i \sigma_i)^0. \quad (4.13)$$

Notice that  $m_i^0 = m^0$  for  $\sigma = const$ , with  $m^0$  the mass burning rate of a flat, stretchless flame. Combining (4.12) and (4.13) with expression (3.13) for  $m_b$ , gives us an expression

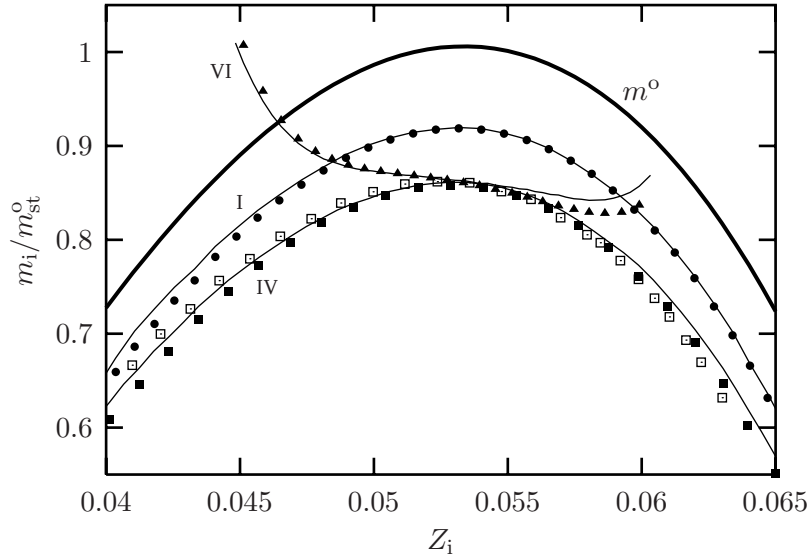


**Figure 4.14.** Mass burning rate  $m_i$  as function of the mixture fraction  $Z_i$  in the inner layer for Flames I ( $\bullet$ ), IV ( $\blacksquare$ ) and VI ( $\blacktriangle$ ). Results for Flame IV computed with detailed chemistry are denoted by open squares ( $\square$ ). Symbols: numerical; thin lines: theory according to (4.14). The bold line represents the mass burning rate  $m^o$  of a stretchless, premixed, flat flame.

for the mass burning rate in the inner layer:

$$m_i = m_i^o - \frac{1}{\sigma_i} \left( \int_{s_u}^{s_b} \sigma \rho K \mathcal{V} ds - \int_{s_i}^{s_b} \sigma \rho K ds \right). \quad (4.14)$$

The first term between parentheses on the right-hand side represents that the mass burning rate in the inner layer is affected by the stretch field throughout the whole flamelet. The second term is just a correction needed to translate the result from  $s = s_b$  to the inner layer.

The mass burning rate in the inner layer is shown in figure 4.14 for Flame I, IV and VI. For each triple flame a series of flamelets is reconstructed and for each flamelet  $m_i$  is plotted against the mixture fraction  $Z_i$  at the inner layer. Due to flame stretch,  $m_i$  is almost 10% lower than the mass burning rate  $m^o(Z)$  of a stretchless premixed flame for Flame I. Since the stretch rate is higher in Flame IV, the decrease in  $m_i$  is larger than for Flame I. For Flame IV,  $m_i$  is approximately 15% smaller than  $m^o$ . This decrease does not change significantly as function of  $Z_i$ , because stretch and curvature are more or less constant along the premixed flame branch of these flames.

The structure of Flame VI is, however, quite different: near the triple point the flame front is convex towards the unburnt mixture, but at the fuel-rich and fuel-lean sides it is concave. Therefore, the flame stretch rate decreases away from the triple point and becomes even negative at the fuel-lean side. As a result the difference between  $m_i$  and  $m^o$  decreases for fuel-rich and fuel-lean conditions. For  $Z_i < 0.047$ , the mass burning rate in the inner layer becomes even higher than  $m^o$ .

By integrating along the flamelets, the mass burning rate can be determined according to (4.14). These predictions of  $m_i$  are plotted in figure 4.14 as well. The comparison with the numerical results can be considered very satisfactory. Close to the triple point at

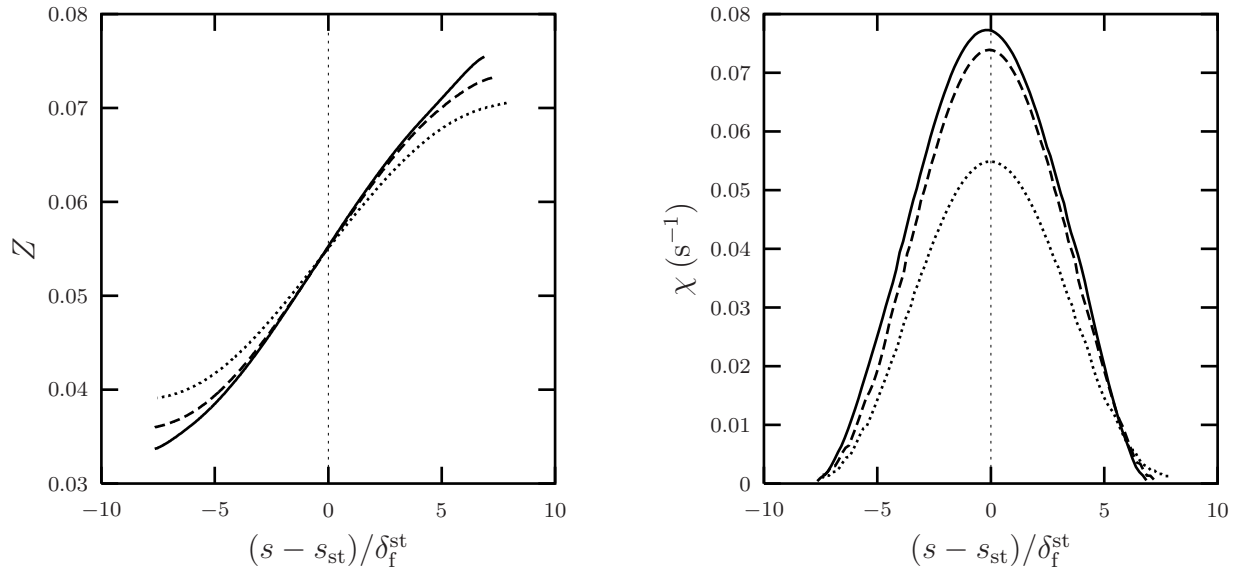


**Figure 4.15.** Mixture fraction  $Z$  and scalar dissipation rate  $\chi$  profiles along the diffusion flamelets D1 (full), D2 (dashed) and D3 (dotted) shown in figure 4.10.

stoichiometric conditions the difference between numerical results and theory is negligible. Away from stoichiometry the differences increase, because the reaction layer becomes thicker and variations in  $Z$  through the flamelet become larger.

So far, the results presented in this section are based on simulations using FGM. A similar analysis can be performed for the results computed with detailed chemistry. The mass burning rate at the inner layer of Flame IV computed with detailed chemistry is plotted in figure 4.14 as well. Again the comparison between FGM and detailed chemistry results is very satisfactory.

### Diffusion flamelets

For the trailing diffusion flame a similar analysis can be performed. Diffusion flamelets are reconstructed from the triple flame solution by integrating in the direction normal to isocontours of  $Z$ . The 1D diffusion flame path is then given by (4.11) with  $\mathbf{n} = -\nabla Z/|\nabla Z|$  in this case. The starting points  $\mathbf{x}_{-\infty}$  are chosen close to the boundary at the lean side. The flame paths of three diffusion flamelets in Flame IV are displayed in figure 4.10. The diffusion flamelets D1, D2 and D3 are located at approximately 3, 5 and 7 mm downstream of the triple point, respectively.

The mixture fraction profiles along these diffusion flamelets are shown in figure 4.15, where  $Z$  is plotted as function of the arc-length  $s$ . The arc-length is scaled with the premixed flame thickness  $\delta_f^{st}$  and the origin is chosen at the position  $s = s_{st}$ , where  $Z = Z_{st}$ . The mixture fraction in the flamelets increases from approximately  $Z \approx 0.035$  on the fuel-lean side to  $Z \approx 0.075$  on the fuel-rich side. Due to the diffusive nature of the flow, the gradient  $\partial Z/\partial s$  decreases for flamelets further downstream. This mixture fraction gradient is closely related to the scalar dissipation rate  $\chi$ , which is an important characteristic of diffusion flamelets. The scalar dissipation rate is defined as:

$$\chi = 2D|\nabla Z|^2 = \frac{2\lambda}{\rho c_p} \left( \frac{\partial Z}{\partial s} \right)^2, \quad (4.15)$$

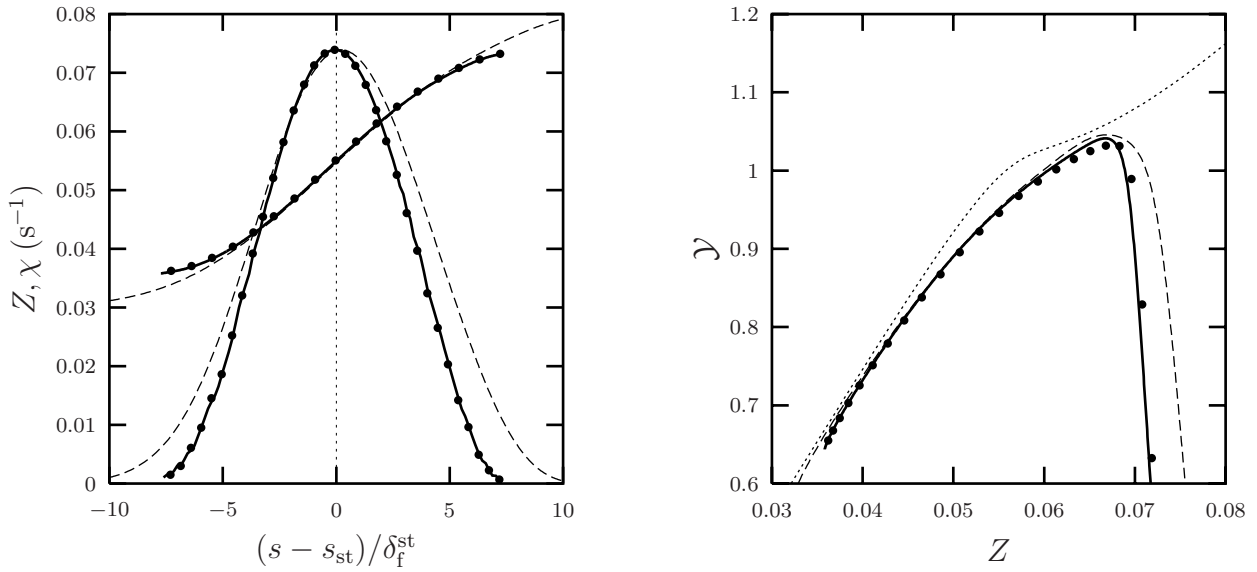


**Figure 4.16.** Mixture fraction  $Z$  and scalar dissipation rate  $\chi$  as function of the arc-length  $s$  (left) and the progress variable  $\mathcal{Y}$  as function of  $Z$  (right) for diffusion flamelet D2 in flame IV and a counterflow diffusion flame with  $a = 81.5 \text{ s}^{-1}$ . Full line: flamelet based on detailed chemistry computation; symbols: flamelet based on FGM computation; dashed line: counterflow flame; dotted line: chemical equilibrium.

which is the inverse of a characteristic diffusion time scale. The scalar dissipation rate for the diffusion flamelets is shown in figure 4.15 as well. The profiles of  $\chi$  are bell-shaped with their maximum near  $Z = Z_{\text{st}}$ . Since the gradient of  $Z$  decreases for flamelets further downstream, the maximum value of  $\chi$  decreases as well.

The diffusion flamelets in the triple flames are compared with the most elementary diffusion flame: the quasi-1D counterflow diffusion flame. The counterflow diffusion flame configuration is similar to the configuration of premixed counterflow flames depicted in figure 3.1, but with opposing fuel and oxidizer streams. These flames are governed by the same set of equations (3.18–3.20, 3.24) as the premixed counterflow flames in chapter 3. However, since the opposing flows have different compositions, the problem is not symmetric as in the premixed case and other boundary conditions have to be applied. In most studies on counterflow diffusion flames, one stream consists of fuel ( $Z = 1$ ) and the other of oxidizer ( $Z = 0$ ). In this study, we use unburnt mixtures with  $Z_{-\infty} = 0.03$  and  $Z_{\infty} = 0.08$  as boundary conditions in order to resemble the flamelets in the triple flame as close as possible. Since these mixtures are within the flammability limits, the diffusion flame is enclosed between two premixed flames. In fact, this flame structure can be considered as a quasi-1D triple flame.

First a series of counterflow diffusion flames is computed with detailed chemistry for different applied strain rates  $a$ . The scalar dissipation rate in counterflow diffusion flames increases for increasing strain rates. Subsequently, diffusion flamelet D2 is compared with a counterflow flame with the same scalar dissipation rate  $\chi_{\text{st}} = 0.074$  at stoichiometric conditions. In figure 4.16, the profiles of  $Z$  and  $\chi$  are plotted for flamelet D2 and the corresponding counterflow flame with  $a = 81.5 \text{ s}^{-1}$ . The behaviour of both  $Z$  and  $\chi$  is very similar for these flames. Due to the boundary conditions for the triple flame simulations, the gradients of  $Z$  at fuel-rich and fuel-lean conditions are smaller for flamelet D2 than for

the counterflow flame.

Since the mixture fraction is a continuously increasing function of  $s$ , diffusion flamelets can be parametrized by  $Z$ . In studies on diffusion flames it is therefore common practice to present results in mixture fraction space. In figure 4.16, the progress variable  $\mathcal{Y}$  is shown in mixture fraction space for flamelet D2 and the corresponding counterflow flame. The chemical equilibrium value  $\mathcal{Y}_{\text{eq}}(Z)$  is shown as well. Because flamelet D2 lies almost completely behind the premixed flame branch, the progress variable has a high value close to  $\mathcal{Y}_{\text{eq}}$ . At  $Z = 0.068$  the flamelet enters the premixed flame branch and  $\mathcal{Y}$  suddenly drops. Similar behaviour can be observed for the counterflow flame, albeit for a higher value of  $Z$ . When transport along iso-surfaces of  $Z$  is neglected and the transformation

$$\frac{\partial}{\partial s} = \frac{\partial Z}{\partial s} \frac{\partial}{\partial Z} \quad (4.16)$$

is applied, the conservation equation for the species mass fractions along the diffusion flamelets can be written as (see e.g. [64])

$$-\rho \frac{\chi}{2} \frac{\partial^2 Y_i}{\partial Z^2} = \dot{\omega}_i, \quad (4.17)$$

stating that there is a balance between diffusion along the flamelet and reaction. Due to this balance, the chemical equilibrium value  $\mathcal{Y}_{\text{eq}}$ , where  $\dot{\omega}_i = 0$ , is not reached in the diffusion flamelets.

The results of flamelet D2 based on the triple flame simulation using FGM are almost the same as the results computed with detailed chemistry. Although the FGM database consists of premixed flamelets, the diffusion part of the flame seems to be modelled accurately by FGM. Since an ordinary 2D conservation equation for the progress variable is solved, transport of  $\mathcal{Y}$  in all directions is accounted for. Therefore, the differences between the results computed with detailed chemistry and FGM are mainly caused by differences in the chemical source term. Since the composition in the diffusion tail of the triple flame is close to chemical equilibrium, for which chemistry is dominant and ILDM and FGM are identical, the composition can be described very accurately by only one progress variable. Thus, because the chemical source term is well described by FGM and diffusion of  $\mathcal{Y}$  along the diffusion flamelets is accounted for, the results of the reduced computations agree well with the results of the detailed chemistry simulations.

## 4.4 Conclusions

In this chapter FGM has been applied to partially premixed flames. Triple flames have been simulated for different mixing lengths with detailed chemistry and FGM. The mixing length has been decreased by decreasing the size of the computational domain in  $y$ -direction. However, lateral diffusion reduces the gradient of  $Z$  so much for small domain widths, that the mixing length at the flame front increases for decreasing  $L_y$ . In order to study larger variations of  $Z$  along the flame front, the mixing length  $\delta_m^i$  should be controlled in another way.

Due to the relatively large mixing length, the trailing diffusion flame is less prominent than the premixed flame branches. The heat release in the diffusion flame is two orders of magnitude smaller than that in the premixed flame branches. Since the diffusion flame is

embedded in the burnt gases of the premixed flame front, the mixture composition in the diffusion flame is close to chemical equilibrium.

The propagation of triple flames is governed by flow redirection that occurs in front of the flame. This redirection is a consequence of the acceleration of normal velocity across the premixed flame front. For large mixing lengths the redirection of the flow increases and as a result the propagation speed increases. Due to the confinement in lateral direction, the redirection — and thus the propagation speed — is smaller than for 'free' triple flames. In [74], Ruetsch and Broadwell concluded that the propagation speed of confined triple flames is equal to the premixed burning velocity, i.e.  $s_P = s_L$ . This is, however, in contradiction with the results from Herrmann [36] and the results presented in this chapter.

The structure of the different flame branches has been studied by using a flamelet analysis. The amount of flame stretch and curvature appeared to be significant in the premixed flame branches. This makes the use of weak-stretch approximations in theoretical studies doubtful. Since flame stretch contains contributions due to curvature, the stretch term is higher for flames with a smaller mixing length. The curvature of the premixed flame front increases for decreasing mixing length. The local mass burning rate in the premixed flame branches is affected significantly by flame stretch. For Flame IV the mass burning rate is approximately 15% smaller than the mass burning rate of a stretchless premixed flame. The results obtained with the flamelet analysis agree with the results from Herrmann [36]. The structure of the trailing diffusion flame has been analyzed as well. It appeared that the diffusion flamelets are very similar to 1D counterflow flames with a similar scalar dissipation rate.

To account for mixture fraction variations in the FGM method,  $Z$  is added to the manifold as additional controlling variable. The agreement between the results of the triple flame computed with detailed chemistry and FGM is very satisfactory. Since transport of species along iso-surfaces of  $\mathcal{Y}$  is not included in the FGM computations, differences appear for species, whose concentration changes significantly along the premixed flame front. The differences are only small for the flames studied here, because the length scale of the variations along the flame front are much larger than the premixed flame thickness, i.e.  $\delta_m^i \gg \delta_f$ .

Although the variations in  $Z$  are small, flame stretch and curvature result in significant deviations from local 1D flame behaviour. The length scales associated with flame stretch  $s_L K^{-1}$  and curvature  $\kappa^{-1}$  are in the same order of magnitude than the premixed flame thickness  $\delta_f$ . However, since the reaction layer thickness is typically much smaller than  $\delta_f$ , the chemistry (or chemical source term  $\omega_{\mathcal{Y}}$ ) is not affected by stretch and curvature. Therefore, the local mass burning rate is reproduced accurately with FGM, which on its turn results in the correct shape of the premixed flame front.

In the trailing diffusion flame only small deviations from chemical equilibrium occur, because the scalar dissipation rate is much smaller than the chemical reaction rates. In this high-temperature region, the mixture composition can be described by only one reactive controlling variable and ILDM and FGM are identical. Therefore, the FGM results agree very well with the detailed chemistry computations. For smaller mixing lengths, the scalar dissipation rate and the deviation from chemical equilibrium will increase. In order to maintain a certain accuracy at higher dissipation rates, the dimension of the manifold can be increased by adding extra progress variables.

Finally, it can be concluded that — at least for the flames considered here — a premixed flamelet database can be used to model partially premixed flames accurately.



# Application to a Semi-Practical Combustion System

## 5.1 Introduction

In the previous chapters we have seen that FGM is an accurate and efficient method to model (partially) premixed laminar flames. The results of simulations with detailed chemistry are reproduced by FGM within a fraction of the computation time. This makes FGM a powerful tool to study combustion processes, not only in scientific research but also in industrial applications. In order to investigate the applicability of FGM to more realistic problems, it is used to model the combustion process in a semi-practical combustion system.

In this chapter the FGM method is used to model the combustion process on a ceramic-foam surface burner in a radiating furnace. Surface burners are of particular interest since they have a very low  $\text{NO}_x$  emission due to the cooling of the gases before they burn [91]. At the Eindhoven University of Technology, surface burners have been studied since 1992. Bouma *et al.* [7, 8] studied the stability, performance and radiative output of ceramic-foam surface burners in a cold environment. The performance and stability of ceramic-foam burners in high temperature systems, where the risk of flashback is enlarged, has been investigated by Lammers [47]. In this chapter, we consider the experimental set-up Lammers used in his work. In contrast to the research of Lammers, the main goal of this work is not to study the behaviour of this semi-practical burner system, but to show that efficient and accurate numerical simulations of such a system can be performed by using FGM.

The outline of this chapter is as follows. The experimental set-up is described in the next section. In section 5.3, the numerical method is discussed. Attention is given to the treatment of the ceramic-foam burner and to radiation modelling. The numerical results are presented in section 5.4 and are compared with thermocouple measurements.

## 5.2 Experimental set-up

The experimental setup has been designed to investigate the stability and performance of a ceramic-foam burner in a hot radiating furnace [48] and is shown in figure 5.1. The furnace consists of a cylinder of fire-resistant bricks, referred to as wall, and a duraboard plate which is referred to as the top disk. The inside of the bricks is polished to a cylinder with a radius of 15.5 cm. In the top disk a cylindrical ceramic-foam burner with a radius of 10 cm is fitted. The flame stabilizes at the lower surface of the burner. Instead of placing the burner at the bottom of the furnace, this configuration has been selected in order to prevent condensing

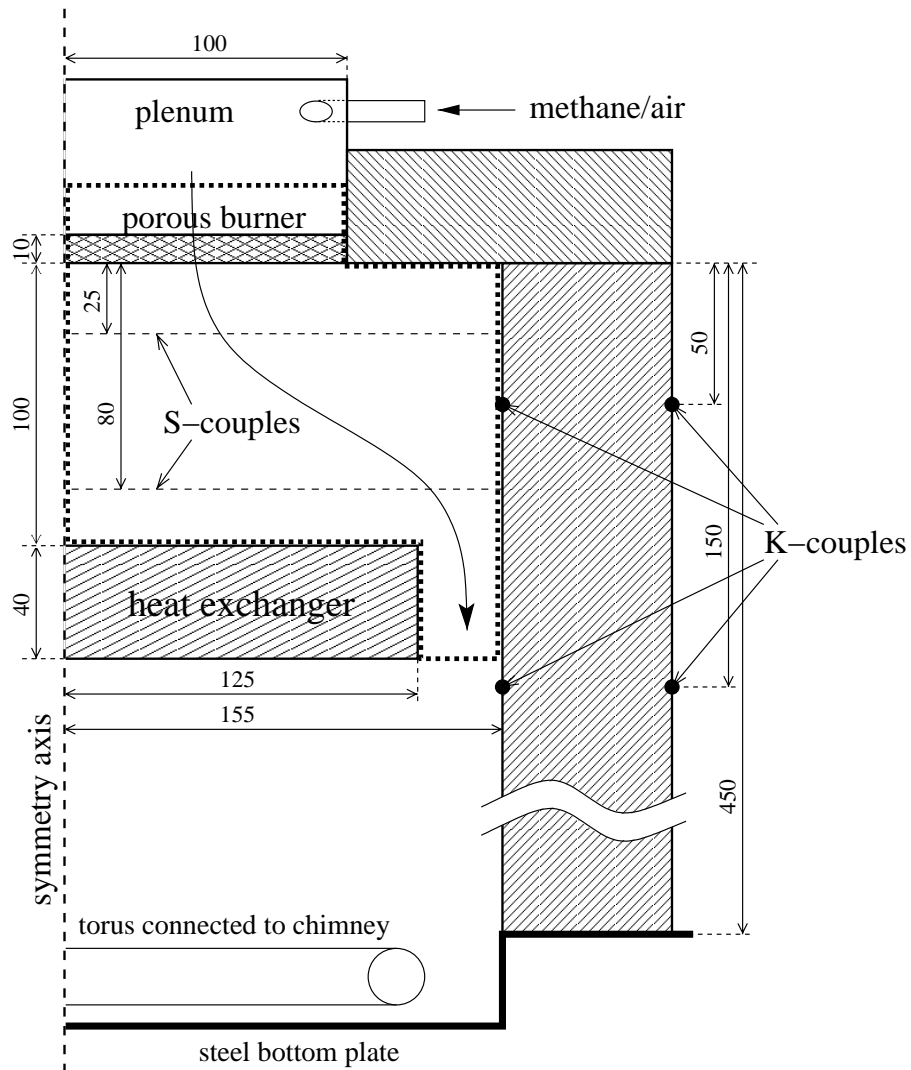


**Figure 5.1.** Schematic cross section of the experimental setup. The thick dotted line denotes the computational domain. The curved arrow indicates the flow direction. All dimensions are in mm.

water to fall onto the burner, because this may lead to fracture of the burner.

A water-cooled, steel heat exchanger with a radius of 12.5 cm is located opposite to the burner and provides good boundary conditions for both the flow and temperature. In the experimental set-up the radiating temperature of the environment can be controlled by changing the vertical position of the heat exchanger. In this work, the distance between the downstream surface of the burner and the heat exchanger is set to 10 cm. The heat exchanger divides the furnace in a hot upper part and a relatively cold, lower part. Due to the relatively narrow gap between the heat exchanger and the wall, there is almost no radiative heat transfer between the two zones. Moreover, since the flow has to pass through the narrow gap, the influence of the lower part of the furnace on the upper part is negligible. Therefore, the computational domain is restricted to the upper part of the furnace. At the bottom of the furnace, the flue gases leave the furnace through a torus that is connected to a chimney.

In the furnace, both gas and wall temperatures are measured. Wall temperatures are measured by using K-type thermocouples located at 5 and 15 cm below the burner at the inside and outside of the brick wall. The accuracy of the thermocouples is 2 K for the inner-wall thermocouples and 5 K for the outer-wall thermocouples [47]. Gas temperatures are measured by inserting S-type thermocouples into the furnace through holes in the brick wall at 2.5 and 8 cm below the burner. The thermocouples consist of a combination of a pure platinum wire and a platinum wire with 10% rhodium. The measured temperatures are corrected for radiative heat losses. The uncertainty in the gas temperatures varies from 2 K near the heat exchanger to 40 K near the burner [47].

The composition and velocity of the unburnt mixture is controlled by two mass-flow controllers, one for methane and one for air. In this work, the unburnt methane/air mixture has a temperature of  $T_u = 300$  K and an equivalence ratio of  $\phi = 0.9$ . Furthermore, the furnace is operated at atmospheric pressure with a thermal load of  $200 \text{ kW m}^{-2}$ , which corresponds to a uniform inlet velocity of  $v_{\text{inlet}} = 7 \text{ cm s}^{-1}$ .

## 5.3 Numerical simulation

### 5.3.1 Porous burner

The ceramic-foam burner is implemented as a two-phase region with the solid-fluid interaction given by volume-averaged terms. The conserved quantities of the gas phase are multiplied by the porosity  $\eta$ , being the volume fraction of the gas phase, to account for the presence of the solid phase. Assuming that the tortuosity of the gas phase equals 1, mass conservation of the gas phase is given by

$$\nabla \cdot (\eta \rho \mathbf{u}) = 0, \quad (5.1)$$

and the conservation equation for the progress variable becomes

$$\nabla \cdot (\eta \rho \mathbf{u} \mathcal{Y}) - \nabla \cdot \left( \eta \frac{\lambda}{Le_{\mathcal{Y}} c_p} \nabla \mathcal{Y} \right) = \eta \dot{\omega}_{\mathcal{Y}}. \quad (5.2)$$

The momentum equation is extended with a solid-fluid interaction term to account for the flow resistance of the porous medium:

$$\nabla \cdot (\eta \rho \mathbf{u} \mathbf{u}) = -\nabla(\eta p) - \nabla \cdot (\eta \boldsymbol{\tau}) + \eta \rho \mathbf{g} - R_{\text{DF}} \mathbf{u}. \quad (5.3)$$

**Table 5.1.** Properties of the combustion system used in the numerical simulation.

Property	Symbol	Value	
Porosity	$\eta$	0.8	–
Tortuosity	$\tau_s$	0.4	–
Conductivity	$\lambda_s$	$1.0 \cdot 10^{-1}$	$\text{W m}^{-1} \text{K}^{-1}$
Heat transfer coefficient	$\alpha_v$	$4.0 \cdot 10^6$	$\text{W m}^{-3} \text{K}^{-1}$
Wall emissivity	$\epsilon$	0.4	–

The porous medium is assumed to be isotropic and its resistance is modelled by a Darcy-Forchheimer equation

$$R_{\text{DF}} = \frac{\mu}{c_1} + c_2 \rho |\mathbf{u}|, \quad (5.4)$$

with the coefficients  $c_1 = 3.0 \times 10^{-9} \text{ m}^2$  and  $c_2 = 1.2 \times 10^3 \text{ m}^{-1}$  derived from experiments [7]. To include the gas-solid heat transfer inside the porous burner and radiative heat exchange outside the foam, the enthalpy equation has been extended with two extra terms, viz.

$$\nabla \cdot (\eta \rho \mathbf{u} h) - \nabla \cdot \left( \eta \frac{\lambda}{c_p} \nabla h \right) = \nabla \cdot (\eta \mathcal{H}) - \alpha_v (T - T_s) + Q_{\text{rg}}, \quad (5.5)$$

where  $T_s$  and  $T$  denote the temperature of the solid and gas phase, respectively. The second term on the right-hand side of (5.5) accounts for the heat transfer between gas and solid in the ceramic-foam burner with  $\alpha_v$  the volumetric heat transfer coefficient. Outside the ceramic-foam burner this term is zero. The second extra term is a radiation term,  $Q_{\text{rg}}$ , which is only important outside the foam burner and accounts for the radiative heat transfer due to gas radiation.

Inside the porous burner, an equation for the temperature  $T_s$  of the solid phase is solved. The temperature  $T_s$  follows from the balance between conduction, gas-solid heat transfer and radiative heat transfer  $Q_{\text{rs}}$  in the porous region:

$$-\nabla \cdot ((1 - \eta) \tau_s \lambda_s \nabla T_s) = \alpha_v (T - T_s) + Q_{\text{rs}}, \quad (5.6)$$

with  $\tau_s$  the tortuosity and  $\lambda_s$  the heat conduction coefficient of the solid phase. The properties of the ceramic foam used in the simulation are given in table 5.1.

### 5.3.2 Radiation

Radiation plays an important role in many combustion applications and is essential for radiant surface burners. Moreover, since the radiative heat flux is proportional to  $T^4$ , radiative heat transfer is very important in the high-temperature furnace considered here.

The radiation terms both inside and outside the ceramic foam ( $Q_{\text{rg}}$  and  $Q_{\text{rs}}$  in (5.5) and (5.6), respectively) are determined with the Discrete-Transfer method developed by Shah [80]. The Discrete-Transfer method is a ray-tracing technique, which calculates the radiative transfer by integrating the radiative transfer equation along a predetermined set of rays. In general, gas radiation is highly spectrally dependent. However, due to the required computational effort needed to solve the complex spectral structure of gas radiation, the gas

is assumed to behave as a gray gas with spectrally independent properties. The radiative transfer equation for such a gray gas is given by

$$\frac{di'}{d\ell} = -k(i' - \frac{\sigma_S T^4}{\pi}), \quad (5.7)$$

which relates the local radiative intensity  $i'$  to the path length  $\ell$ , the local absorption coefficient  $k$  and the temperature of the gas phase. In (5.7),  $\sigma_S$  denotes the Stefan-Boltzmann constant. The absorption coefficient used for the ceramic foam is  $10^4 \text{ m}^{-1}$  [47], while in the hot flue-gas region an absorption coefficient of  $0.46 \text{ m}^{-1}$  is used. The constant absorption coefficient of the flue gas is determined by calculating the emission in a single direction at the mean beam length and a mean temperature by using the Edwards wide band model, which includes the spectral information of gas radiation [24, 47]. In the ceramic-foam region the radiation originates from the solid phase and therefore, in this region, the temperature  $T_s$  of the solid phase is used in (5.7) instead of the gas temperature. The radiant heat flux  $q_r$  is obtained after integration of the intensity  $i'$  in direction  $\Omega$  over all space angles:

$$q_r = \int_{4\pi} i' \Omega \, d\omega. \quad (5.8)$$

The boundary surfaces are modelled as diffuse gray surfaces with an emissivity  $\epsilon$ . The net radiative heat flux for these surfaces is given by the difference between emission and absorption:

$$q_{\text{surf}} = \epsilon \left( \sigma_S T^4 - \int_{2\pi} i'_{\text{im}} \cos \theta \, d\omega \right), \quad (5.9)$$

where  $\theta$  denotes the angle with the normal vector on the surface and  $\omega$  a solid angle. The intensity  $i'_{\text{im}}$  of the radiation impinging on the surface is found by tracing rays back to their origin and solving (5.7) over this path. The boundary condition for (5.7) at the origin is found from the intensity  $i'_{\text{or}}$  of the radiation leaving the originating surface:

$$i'_{\text{or}} = \frac{1 - \epsilon}{\pi} \int_{2\pi} i'_{\text{im}} \cos \theta \, d\omega + \frac{\epsilon \sigma_S}{\pi} T^4. \quad (5.10)$$

The source terms in the energy equation for the gas phase and the solid phase ( $Q_{\text{rg}}$  and  $Q_{\text{rs}}$ ) are determined from the difference between absorption and emission in the medium:

$$Q_r = k \left( \int_{4\pi} i' \, d\omega - 4\sigma_S T^4 \right). \quad (5.11)$$

For the angular integral in (5.11), the intensities of the rays traced for the surface calculations are used. More details about the radiation model are given by Lammers [47].

### 5.3.3 Computational domain and boundary conditions

The computational domain is restricted to the hot, upper part of the furnace (see area enclosed by dotted line in figure 5.1). Furthermore, the computational domain includes some simplifications of the experimental set-up. First of all, the experimental set-up is described using an axi-symmetric coordinate system. Because the actual flow into the plenum is not axi-symmetric, the plenum is restricted to a height of 3 mm with a uniform inlet velocity at the top. The thickness of the burner is reduced from 10 mm to 1 mm in order to minimize

the number of small grid cells that is needed for an accurate radiation computation with a high absorption coefficient. Due to the relatively low conductivity used for the ceramic-foam burner, only the top layer is heated. A justification for this assumption is given by Lammers [47]. The flow grid is a rectangular mesh of 80 grid cells in axial direction and 50 cells in radial direction, with refinements in the burner region, at the flame front and near the walls. The radiation grid is constructed from the flow grid by combining multiple flow cells to a single radiation cell.

At the inlet, the velocity  $v_{\text{inlet}} = 7 \text{ cm s}^{-1}$ , temperature  $T_{\text{inlet}} = 300 \text{ K}$  and mixture composition are prescribed. At the outlet, the pressure is prescribed and the normal derivatives of all other variables are assumed to be zero. For the radiative computation both the inlet and outlet of the furnace are treated as black surfaces ( $\epsilon = 1$ ) radiating at a temperature of 300 K. At the furnace walls, the velocity and the species fluxes are zero. The boundary condition for the enthalpy equation at the furnace wall is given by the heat flux through the wall

$$q_{\text{wall}} = -\alpha_s(T_i - T_{\text{air}}), \quad (5.12)$$

with  $T_i$  the inner-wall temperature and  $T_{\text{air}}$  the temperature of the surrounding air. The heat transfer coefficient  $\alpha_s$  contains contributions from conduction through the wall (indicated by the conductivity  $\lambda_{\text{wall}}$ ) and free convection ( $\alpha_c$ ) and radiation ( $\alpha_r$ ) at the outside of the wall [49]:

$$\alpha_s = \left[ \frac{r_i}{\lambda_{\text{wall}}} \ln \frac{r_o}{r_i} + \frac{r_i}{r_o} (\alpha_c + \alpha_r) \right]^{-1}, \quad (5.13)$$

where  $r_i$  and  $r_o$  are the radii of the inner and outer wall, respectively. The temperature of the outer wall can be derived from this boundary condition. The temperature of the water-cooled heat exchanger is assumed to be 300 K. The furnace walls and the heat exchanger are treated as diffuse gray surfaces with an emissivity of  $\epsilon = 0.4$ .

The simulation has been performed by using the commercial flow solver package CFX-4 from AEA Technology [11]. The Discrete-Transfer method is a standard model of CFX. FGM has been implemented by means of user-defined subroutines. The computing time for the simulation was approximately 15 hours on a Silicon Graphics R10000 workstation. A simulation with detailed chemistry appeared to be impossible, because the standard solver of CFX-4 cannot deal with the stiffness of the equations.

The reduced chemistry computation has been performed with the same manifold as used for the 2D test results in chapter 2. This manifold is based on the skeletal mechanism listed in appendix A, which does not include NO chemistry. Therefore, NO emissions cannot be predicted with this manifold. However, FGM can be applied to any reaction mechanism. So, if NO chemistry is included in the flamelet computations, it will be possible to predict NO emissions by using FGM.

## 5.4 Results

The results of the numerical computation are shown in figure 5.2. The flow pattern is indicated by streamlines and the temperature field is represented using gray scales. In the figure it is shown that the burnt gases with a temperature of nearly 1700 K are cooled by the walls and the heat exchanger and leave the combustion chamber with a temperature of

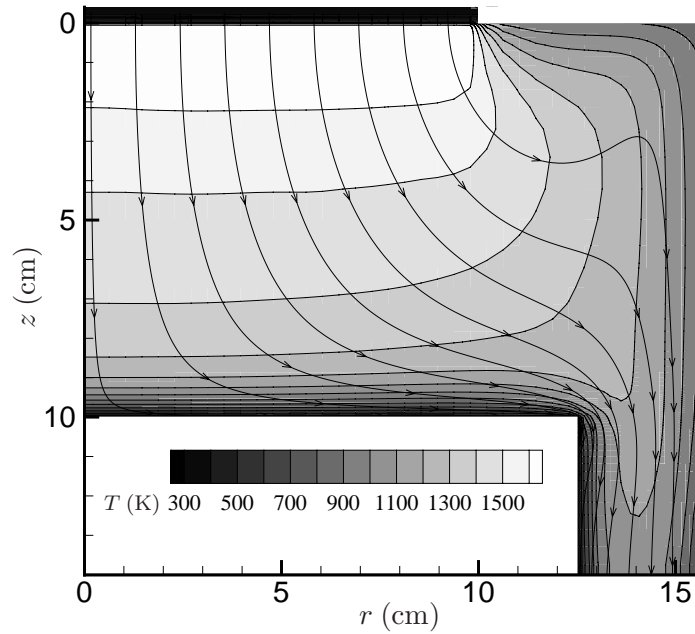


**Figure 5.2.** Numerical results for temperature (gray scales) and streamlines (lines with arrows).

approximately 1000 K. The flame itself is hardly visible, since it is only a millimeter thick and because it is located very close to and partly within the burner. In order to visualize the flame structure in more detail, temperature and  $Y_{\text{O}}$  profiles along the center axis ( $r = 0$ ) are plotted in figure 5.3 as function of the distance  $z$  to the burner. It shows clearly that the small scales are resolved by the computation and that the combustion process starts within the porous medium.

In the same figure the results for a pure 1D flame simulation with detailed chemistry [8] are plotted. In this simulation the same equations as for the computation of the 2D flame are solved. Only the modelling of the radiation terms is different. In the 1D model the energy flux due to radiation within the ceramic foam is approximated with the Rosseland diffusion equation [82], which is valid for an optically thick medium. The radiation term  $Q_{\text{rg}}$  in the 1D flame simulation is modelled by using the gray-medium approximation [13] within the optical thin limit:

$$Q_{\text{rg}} = 4k_{\text{P}}\sigma_{\text{S}}(T^4 - T_{\text{air}}^4). \quad (5.14)$$

The Planck mean absorption coefficient  $k_{\text{P}}$  depends on the temperature and on the partial gas pressures of  $\text{CO}_2$  and  $\text{H}_2\text{O}$ . The simulation of the 1D flame is performed using detailed chemical kinetics on a much finer grid than the computation of the 2D flame.

The results of the 1D flame can be compared with the profiles along the center axis, because the flame at the center of the burner can be assumed to be 1D. It demonstrates that the results of the temperature and species profiles computed with FGM are in good agreement with the detailed chemistry computations of the 1D flame. The small difference in temperature profile (and therefore in  $Y_{\text{O}}$ ) is caused by the different treatment of radiation and conduction in the ceramic foam and by the limitation of the manifold used. Since

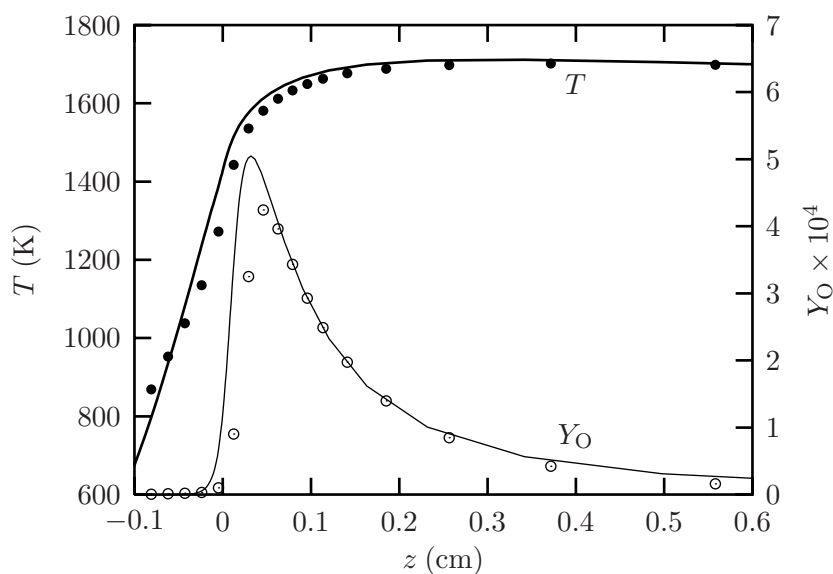


**Figure 5.3.** Temperature and  $Y_{\text{O}}$  profiles along the center axis. Symbols and lines are used to represent FGM (2D) and detailed chemistry (1D) results, respectively. The detailed chemistry results have been computed on a much finer grid.

the flame stabilizes deeply in the ceramic foam at low gas velocities, the deviation from adiabatic flame behaviour is large in this region. The correlations between the species and the enthalpy of the flame stabilized in the porous burner are therefore different than those of 1D adiabatic flamelets used to construct the manifold. This may lead to different reaction rates. However, since the main part of the reaction layer is located outside the ceramic foam, the chemical source terms are not much different from those of an adiabatic flamelet with the same enthalpy. Therefore, the stabilization of the flame is for this case well predicted by FGM, resulting in temperature of the burnt gases that is only 1% lower than the temperature computed with detailed chemistry.

The radial profiles of the temperature have been measured at 2.5 and 8 cm from the burner surface and the results are shown in figure 5.4. At  $z = 2.5$  cm the temperature profile indicates the presence of a hot core with a radius comparable with the radius of the burner and a colder region around it. Due to gas radiation, the temperature at the center has decreased from 1700 K near the burner to 1600 K at  $z = 2.5$  cm. At  $z = 8$  cm the maximum temperature is only 1350 K and the hot core cannot be distinguished any more. It can be seen that the predicted temperatures correlate well with the experimental values. The maximum difference between computational and experimental results is 75 K. The main problem in the measurements is the uncertainty in the location of the thermocouple. Due to this, the error in the measured temperatures is about 50 K.

In figure 5.5 the measured wall temperatures are compared with the computed results. Both the temperatures measured at the inside and the outside of the wall coincide well with the numerical results. The temperatures measured at  $z = 15$  cm are outside the computational domain. However, when the numerical results are extrapolated, they appear to agree with the measurements.

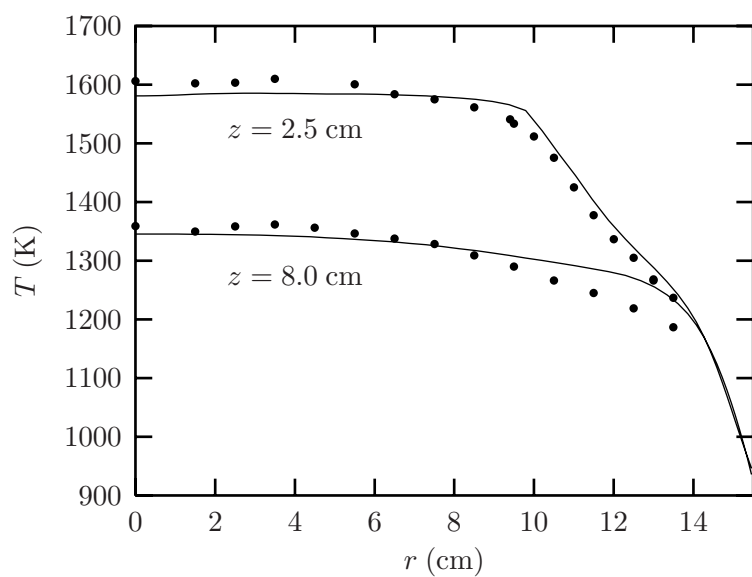


**Figure 5.4.** Radial profiles of the temperature at 2.5 and 8 cm from the burner surface. Symbols and lines are used to represent measurements and simulations, respectively.

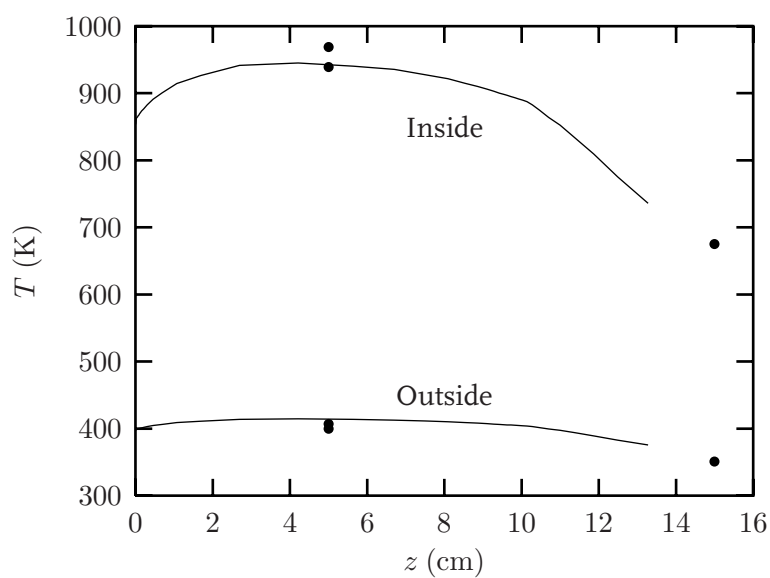


**Figure 5.5.** Vertical temperature profiles along the inside and outside of the furnace wall. Symbols and lines are used to represent measurements and simulations, respectively.

## 5.5 Conclusions

Due to the enormous reduction in computation time, FGM enables us to perform simulations of combustion in more realistic burner systems. In this chapter, FGM has been applied to a semi-practical burner system, which has been developed to study the performance of ceramic-foam surface burners in a hot furnace. Although the geometry of the furnace is not very complex, the stabilization of the flame on the porous burner in combination with the radiative heat transfer puts a high demand on computational power, which prohibits the use of detailed chemistry.

The numerical results computed by using a FGM with one progress variable and the enthalpy as additional controlling variable, agree well with temperature measurements. Lammers [47] has investigated the influence of several simulation parameters on the final result. He found that the influence of the emissivity of the walls is negligible. On the other hand, the computed temperature profiles appeared to be more sensitive to the emissivity of the heat exchanger and the gas-radiation model used. An increase of the emissivity of the heat exchanger from 0.4 to 0.7 resulted in a temperature decrease of approximately 40 K close to the heat exchanger. The use of a different gas-radiation model (gray-bands model) had an even larger effect and led to a temperature decrease of nearly 100 K at  $z = 8.5$  cm. Close to the burner the variations are much smaller, because in this region the temperature is mainly determined by chemistry and the stabilization of the flame.

The stabilization of the flame on the burner is modelled well by FGM, although some small differences with detailed chemistry results for a 1D flame occur. The large perturbation from local adiabatic behaviour in the porous region is the main reason for these differences. This problem can be solved by increasing the dimension of the manifold. An extra degree of freedom results in a more accurate description of the mixture composition and thus the chemical source term near the preheat zone of the flame. Another way to tackle this problem is to construct a manifold from 1D flames stabilized on ceramic-foam surface burners. In this way the non-adiabatic effects in the burner are included in the manifold.

Finally, we may conclude that FGM can be used to perform accurate and efficient simulations of the combustion process in this semi-practical burner system. The predicted temperature profiles agree well with the thermocouple measurements. The results computed with FGM can also be used to predict CO and NO emissions. Notice that the accuracy of FGM results is limited by the accuracy of the detailed reaction model: if simulations with detailed chemistry cannot predict emissions correctly, FGM computations will not give more accurate results. However, since species concentrations have not been measured yet in this set-up, a comparison between predicted and measured emissions remains for the future.

## Summarizing Conclusions

In this thesis the FGM method has been introduced and applied to (partially) premixed laminar flames. FGM can be considered as a combination of two existing approaches: the ILDM and the flamelet approach. FGM shares its basic assumption with flamelet approaches, but the implementation is very similar to ILDM. In high-temperature regions, in which chemistry is dominant, the flamelets are attracted by the ILDM. Therefore, in regions where the ILDM is attracting (and makes sense), the FGM is identical to the ILDM and it will be attracting as well. In 'low'-temperature regions FGM is more accurate, because 1D transport effects are taken into account. Therefore, less controlling variables are needed, which makes it an efficient reduction method. Test results of burner-stabilized methane/air flames indicate that only one progress variable plus the enthalpy are sufficient to reproduce detailed chemistry simulations very well.

As in the ILDM method, the accuracy of FGM can be increased by adding more dimensions to the manifold. This distinguishes the FGM method clearly from conventional flamelet methods, which consider only one progress variable. As shown in chapter 3, simulations of counterflow flames using a manifold with two progress variables yield more accurate results than a 1D manifold. Multi-dimensional manifolds are created by solving the flamelet equations for different initial conditions. Although there is a freedom of choice in the initial composition, the choice is not crucial. This is confirmed by the results for counterflow flames computed with two different 2D manifolds. Because the researcher has to choose the initial conditions, the FGM method cannot be automated to the same degree as ILDM. However, we want to emphasize that no detailed knowledge of the chemical processes is needed by the user, and that FGM can be applied to any fuel mixture or reaction mechanism. Moreover, new developments by Bongers *et al.* [6] might provide a similar mathematical basis for FGM as there is for ILDM.

In chapter 3 flame stretch effects have been investigated by simulating premixed counterflow flames. Flame stretch is together with flame curvature and transient effects one of the most important perturbations from local 1D flamelet behaviour. A relation between the mass burning rate of premixed laminar flames and flame stretch has been derived in chapter 3. The numerical results for counterflow flames with Lewis numbers equal to 1 agree very well with this relation for  $m_b$ . This not only holds for weak stretch, but for high strain rates as well. When Lewis numbers unequal to 1 are used, differential diffusion effects in combination with flame stretch lead to variations in the enthalpy and element mass fractions. For  $Le_i = \text{const}$  these variations result in a significant extra change in the mass burning rate as a function of the Karlovitz integral  $Ka$ .

In chapter 4 FGM has been applied to partially premixed flames. Triple flames have been investigated by using detailed chemistry and FGM. In partially premixed flames variations in the mixture fraction occur. To account for changes in the mixture fraction,  $Z$

has been used in the manifold as an additional controlling variable. This procedure is in fact similar to adding the enthalpy as variable to account for enthalpy changes in burner-stabilized flames and to the additional controlling variable to account for differential diffusion effects in counterflow flames. The structure of the different flame branches has been studied by using a flamelet analysis. The influence of flame stretch on the local mass burning rate in the premixed flame branches appeared to be significant and it cannot be described by using weak-stretch assumptions. Flamelets in the trailing diffusion flame have a similar structure as counterflow diffusion flames with the same scalar dissipation rate. Because the mixing length for the flames studied in this work is relatively large, the scalar dissipation rate is small and the heat release in the diffusion flame is 2 orders of magnitude smaller than that in the premixed flame branches. To make the diffusion flame more prominent and to really put FGM to a more stringent test, the mixture fraction gradient should be increased. This could be realized, for instance, by applying the boundary condition for the mixture composition closer to the premixed flame front.

Since the perturbations due to flame curvature and transient effects are not essentially different than due to flame stretch, we expect that they can be treated in the same way. As long as the length scale corresponding to the perturbation from ideal 1D flame behaviour is larger than the reaction layer thickness, a FGM with one progress variable and additional controlling variables to account for variations in the conserved variables will be sufficient. When the reaction layer is disturbed, extra progress variables can be added to the manifold. Therefore, it is expected that FGM can also be applied to turbulent flames in the so-called thin reaction zones regime [64]. However, since the reaction layer must be resolved in FGM, a large number of grid points is needed and the application for turbulent flames is limited to simple configurations. To treat turbulent flames in more complex geometries, time or space-averaged conservation equations should be used.

Besides accuracy, numerical efficiency is an important aspect of reduction methods. The comparison of computation times of 1D flame simulations with FGM and detailed chemistry has shown that a reduction of a factor of 50 can easily be reached. The reasons for this speed up are: 1) a faster evaluation of the chemical source terms, 2) less conservation equations to be solved, and 3) a reduction of the stiffness of the equations, which makes the use of fast explicit solvers possible. The results also show that FGM is more accurate than ILDM for the same number of dimensions. Therefore, less progress variables are needed in FGM to reach the same accuracy, which makes the method more efficient. Furthermore, due to the elimination of the fast time scales, the solution procedure becomes much more stable and less sensitive to the initial guess. The initial field of the progress variable for the Bunsen flames described in chapter 2, for instance, consisted of a binary distribution:  $\mathcal{Y} = 0$  for  $y < 5$  mm and  $\mathcal{Y} = 1$  for  $y \geq 5$  mm. Simulations with detailed chemistry need a much more accurate initial field. The solution computed with FGM could provide an accurate initial field for a detailed chemistry computation.

The enormous reduction of the computational cost makes it possible to treat more complex burner systems. This is demonstrated in chapter 5, in which the combustion process in a semi-practical furnace is simulated by using FGM. The predicted temperature profiles agreed well with measurements. A comparison with measured species concentrations would be interesting. Especially, NO emissions are interesting from a designer's point of view. Since NO formation continues in the burnt mixture, it cannot be described accurately by the progress variable  $\mathcal{Y}$ , which is constant there ( $\nabla\mathcal{Y} = 0$ ). This problem can be solved by including NO in the progress variable or by using a post-processing method [25],

in which the NO chemistry is separated from the actual flame computation. However, it is important to point out that the accuracy of any reduced reaction model is limited by the accuracy of the detailed reaction mechanism.

Finally, it may be concluded that FGM can be used to perform accurate and efficient numerical simulations of premixed or partially premixed laminar flames and that it can be a useful tool for the design of clean and efficient burner systems.



# Nomenclature

## Latin

$A$	pre-exponential factor	*
$a$	applied strain rate	$s^{-1}$
$\mathcal{C}$	convection	—
$c$	enthalpy flux coefficient	$J m^{-1} s^{-1}$
$c_p$	specific heat	$J kg^{-1} K^{-1}$
$c_{pi}$	partial specific heat	$J kg^{-1} K^{-1}$
$\mathcal{D}$	diffusion	—
$D$	diffusion coefficient	$m^2 s^{-1}$
$D_{ij}$	binary diffusion coefficient	$m^2 s^{-1}$
$D_{im}$	mixture-averaged diffusion coefficient	$m^2 s^{-1}$
$d$	stand-off distance	m
$E_a$	activation energy	J
$e$	unit vector	—
$\mathcal{F}$	convective term in (3.1)	$kg m^{-1} s^{-1}$
$F$	flux	$kg m^{-1} s^{-1}$
$\mathcal{G}$	diffusion flux in (3.1)	$kg s^{-1}$
$G$	level set scalar	—
$g$	gravity	$m s^{-2}$
$\mathcal{H}$	enthalpy flux due to differential diffusion	$J m^{-2} s^{-1}$
$h$	specific enthalpy	$J kg^{-1}$
$h_i$	partial specific enthalpy	$J kg^{-1}$
$\mathbf{I}$	unit tensor	—
$i$	radiative intensity	$J m^{-2} s^{-1}$
$\mathbf{J}$	Jacobian	$s^{-1}$
$k_{eq}$	equilibrium constant	*
$K$	stretch rate	$s^{-1}$
$k$	absorption coefficient	$m^{-1}$
$k_j$	reaction rate coefficient for reaction $j$	*
$k_P$	Planck mean absorption coefficient	$m^{-1}$
$Ka$	Karlovitz integral	—
$Ka$	Karlovitz number	—
$\ell$	path length	m
$L_x$	dimension of computational domain in $x$ -direction	m
$L_y$	dimension of computational domain in $y$ -direction	m
$Le_i$	Lewis number	—

$\mathcal{M}_i$	species symbol	—
$[\mathcal{M}_i]$	concentration of species $i$	$\text{mol m}^{-3}$
$M$	mass	kg
$\bar{M}$	mean molar mass	$\text{kg mol}^{-1}$
$M_i$	molar mass	$\text{kg mol}^{-1}$
$Ma$	Mach number	—
$m$	mass burning rate	$\text{kg m}^{-2} \text{s}^{-1}$
$N_{\text{av}}$	number of additional controlling variables	—
$N_{\text{cv}}$	total number of controlling variables	—
$N_e$	number of elements	—
$N_p$	number of gridpoints	—
$N_{\text{pv}}$	number of progress variables	—
$N_r$	number of reactions	—
$N_s$	number of species	—
$N_{\text{st}}$	number of steady-state relations	—
$\mathbf{n}$	normal vector	—
$\mathcal{P}$	multi-dimensional perturbations	—
$p$	pressure	Pa
$p_{\text{amb}}$	ambient pressure	Pa
$Q_h$	enthalpy transport along flame front	$\text{J m}^{-3} \text{s}^{-1}$
$Q_i$	species transport along flame front	$\text{kg m}^{-3} \text{s}^{-1}$
$Q_r$	radiation term	$\text{J m}^{-3} \text{s}^{-1}$
$\mathbf{q}$	heat flux	$\text{J m}^{-2} \text{s}^{-1}$
$\mathbf{q}_r$	radiant heat flux	$\text{J m}^{-2} \text{s}^{-1}$
$\mathcal{R}$	chemical reaction	—
$R$	universal gas constant	$\text{J mol}^{-1} \text{K}^{-1}$
$R_{\text{DF}}$	resistance based on Darcy-Forchheimer equation	$\text{kg m}^{-3} \text{s}^{-1}$
$r_j$	reaction rate for reaction $j$	$\text{mol m}^{-3} \text{s}^{-1}$
$r$	radial coordinate	m
$\mathcal{S}$	chemical source term in (3.1)	$\text{kg m}^{-1} \text{s}^{-1}$
$\mathbf{S}$	transformation matrix	—
$\mathbf{s}_i$	right eigenvector	—
$\mathbf{s}_i^L$	left eigenvector	—
$s$	arc length	m
$s_L$	burning velocity	$\text{m s}^{-1}$
$s_P$	propagation speed	$\text{m s}^{-1}$
$T$	temperature	K
$t$	time	s
$\mathbf{U}_i$	diffusion velocity	$\text{m s}^{-1}$
$\mathbf{u}$	fluid velocity	$\text{m s}^{-1}$
$\mathbf{u}_f$	flame surface velocity	$\text{m s}^{-1}$
$u$	velocity in $x$ -direction	$\text{m s}^{-1}$
$V$	volume	$\text{m}^3$
$v$	velocity in $y$ -direction	$\text{m s}^{-1}$
$W_i$	chemical source term	$\text{s}^{-1}$
$w$	velocity in $z$ -direction	$\text{m s}^{-1}$
$w_{ji}$	mass fraction of element $j$ in species $i$	—

$\mathbf{x}$	space coordinate	m
$X_i$	species mole fraction	—
$x$	space coordinate	m
$\mathcal{Y}$	progress variable	—
$Y_i$	species mass fraction	—
$y$	space coordinate	m
$Z$	mixture fraction	—
$Z_j$	element mass fraction	—
$z$	space coordinate	m

\* The units of the reaction rate variables depend on the reaction order. The unit of the pre-exponential factor depends on the reaction constant  $\beta$  as well.

### Greek

$\alpha_s$	surface heat transfer coefficient	$\text{J m}^{-1} \text{s}^{-1} \text{K}^{-1}$
$\alpha_v$	volumetric heat transfer coefficient	$\text{J m}^{-3} \text{s}^{-1} \text{K}^{-1}$
$\beta$	reaction constant	—
$\Delta$	change	—
$\delta_f$	flame thickness	m
$\delta_m$	mixing length	m
$\epsilon$	emissivity	—
$\eta$	porosity	—
$\theta$	angle	rad
$\kappa$	curvature	$\text{m}^{-1}$
$\Lambda$	diagonal matrix of eigenvalues	$\text{s}^{-1}$
$\lambda$	heat conductivity	$\text{J m}^{-1} \text{s}^{-1} \text{K}^{-1}$
$\lambda_i$	eigenvalue	$\text{s}^{-1}$
$\mu$	dynamic viscosity	$\text{kg m}^{-1} \text{s}^{-1}$
$\nu$	stoichiometric coefficient	—
$\xi$	collision efficiency	—
$\rho$	density	$\text{kg m}^{-3}$
$\sigma$	surface	$\text{m}^2$
$\sigma_S$	Stefan-Boltzmann constant	$\text{J m}^{-2} \text{s}^{-1} \text{K}^{-4}$
$\boldsymbol{\tau}$	stress tensor	$\text{kg m}^{-1} \text{s}^{-2}$
$\tau$	tortuosity	—
$\phi$	stoichiometry	—
$\varphi$	variable stored in database	—
$\chi$	scalar dissipation rate	$\text{s}^{-1}$
$\dot{\omega}_i$	chemical source term	$\text{kg m}^{-3} \text{s}^{-1}$
$\dot{\omega}_T$	heat release	$\text{J m}^{-3} \text{s}^{-1}$
$\omega$	solid angle	sr
$\boldsymbol{\Omega}$	unit direction vector	—

**Subscripts and superscripts**

$-\infty$	initial
b	burnt
f	forward
fu	fuel
eq	equilibrium
i	inner layer
im	impinging
ref	reference
o	stretchless
or	originating
ox	oxidizer
r	reversed
s	solid phase
st	stoichiometric
u	unburnt

## Reaction Mechanism

The reaction mechanism used in this work as base mechanism, is obtained from reference [85]. This mechanism consists of 25 reversible reactions involving 16 species. In table A.1 the different species are listed together with their molar mass and Lewis number. The Lewis numbers are obtained by a least-squares fit on the mixture-averaged properties [85]. Note that the effective Lewis number for  $N_2$  follows from the constraint (1.26). Because species with two or more C atoms are not considered, this mechanism is not suitable for fuel-rich conditions.

The reactions and their rate parameters  $A$ ,  $\beta$  and  $E_a$  are listed in table A.2. In some reactions a third molecule is involved, which does not react itself, but it is essential for the reaction to proceed. This third molecule, denoted by  $M$ , can be any species and its concentration is given by

$$[M] = \sum_i^{N_s} \xi_i [\mathcal{M}_i], \quad (A.1)$$

where  $\xi_i$  are the so-called collision efficiencies. The efficiencies used in this reaction mechanism are:  $\xi_{CH_4} = 6.5$ ,  $\xi_{CO_2} = 1.5$ ,  $\xi_{CO} = 0.75$ ,  $\xi_{O_2} = 0.4$ ,  $\xi_{H_2O} = 6.5$ ,  $\xi_{N_2} = 0.4$  and  $\xi_i = 1$  for the other species.

**Table A.1.** The species involved in the reaction mechanism together with their molar mass ( $\text{gr mol}^{-1}$ ) and Lewis number.

Species	$M_i$	$Le_i$	Species	$M_i$	$Le_i$
CH <sub>4</sub>	16.043	0.97	H	1.008	0.18
CH <sub>3</sub>	15.035	1.00	O <sub>2</sub>	31.999	1.10
CH <sub>3</sub> O	31.035	1.30	O	15.999	0.70
CH <sub>2</sub> O	30.027	1.28	OH	17.007	0.73
HCO	29.019	1.27	HO <sub>2</sub>	33.007	1.10
CO <sub>2</sub>	44.010	1.39	H <sub>2</sub> O	18.015	0.83
CO	28.011	1.10	H <sub>2</sub> O <sub>2</sub>	34.015	1.12
H <sub>2</sub>	2.016	0.30	N <sub>2</sub>	28.013	—

**Table A.2.** Reactions and their rate parameters. Units are mole, cm, s and K according to conventions used in standard literature on combustion chemistry.

	Reaction	$A$	$\beta$	$E_a/R$
1	$\text{H} + \text{O}_2 \rightleftharpoons \text{OH} + \text{O}$	$2.00 \times 10^{14}$	0.0	8455
2	$\text{O} + \text{H}_2 \rightleftharpoons \text{OH} + \text{H}$	$1.80 \times 10^{10}$	1.0	4442
3	$\text{H}_2 + \text{OH} \rightleftharpoons \text{H}_2\text{O} + \text{H}$	$1.17 \times 10^9$	1.3	1825
4	$\text{OH} + \text{OH} \rightleftharpoons \text{H}_2\text{O} + \text{O}$	$6.00 \times 10^8$	1.3	0
5	$\text{H} + \text{O}_2 + \text{M} \rightleftharpoons \text{HO}_2 + \text{M}$	$2.30 \times 10^{18}$	-0.8	0
6	$\text{H} + \text{HO}_2 \rightleftharpoons \text{OH} + \text{OH}$	$1.50 \times 10^{14}$	0.0	505
7	$\text{H} + \text{HO}_2 \rightleftharpoons \text{H}_2 + \text{O}_2$	$2.50 \times 10^{13}$	0.0	352
8	$\text{OH} + \text{HO}_2 \rightleftharpoons \text{H}_2\text{O} + \text{O}_2$	$2.00 \times 10^{13}$	0.0	503
9	$\text{CO} + \text{OH} \rightleftharpoons \text{CO}_2 + \text{H}$	$1.51 \times 10^7$	1.3	-382
10	$\text{CH}_4 \rightleftharpoons \text{CH}_3 + \text{H}$	$2.30 \times 10^{38}$	-7.0	57550
11	$\text{CH}_4 + \text{H} \rightleftharpoons \text{CH}_3 + \text{H}_2$	$2.20 \times 10^4$	3.0	4404
12	$\text{CH}_4 + \text{OH} \rightleftharpoons \text{CH}_3 + \text{H}_2\text{O}$	$1.60 \times 10^6$	2.1	1238
13	$\text{CH}_3 + \text{O} \rightleftharpoons \text{CH}_2\text{O} + \text{H}$	$6.80 \times 10^{13}$	0.0	0
14	$\text{CH}_2\text{O} + \text{H} \rightleftharpoons \text{HCO} + \text{H}_2$	$2.50 \times 10^{13}$	0.0	2009
15	$\text{CH}_2\text{O} + \text{OH} \rightleftharpoons \text{HCO} + \text{H}_2\text{O}$	$3.00 \times 10^{13}$	0.0	601
16	$\text{HCO} + \text{H} \rightleftharpoons \text{CO} + \text{H}_2$	$4.00 \times 10^{13}$	0.0	0
17	$\text{HCO} + \text{M} \rightleftharpoons \text{CO} + \text{H} + \text{M}$	$1.60 \times 10^{14}$	0.0	7398
18	$\text{CH}_3 + \text{O}_2 \rightleftharpoons \text{CH}_3\text{O} + \text{O}$	$7.00 \times 10^{12}$	0.0	12910
19	$\text{CH}_3\text{O} + \text{H} \rightleftharpoons \text{CH}_2\text{O} + \text{H}_2$	$2.00 \times 10^{13}$	0.0	0
20	$\text{CH}_3\text{O} + \text{M} \rightleftharpoons \text{CH}_2\text{O} + \text{H} + \text{M}$	$2.40 \times 10^{13}$	0.0	14500
21	$\text{HO}_2 + \text{HO}_2 \rightleftharpoons \text{H}_2\text{O}_2 + \text{O}_2$	$2.00 \times 10^{12}$	0.0	0
22	$\text{H}_2\text{O}_2 + \text{M} \rightleftharpoons \text{OH} + \text{OH} + \text{M}$	$1.30 \times 10^{17}$	0.0	22900
23	$\text{H}_2\text{O}_2 + \text{OH} \rightleftharpoons \text{H}_2\text{O} + \text{HO}_2$	$1.00 \times 10^{13}$	0.0	906
24	$\text{OH} + \text{H} + \text{M} \rightleftharpoons \text{H}_2\text{O} + \text{M}$	$2.20 \times 10^{22}$	-2.0	0
25	$\text{H} + \text{H} + \text{M} \rightleftharpoons \text{H}_2 + \text{M}$	$1.80 \times 10^{18}$	-1.0	0

## An Alternative Way to Create Multi-Dimensional Manifolds

In section 2.2.2 it is explained how a multi-dimensional manifold can be constructed by solving the flamelet equations (2.16)-(2.18) for different initial compositions. An alternative way to add an extra dimension to the manifold, is to include additional terms in the flamelet equations. Here we give two examples.

In section 3.4.1, compared to the theory a small relative increase is observed in the mass burning rate of counterflow flames with  $Le_i = 1$  at high strain rates. This effect is related to the boundary condition at the stagnation plane, which causes radicals in the burnt gases, such as H, O and OH, to diffuse upstream. Due to the higher concentration of radicals in the reaction zone, the reaction rates increase and, therefore, the mass burning rate increases. To capture this effect using FGM, a manifold is created using a series of flamelets computed with an artificially enhanced reaction rate for the reaction  $H_2 \rightarrow 2H$ , which is realized by increasing the reaction constant. This specific reaction is used, because the radical concentrations appear to be very sensitive to its reaction rate. Since the element mass fraction and the enthalpy are unchanged and the reverse reaction rate is computed using the equilibrium constant, the equilibrium mixture remains the same.

The series of flamelets with different amounts of radicals in the reaction layer, is used to construct a 2D manifold. The mass fraction of H is chosen as the second progress variable, because relatively the largest variations occur in  $Y_H$ . Besides solving an equation for  $\mathcal{Y}$ , a second conservation equation is solved for  $Y_H$ . The mass burning rates computed using this 2D FGM are displayed in figure B.1. It can be observed that the additional effect on the mass burning rate is modelled and that the results of the detailed computations are reproduced almost exactly. It should be noted that this 2D manifold is successful, because it is known beforehand (from detailed computations) which effects must be included in the manifold. If it is necessary, in general, to carry out a detailed chemistry computation in order to generate the correct FGM afterwards, this is certainly not a very promising solution. However, in many applications the most important perturbations are known or can be found without performing the detailed chemistry calculation.

The second manifold, which is generated by including an additional term in the flamelet equations, is created for counterflow flames with  $Le_i = \text{const}$ . In section 3.4.3 it has been explained how variations in  $Z_j$  and  $h$  can be accounted for using a manifold constructed of flamelets with different initial compositions. Another way to create such a 2D manifold, is to include a stretch term in the flamelet equations. Since the main perturbation in counterflow flames is flame stretch and because  $K = a$  in case of weak stretch, a constant-stretch term is included in the flamelet equations. This set of equations is then solved for a series of stretch rates:  $K = 0, 100, 200 \text{ s}^{-1}$ , etc. The resulting set of flamelets is parametrized by the progress variable  $\mathcal{Y}$  and the element mass fraction  $Z_H$ , which is the most suitable

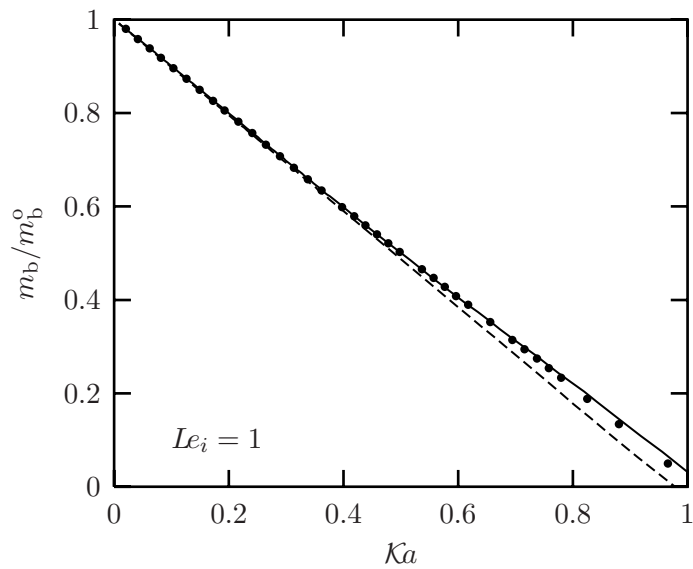


**Figure B.1.** Scaled mass burning rate as function of the Karlovitz integral for  $Le_i = 1$ . Full line: detailed; dotted line: 1D FGM; solid symbols: 2D FGM.

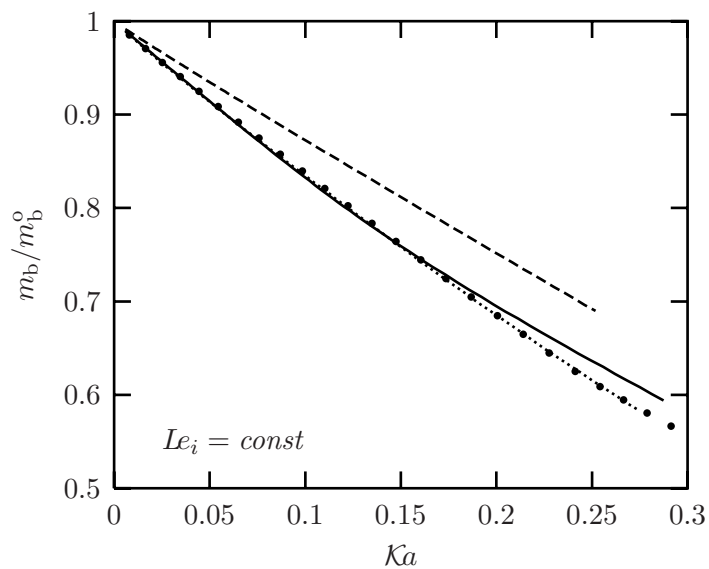


**Figure B.2.** Scaled mass burning rate as function of the Karlovitz integral for  $Le_i = const$ . Full line: detailed; dashed line: 1D FGM; dotted line: 2D FGM C; symbols: 2D FGM constructed using stretched flamelets.

second progress variable because it changes the most. For  $Z_H$  a conservation equation is solved, which is very similar to (2.34). The mass burning rates computed using this 2D FGM are plotted in figure B.2 as function of  $\mathcal{K}a$ . Since variations in  $Z_j$  and  $h$  are taken into account, the detailed results can be reproduced for weak stretch. Again, at higher strain rates the stagnation plane influences the results and higher-order stretch effects become important.



# References

- [1] Andrews G.E. and Bradley D., The burning velocity of methane-air mixtures, *Combust. Flame* 19:275–288 (1972)
- [2] Anthonissen M.J.H., *Local Defect Correction Techniques: Analysis and Application to Combustion*, Ph.D. thesis, Eindhoven University of Technology (2001)
- [3] Bennett B.A.V. and Smooke M.D., Local rectangular refinement with application to axisymmetric laminar flames, *Combust. Theory Modelling* 2:221–258 (1998)
- [4] Bilger R.W., The structure of turbulent nonpremixed flames, *Proc. Combust. Inst.* 22:475–488 (1988)
- [5] Blasenbrey T., *Entwicklung und Implementierung automatisch reduzierter Reaktionsmechanismen für die Verbrennung von Kohlenwasserstoffen*, Ph.D. thesis, Institut für Technische Verbrennung der Universität Stuttgart (2000)
- [6] Bongers H., van Oijen J.A. and de Goey L.P.H., Intrinsic low-dimensional manifold method extended with diffusion, *Proc. Combust. Inst.* 29 (2002)
- [7] Bouma P.H., *Methane-Air Combustion on Ceramic Foam Surface Burners*, Ph.D. thesis, Eindhoven University of Technology (1997)
- [8] Bouma P.H. and de Goey L.P.H., Premixed combustion on ceramic foam burners, *Combust. Flame* 119:133–143 (1999)
- [9] Buckmaster J., *The Mathematics of Combustion*, Society for Industrial and Applied Mathematics, Philadelphia (1985)
- [10] Buckmaster J. and Matalon M., Anomalous Lewis number effects in tribrachial flames, *Proc. Combust. Inst.* 22:1527–1535 (1988)
- [11] CFX, AEA Technology plc.  
<http://www.software.aeat.com/cfx>
- [12] CHEM1D, A one-dimensional laminar flame code, Eindhoven University of Technology  
<http://www.combustion.tue.nl/chem1d>
- [13] Chen J., Liu Y. and Rogg B., CO-H<sub>2</sub>-N<sub>2</sub>/air diffusion flames: Thermal radiation and transient effects, in *Reduced Kinetic Mechanisms for Applications in Combustion Systems*, edited by N. Peters and B. Rogg, pp. 202–229, Springer Verlag, Berlin (1993)

- [14] Chen J.H., Echekeki T. and Kollmann W., The mechanism of two-dimensional pocket formation in lean premixed methane-air flames with implications to turbulent combustion, *Combust. Flame* 116:15–48 (1998)
- [15] Christo F.C., Masri A.R. and Nebot E.M., Artificial neural network implementation of chemistry with pdf simulation of H<sub>2</sub>/CO<sub>2</sub> flames, *Combust. Flame* 106:406–427 (1996)
- [16] Chung S.H. and Law C.K., An integral analysis of the structure and propagation of stretched premixed flames, *Combust. Flame* 72:325–336 (1988)
- [17] Davis S.G., Quinard J. and Searby G., A numerical investigation of stretch effects in counterflow, premixed laminar flames, *Combust. Theory Modelling* 5:353–362 (2001)
- [18] Dixon-Lewis G., Flame structure and flame reaction kinetics II Transport phenomena in multi-component systems, *Proc. Roy. Soc. A* 307:111–135 (1968)
- [19] Dixon-Lewis G., Structure of laminar flames, *Proc. Combust. Inst.* 23:305–324 (1990)
- [20] Dold J.W., Flame propagation in a non-uniform mixture: Analysis of a slowly-varying triple-flame, *Combust. Flame* 76:71–88 (1989)
- [21] Domingo P. and Vervisch L., Triple flames and partially-premixed combustion in autoignition of non-premixed turbulent mixtures, *Proc. Combust. Inst.* 26:233–240 (1996)
- [22] Douglas C.C., Ern A. and Smooke M.D., Multigrid solutions of flame sheet problems on serial and parallel computers, *Parallel Algorithms and Applications* 10:225–236 (1997)
- [23] Echekeki T. and Chen J.H., Structure and propagation of methanol-air triple flames, *Combust. Flame* 114:231–245 (1998)
- [24] Edwards D.K., Molecular gas band radiation, in *Advances in Heat Transfer* 12, pp. 115–193, Academic Press, New York (1976)
- [25] Eggels R.L.G.M., *Modelling of Combustion Processes and NO Formation with Reduced Reaction Mechanisms*, Ph.D. thesis, Eindhoven University of Technology (1996)
- [26] Eggels R.L.G.M. and de Goey L.P.H., Mathematically reduced reaction mechanisms applied to adiabatic flat hydrogen/air flames, *Combust. Flame* 100:559–570 (1995)
- [27] Favier V., Vervisch L., Herrmann M., Terhoeven P., Binninger B. and Peters N., Numerical simulation of combustion in partially premixed turbulent flows, in *Numerical Flow Simulation*, edited by E.H. Hirschel, Notes on Numerical Fluid Mechanics, pp. 203–221, Vieweg (1998)
- [28] Ghosal S. and Vervisch L., Theoretical and numerical study of a symmetrical triple flame using the parabolic flame path approximation, *J. Fluid Mech.* 415:227–260 (2000)
- [29] Gicquel O., Darabiha N. and Thévenin D., Laminar premixed hydrogen/air counterflow flame simulations using flame prolongation of ILDM with differential diffusion, *Proc. Combust. Inst.* 28:1901–1908 (2000)

- 
- [30] Gicquel O., Thévenin D., Hilka M. and Darabiha N., Direct numerical simulations of turbulent premixed flames using intrinsic low-dimensional manifolds, *Combust. Theory Modelling* 3:479–502 (1999)
- [31] de Goey L.P.H., Mallens R.M.M. and ten Thijs Boonkcamp J.H.M., An evaluation of different contributions to flame stretch for stationary premixed flames, *Combust. Flame* 110:54–66 (1997)
- [32] de Goey L.P.H. and ten Thijs Boonkcamp J.H.M., A mass-based definition of flame stretch with finite thickness, *Combust. Sci. Technol.* 122:399–405 (1997)
- [33] de Goey L.P.H. and ten Thijs Boonkcamp J.H.M., A flamelet description of premixed laminar flames and the relation with flame stretch, *Combust. Flame* 119:253–271 (1999)
- [34] Groot G.R.A. and de Goey L.P.H., A computational study on propagating spherical and cylindrical premixed flames, *Proc. Combust. Inst.* 29 (2002)
- [35] Hartley L.J. and Dold J.W., Flame propagation in a nonuniform mixture: Analysis of a propagating triple-flame, *Combust. Sci. Technol.* 80:23–46 (1991)
- [36] Herrmann M., *Flamelet Libraries for Premixed and Partially Premixed Combustion*, Technical Report WVT 2002.03, Eindhoven University of Technology (2002)
- [37] Hirschfelder J.O., Curtis C.F. and Bird R.B., *Molecular theory of gases and liquids*, Wiley, New York (1964)
- [38] van 't Hof B., *Numerical Aspects of Laminar Flame Simulations*, Ph.D. thesis, Eindhoven University of Technology (1998)
- [39] Im H.G. and Chen J.H., Structure and propagation of triple flames in partially premixed hydrogen-air mixtures, *Combust. Flame* 119:436–454 (1999)
- [40] Kang S. and Kim Y., A pressure-based unstructured-grid finite-volume method for simulating laminar reacting flow, *Numer. Heat Transfer B* 41:53–72 (2002)
- [41] Karlovitz B., Denniston Jr. D.W., Knapschaefer D.H. and Wells F.E., Studies on turbulent flames, *Proc. Combust. Inst.* 4:613–635 (1953)
- [42] Kee R.J. and Miller J.A., A structured approach to the computational modeling of chemical kinetics and molecular transport in flowing systems, *Springer Series in Chemical Physics* 47:196 (1986)
- [43] Kioni P.N., Rogg B., Bray K.N.C. and Liñán A., Flame spread in laminar mixing layers: The triple flame, *Combust. Flame* 95:276–290 (1993)
- [44] Ko Y.S. and Chung S.H., Propagation of unsteady tribrachial flames in laminar non-premixed jets, *Combust. Flame* 118:151–163 (1999)
- [45] Konnov A.A., Detailed reaction mechanism for small hydrocarbons combustion (2000) <http://homepages.vub.ac.be/~akonnov/>

- [46] Lam S.H. and Goussis D.A., Conventional asymptotics and computational singular perturbation for simplified kinetics modeling, in *Reduced kinetic mechanisms and asymptotic approximations for methane-air flames*, edited by M.D. Smooke, pp. 227–242, Springer Verlag, Berlin (1991)
- [47] Lammers F.A., *Ceramic-Foam Surface Burners in High-Temperature Environments*, Ph.D. thesis, Eindhoven University of Technology (2001)
- [48] Lammers F.A., Bouma P.H., Althuisen T.A.M. and de Goey L.P.H., Stability and performance of ceramic foam surface burners in a hot environment, in *Fifth International Conference on Technologies and Combustion for a Clean Environment*, pp. 533–539, Lisbon Portugal (1999)
- [49] Lammers F.A., van Oijen J.A., Bouma P.H. and de Goey L.P.H., Modelling of ceramic foam surface burners using flamelet-generated manifolds, in *Second European Conference on Small Burner and Heating Technology*, pp. 29–37, Stuttgart Germany (2000)
- [50] de Lange H.C., *Modelling of Premixed Laminar Flames*, Ph.D. thesis, Eindhoven University of Technology (1992)
- [51] de Lange H.C. and de Goey L.P.H., Two-dimensional methane/air flame, *Combust. Sci. Technol.* 92:423–427 (1993)
- [52] Law C.K., A compilation of experimental data on laminar burning velocities, in *Reduced Kinetic Mechanisms for Applications in Combustion Systems*, edited by N. Peters and B. Rogg, pp. 19–31, Springer Verlag, Berlin (1993)
- [53] van Maaren A., *One-step chemical reaction parameters for premixed laminar flames*, Ph.D. thesis, Eindhoven University of Technology (1994)
- [54] Maas U. and Pope S.B., Simplifying chemical kinetics: Intrinsic low-dimensional manifolds in composition space, *Combust. Flame* 88:239–264 (1992)
- [55] Maas U. and Pope S.B., Laminar flame calculations using simplified chemical kinetics based on intrinsic low-dimensional manifolds, *Proc. Combust. Inst.* 25:1349–1356 (1994)
- [56] Majda A. and Lamb K.G., Simplified equations for low-Mach number combustion with strong heat release, in *Dynamical Issues in Combustion Theory*, edited by P.C. Fife, A. Linan and F.A. Williams, pp. 167–212, Springer Verlag, New-York (1991)
- [57] Markstein G.H., *Nonsteady Flame Propagation*, Pergamon Press, Oxford (1964)
- [58] Massias A., Diamantis D., Mastorakos E. and Goussis D.A., An algorithm for the construction of global reduced mechanisms with CSP data, *Combust. Flame* 117:685–708 (1999)
- [59] Müller C.M., Breitbach H. and Peters N., Partially premixed turbulent flame propagation in jet flames, *Proc. Combust. Inst.* 25:1099–1106 (1988)

- 
- [60] Najm H.N., Paul P.H., Mueller C.J. and Wyckoff P.S., On the adequacy of certain experimental observables as measurements of flame burning rate, *Combust. Flame* 113:312–332 (1998)
- [61] Ovink R., *Flamelet Modelling for Partially Premixed Turbulent Jet Diffusion Flames*, Ph.D. thesis, Eindhoven University of Technology (2001)
- [62] Peters N., Laminar flamelet concepts in turbulent combustion, *Proc. Combust. Inst.* 21:1231–1250 (1986)
- [63] Peters N., Reducing mechanisms, in *Reduced kinetic mechanisms and asymptotic approximations for methane-air flames*, edited by M.D. Smooke, pp. 48–67, Springer Verlag, Berlin (1991)
- [64] Peters N., *Turbulent Combustion*, Cambridge University Press, Cambridge (2000)
- [65] Peters N. and Rogg B. (editors), *Reduced kinetic mechanisms for applications in combustion systems*, Springer Verlag, Berlin (1993)
- [66] Peters N. and Williams F.A., Asymptotic structure of stoichiometric methane-air flames, *Combust. Flame* 68:185–207 (1987)
- [67] Phillips H., Flame in a buoyant layer, *Proc. Combust. Inst.* 10:1277–1283 (1965)
- [68] Pitts W.M., Assessment of theories for the behavior and blowout of lifted turbulent jet diffusion flames, *Proc. Combust. Inst.* 22:809–816 (1988)
- [69] Plessing T., Terhoeven P., Peters N. and Mansour M., An experimental and numerical study of a laminar triple flame, *Combust. Flame* 115:335–353 (1998)
- [70] Pope S.B., Computationally efficient implementation of combustion chemistry using *in situ* adaptive tabulation, *Combust. Theory Modelling* 1:41–63 (1997)
- [71] Pope S.B. and Maas U., *Simplifying Chemical Kinetics: Trajectory-Generated Low-Dimensional Manifolds*, Technical Report FDA 93-II, Cornell University (1993)
- [72] Réveillon J., Domingo P. and Vervisch L., Non-premixed flame ignition in turbulent flows, triple flame, in *Tenth symposium on turbulent shear flows*, The Pennsylvania State University (1995)
- [73] Rook R., *Acoustics in Burner-Stabilised Flames*, Ph.D. thesis, Eindhoven University of Technology (2001)
- [74] Ruetsch G.R. and Broadwell J.E., Effects of confinement on partially premixed flames, in *Annual Research Briefs*, pp. 323–333, Center for Turbulence Research (1995)
- [75] Ruetsch G.R., Vervisch L. and Liñán A., Effects of heat release on triple flames, *Phys. Fluids* 7:1447–1454 (1995)
- [76] Sato J., Effect of Lewis number on extinction behavior of premixed flames in a stagnation flow, *Proc. Combust. Inst.* 19:1541–1548 (1982)

- [77] Schmidt D., Blasenbrey T. and Maas U., Intrinsic low-dimensional manifolds of strained and unstrained flames, *Combust. Theory Modelling* 2:135–152 (1999)
- [78] Seshadri K. and Peters N., The inner structure of methane-air flames, *Combust. Flame* 81:96–118 (1990)
- [79] Seshadri K., Peters N., van Oijen J.A. and de Goey L.P.H., The asymptotic structure of weakly strained moderately rich methane-air flames, *Combust. Theory Modelling* 5:201–215 (2001)
- [80] Shah N.G., *The Computation of Radiation Heat Transfer*, Ph.D. thesis, University of London (1979)
- [81] Shu Z., Aggarwal S.K., Katta V.R. and Puri I.K., Flame-vortex dynamics in an inverse partially premixed combustor: The Froude number effects, *Combust. Flame* 111:276–295 (1997)
- [82] Siegel R. and Howell J.R., *Thermal Radiation Heat Transfer*, Hemisphere Publishing Corporation, New York (1992)
- [83] Smith G.P., Golden D.M., Frenklach M., Moriarty N.W., Eiteneer B., Goldenberg M., Bowman C.T., Hanson R.K., Song S., Gardiner Jr. W.C., Lissianski V.V. and Qin Z.  
[http://www.me.berkeley.edu/gri\\_mech/](http://www.me.berkeley.edu/gri_mech/)
- [84] Smooke M.D., Crump J., Seshadri K. and Giovangigli V., Comparison between experimental measurements and numerical calculations of the structure of counterflow, diluted, methane-air, premixed flames, *Proc. Combust. Inst.* 23:463–470 (1990)
- [85] Smooke M.D. and Giovangigli V., Formulation of the premixed and nonpremixed test problems, in *Reduced kinetic mechanisms and asymptotic approximations for methane-air flames*, edited by M.D. Smooke, pp. 1–28, Springer Verlag, Berlin (1991)
- [86] Somers L.M.T., *The Simulation of Flat Flames with Detailed and Reduced Chemical Models*, Ph.D. thesis, Eindhoven University of Technology (1994)
- [87] Stull D.R. and Prophet H., *JANAF thermochemical tables*, U. S. Government Printing Office, Washington (1971)
- [88] Thévenin D., Behrendt F., Maas U., Przywara B. and Warnatz J., Development of a parallel direct simulation code to investigate reactive flows, *Comp. Fluids* 25:485–496 (1996)
- [89] Thiart G.D., Finite difference scheme for the numerical solution of fluid flow and heat transfer problems on nonstaggered grids, *Num. Heat Transfer, Part B* 17:41–62 (1990)
- [90] Turanyi T., Parameterization of reaction mechanisms using orthogonal polynomials, *Comp. Chem.* 18:45–54 (1994)
- [91] Viskanta R., Interaction of combustion and heat transfer in porous inert media, in *Eighth Int. Symposium on Transport Phenomena in Combustion*, pp. 64–87, San Fransisco (1995)

- 
- [92] Warnatz J., Resolution of gas phase and surface combustion chemistry into elementary reactions, *Proc. Combust. Inst.* 24:553–579 (1992)
- [93] Warnatz J., Maas U. and Dibble R.W., *Combustion*, Springer Verlag, Berlin (1996)
- [94] Westbrook C.K. and Dryer F.L., Simplified reaction mechanisms for the oxidation of hydrocarbon fuels in flames, *Combust. Sci. Technol.* 27:31–34 (1981)
- [95] Williams F.A., *Combustion Theory*, Addison-Wesley Publishing Company, Redwood city (1985)
- [96] Williams F.A., Turbulent combustion, in *The Mathematics of Combustion*, edited by J. Buckmaster, pp. 97–131, Society for Industrial and Applied Mathematics, Philadelphia (1985)
- [97] World Energy Assessment, *Energy and the Challenge of Sustainability*, United Nations Development Programme, New York (2000)
- [98] Zeldovich Y.B. and Frank-Kamenetzki D.A., A theory of thermal propagation of flame, *Physico Chimica URSS* 9:341–350 (1938)



# Abstract

Numerical simulations of combustion processes using detailed chemical models are very time consuming. Therefore, several methods to simplify the description of the reaction kinetics have been developed during the last decades. The main part of these methods is based on the assumption that most chemical processes in a flame have a much smaller time scale than the flow time scale. These assumptions, however, give poor approximations in the 'colder' regions of a flame, in which transport processes are also important.

In this thesis a new method is presented, which can be considered as a combination of two existing approaches to speed up flame calculations, i.e. the flamelet and manifold approach. This new method, referred to as the *Flamelet-Generated Manifold* (FGM) method, shares the idea with flamelet approaches that a multi-dimensional flame may be considered as a set of one-dimensional flames. The implementation, however, is typical for manifold methods: a low-dimensional manifold in composition space is constructed, and the mixture composition is described by a small number of so-called controlling variables. The thermo-chemical variables are stored in a database, which can be used in subsequent flame simulations. During the flame simulation conservation equations have to be solved for the controlling variables only.

In the FGM method a manifold is generated by solving a set of one-dimensional flamelet equations. The solutions, called flamelets, are used to construct the manifold. Like in other manifold methods, the dimension of the manifold can be increased to satisfy a desired accuracy. Since the major parts of convection and diffusion processes are present in one-dimensional flamelets, the FGM method is more accurate in the 'colder' zones of premixed flames than reduction methods based on local chemical equilibria. Test results of one- and two-dimensional methane/air flames show that detailed chemistry computations are reproduced very well by using a FGM with only one progress variable apart from the enthalpy to account for energy losses. Due to the application of the FGM method, the computation time has been reduced by a factor of 50 in one-dimensional flames demonstrating the enormous potential of the method. For two-dimensional flames the computational gain is even larger.

The influence of disturbances from ideal one-dimensional premixed flame behaviour has been studied systematically. Flame stretch and curvature, for instance, play an important role in multi-dimensional flames, because they can have a large influence on the mass burning rate of premixed flames. Since a FGM is constructed using flat stretchless flamelets, these multi-dimensional effects are not included in the manifold. To investigate the influence of flame stretch, premixed counterflow flames have been modelled with both detailed chemistry and the FGM method. The mass burning rate of these counterflow flames has been analyzed and compared with theory. A good agreement is found between numerical results and theory. The results also show that the main effect of flame stretch

on the mass burning rate is reproduced by a one-dimensional FGM. Small remaining effects due to differential diffusion, can be accounted for by increasing the dimension of the manifold.

In many industrial applications combustion occurs under partially premixed conditions. To account for changes in the mixture fraction, which occur in partially premixed systems, the mixture fraction is added to the FGM as an additional controlling variable. So-called triple flames have been simulated for different mixture fraction gradients using both detailed chemistry and the FGM method. Triple flames are believed to play an essential role in flame propagation in partially premixed mixtures. The structure and propagation of triple flames have been studied by using a flamelet analysis. The influence of flame stretch on the mass burning rate appears to be significant in these flames. The results of detailed chemistry and FGM computations agree very well, because the length scales of the mixture fraction variations are much larger than the reaction layer thickness.

Due to the enormous reduction in computation time, the FGM method allows us to model more complex combustion systems. To investigate whether efficient and accurate simulations of realistic combustion systems are possible with the FGM method, a simulation of laminar combustion on a ceramic-foam burner in a radiating furnace has been presented. The results have been compared with temperature measurements. The good agreement between numerical predictions and measurements indicates that the FGM method provides a useful tool for the design process of clean and efficient combustion systems.

# Samenvatting

Het gebruik van gedetailleerde reactiemodellen voor de numerieke simulatie van verbrandingsprocessen vergt lange rekentijden. Daarom zijn gedurende de laatste decennia verschillende methoden ontwikkeld om de beschrijving van de reactiekinetiek te vereenvoudigen. Het grootste deel van deze methoden is gebaseerd op de aanname dat de meeste chemische processen in een vlam een veel kleinere tijdschaal hebben dan de stromingsverschijnselen. Deze aanname leidt echter tot een slechte benadering van de samenstelling van het mengsel in de 'koudere' delen van een vlam, waar transportprocessen ook belangrijk zijn.

In dit proefschrift wordt een nieuwe methode geïntroduceerd die gezien kan worden als een combinatie van twee reeds bestaande benaderingen om simulaties van vlammen te versnellen: de *flamelet* en *manifold* benadering. Deze nieuwe methode, die *Flamelet-Generated Manifold* (FGM) wordt genoemd, deelt de gedachte met de flamelet benadering dat een meer-dimensionale vlam beschouwd kan worden als een verzameling één-dimensionale vlammen. De implementatie is echter typisch voor manifold methoden: een laag-dimensionaal manifold in de compositieruimte wordt geconstrueerd en de samenstelling van het mengsel wordt beschreven met een klein aantal zogenaamde controlevariabelen. De thermochemische variabelen worden opgeslagen in een database, die vervolgens gebruikt kan worden voor simulaties van vlammen. Tijdens de simulatie hoeven alleen behoudsvergelijkingen voor de controle-variabelen te worden opgelost.

In de FGM methode wordt een manifold gegenereerd door een set één-dimensionale vergelijkingen op te lossen. De oplossingen, die *flamelets* worden genoemd, worden gebruikt om het manifold te creëren. Net als in andere manifold methoden kan de dimensie van het manifold vergroot worden om een gewenste nauwkeurigheid te bereiken. Aangezien convectie- en diffusieprocessen aanwezig zijn in één-dimensionale vlammen, is de FGM methode nauwkeuriger in de 'koudere' gebieden van een voorgemengde vlam dan methoden die gebaseerd zijn op lokaal chemisch evenwicht. Testresultaten van één- en twee-dimensionale methaan/lucht vlammen tonen aan dat berekeningen met gedetailleerde reactiemodellen zeer goed gereproduceerd kunnen worden met behulp van een FGM met slechts één voortgangsvariabele. Door het gebruik van de FGM methode is de rekentijd voor één-dimensionale vlammen met een factor 50 gereduceerd, wat de enorme kracht van de methode aantoont. Voor twee-dimensionale vlammen is de winst nog groter.

De invloed van afwijkingen van zuiver één-dimensionaal voorgemengd gedrag is systematisch bestudeerd. *Flame stretch* (vlamrek) en *flame curvature* (vlamkromming) bijvoorbeeld spelen een belangrijke rol in meer-dimensionale vlammen, omdat ze een grote invloed op de verbrandingssnelheid kunnen hebben. Omdat het FGM gegenereerd is met behulp van vlakke ongerekte vlammen, bevat het manifold deze meer-dimensionale effecten niet. Om de invloed van vlamrek te onderzoeken, zijn voorgemengde stagnatievlammen

gemodelleerd met zowel gedetailleerde chemie als FGM. De verbrandingssnelheid van deze stagnatievlammen is geanalyseerd en vergeleken met een theoretische benadering. De numerieke resultaten komen goed overeen met deze theorie. De resultaten tonen ook aan dat het belangrijkste effect van vlamrek op de verbrandingssnelheid wordt gereproduceerd met een één-dimensionaal FGM. Kleine overige effecten door differentiële diffusie kunnen meegenomen worden door de dimensie van het manifold te verhogen.

In veel industriële toepassingen vindt verbranding plaats onder gedeeltelijk voorge-mengde condities. Om de variaties in de mengselverhouding, die optreden in gedeeltelijk voorge-mengde systemen, mee te kunnen nemen, wordt de mengselverhouding toegevoegd aan het FGM als een extra variabele. Voor verschillende gradiënten in de mengselverhou-ding zijn zogenaamde *triple flames* gesimuleerd met een gedetailleerd reactiemodel en met de FGM methode. Van triple flames wordt gedacht dat ze een essentiële rol spelen in de voortplanting van vlammen in gedeeltelijk voorge-mengde mengsels. De structuur en voort-planting van triple flames zijn bestudeerd met behulp van een flamelet analyse. De invloed van vlamrek op de verbrandingssnelheid blijkt significant te zijn in deze vlammen. De resultaten van berekeningen met gedetailleerde chemie en met de FGM methode komen zeer goed overeen, omdat de lengteschaal van de variaties in de mengselverhouding veel groter is dan de dikte van de reactielaag.

Door de enorme afname van de rekentijd maakt de FGM methode het mogelijk om meer complexe verbrandingssystemen te simuleren. Om te onderzoeken of efficiënte en nauwkeurige simulaties van vlammen in realistische verbrandingsinstallaties mogelijk zijn met de FGM methode, is een berekening van laminaire verbranding op een keramische schuimbrander in een stralende verbrandingskamer gepresenteerd. De resultaten zijn vergeleken met temperatuurmetingen. De goede overeenkomst tussen de numerieke voor-spellingen en de metingen toont aan dat de FGM methode een bruikbaar stuk gereedschap is voor het ontwerpproces van schone en zuinige verbrandingsinstallaties.

# Curriculum Vitae

Jeroen Adrianus van Oijen was born in Nieuwkuijk (Vlijmen) on June 8, 1973. From 1985 to 1991 he followed pre-university education (VWO) at the Dr. Mollercollege in Waalwijk. After that, he studied Applied Physics at the Eindhoven University of Technology. His master's thesis, which he finished in 1996, concerned the numerical simulation of the advection of passive tracers in two-dimensional flows.

After receiving his university degree, Jeroen became a Junior Scientist (Assistent in Opleiding) in the group of prof.dr. L.P.H. de Goey at the Faculty of Mechanical Engineering of the same university. The Ph.D. project was supported by the Technology Foundation STW and concerned the development of new simulation techniques for combustion processes. During this Ph.D. project Jeroen presented results at international conferences in Heidelberg (Germany, 1999), Jacksonville (Florida USA, 2000), Edinburgh (Scotland, 2000), Seattle (Washington USA, 2001) and Sorrento (Italy, 2002).

As of January 1, 2002, Jeroen van Oijen is working as postdoctoral researcher in the Combustion Technology group of prof.dr. L.P.H. de Goey. This postdoctoral research involves the numerical simulation of turbulent flames using advanced flamelet models.

## Journal publications following from this thesis

- [1] van Oijen J.A. and de Goey L.P.H., Modelling of premixed laminar flames using flamelet-generated manifolds, *Combust. Sci. Technol.* 161:113–137 (2000)
- [2] van Oijen J.A., Lammers F.A. and de Goey L.P.H., Modeling of complex premixed burner systems by using flamelet-generated manifolds, *Combust. Flame* 127:2124–2134 (2001)
- [3] van Oijen J.A. and de Goey L.P.H., Modelling of premixed counterflow flames using the flamelet-generated manifold method, *Combust. Theory Modelling* 6:463–478 (2002)
- [4] van Oijen J.A. and de Goey L.P.H., Numerical simulations of triple flames by using the flamelet-generated manifold method, in preparation (2002)



# Dankwoord

Bij de totstandkoming van dit proefschrift heb ik hulp gehad van velen. Graag wil ik een aantal van hen hier noemen.

Op de eerste plaats natuurlijk Philip de Goey: zijn inspirerende begeleiding, interesse en ondersteuning zijn een enorme stimulans geweest. Mede dankzij zijn enthousiasme voor de verbrandingsleer is het vuur ook in mij gaan branden en ga ik met veel plezier verder in dit vakgebied. Ook gaat mijn dank uit naar Anton van Steenhoven, die het onderzoek op de voet heeft gevolgd en die altijd wil meedenken. Bovendien wil ik hem, Dirk Roekaerts en Harry Hoeijmakers bedanken voor het proeflezen en het geven van zinvolle suggesties voor het proefschrift.

Het onderzoek beschreven in dit proefschrift maakt deel uit van een project gefinancierd door de Technologiestichting STW. Iedereen die betrokken is geweest bij dit project en in het bijzonder Rogier Evertsen bedank ik voor de prettige samenwerking.

Het onderzoek is uitgevoerd in de divisie Thermo Fluids Engineering van de faculteit Werktuigbouwkunde van de Technische Universiteit Eindhoven. Alle leden van deze divisie bedank ik voor de gezelligheid en de goede sfeer. In het bijzonder wil ik mijn medespelers vermelden: de balgoochelaars van het zaalvoetbalteam, die laten zien dat je ook veel plezier kunt hebben zonder differentiaalvergelijkingen. Daarnaast gaat mijn speciale dank uit naar de leden van de onderzoeksgroep Combustion Technology, met name mijn kamergenoten Karel-Joop en Ronald, en de burens Gemmeke en Happy, voor hun hulp en gezelligheid. Oud-groepsgeenoot Bart Lammers ben ik dank verschuldigd voor de prettige samenwerking bij het onderzoek beschreven in hoofdstuk 5.

Ook buiten de universiteit zijn er vele mensen aan wie ik veel te danken heb. Dit geldt met name voor mijn familie en in het bijzonder mijn ouders, die altijd in me geloofd hebben en die altijd voor me klaar staan. Tenslotte wil ik Ingeborg bedanken voor haar geduld en onvoorwaardelijke steun. Zonder haar begrip en liefde was dit proefschrift nooit tot stand gekomen.

Bedankt allemaal!

Jeroen van Oijen, juli 2002.